The rheology of gas fluidized powders as determined in a vertical standpipe

THE RHEOLOGY OF GAS FLUIDIZED POWDERS AS DETERMINED IN A VERTICAL STANDPIPE

PROEFSCHRIFT

TER VERKRIJGING VAN DE GRAAD VAN DOCTOR IN DE TECHNISCHE WETENSCHAPPEN AAN DE TECHNISCHE HOGESCHOOL EINDHOVEN, OP GEZAG VAN DE RECTOR MAGNIFICUS, PROF. IR. J. ERKELENS VOOR EEN COMMISSIE AANGEWEZEN DOOR HET COLLEGE VAN DEKANEN IN HET OPENBAAR TE VERDEDIGEN OP VRIJDAG 18 JUNI 1982 TE 16.00 UUR

DOOR

GERTRUDA VAN DEN LANGENBERG-SCHENK

GEBOREN TE GENNEP

DIT PROEFSCHRIFT IS GOEDGEKEURD
DOOR DE PROMOTOREN:

PROF.DR.K.RIETEMA
PROF.DR.IR.W.P.M.VAN SWAAIJ

CONTENTS

CHAPTER 1

GENERAL INTRODUCTION

1.1 Introduction

Synopsis

The importance of insight in the flow behaviour of flowing fluidized powders is indicated from the point of view of direct industrial applications (transport of powders) and of more indirect applications such as fluidized bed reactors, fluidized bed dryers.

The investigation reported here was started with the aim to get insight in the flow behaviour of flowing fluidized powders.

A. In industry fluidized bed conveyors have been used frequently since long (about 1949) for transporting several kinds of powders e.g. fly ash, coal, dust, washing powders, plastic, metal powders, alumina, cracking catalyst, sand and wheat.
   This method has several advantages:
   1. The simplicity of construction and operation of the installation.
   2. The low capital cost compared to mechanical methods.
   3. The low running cost compared to pneumatic conveying, where (very) high air velocities are used, causing high energy consumption.
   4. The low maintenance cost compared to mechanical methods.
   5. The minimal attrition of the transported powders compared to the occurring particle degradation in pneumatic conveying.
   6. The minimal wear of the carrying lines compared to the abrasion of carrying lines in pneumatic conveying.
   7. The system is completely closed which means:
      the cleanliness of working
      the low wastage of powder
      the possibility to use high temperatures, if necessary.
   8. The high attainable conveying rates.

   Of course there are also drawbacks:
   1. The direction of transport is almost restricted to the vertical. In the case the direction is downwards the conveyor is called a standpipe.

2. Only powders with good fluidizing properties are suited for handling.

More serious are the practical problems met, such as blockage of the lines and the impossibility to reach the design capacity. These problems cannot be solved yet satisfactorily because a strong theoretical basement lacks, only experience and rules of thumb are available.

B. An extended comprehension of the flow behaviour will clarify the overall circulation in fluidized bed reactors. This overall circulation plays an important role in the occurring mixing process. The mixing influences the mass transfer, heat transfer and conversion rate, the most important parameters.

C. Knowing the flow in undisturbed systems, the next step is to get information about systems containing obstructions for flow, e.g. pipe bundles, artificial or spontaneous bubbling.

   i. The flow around rising bubbles is of importance for an insight in the coalescence and splitting up of bubbles, a process which in freely bubbling beds is continuously occurring.

   ii. For the mass transfer and the cloud*) thickness the flow around rising bubbles is of great importance. The cloud thickness is certainly influenced by the flow around the bubbles, while the cloud thickness influences the mass transfer from the dense phase to the bubble phase.

   iii. The influence of obstructions on the flow is not understood sufficiently. Heat transfer from pipe bundles to fluidized beds is rather common however. The mainly empirical knowledge of the heat transfer in such systems is not yet understood well.

The approach followed here to solve the rheological behaviour of flowing powders is more fundamental compared to most literature studies. These are briefly discussed in chapter 2.

*) The cloud is that part of the dense phase around the rising bubble where the interstitial gas is in direct convectional exchange with the bubble gas.

The experimental measuring techniques used are described in section 3.1. Section 3.2 contains a brief description of the conventional measuring devices. A new technique to measure the velocity profile in flowing powders using radioactive labeling techniques is described in chapter 4.
Chapter 5 gives the measuring results, conclusions and suggestions for further investigations.

1.2 Basic concepts

Synopsis

The most common rheological models are briefly mentioned. The most fundamental parameters are introduced.

For a good understanding of the following chapters some basic concepts are supposed to be known. For the sake of completeness these will be briefly mentioned in the following. Several models, describing the rheological behaviour of liquids exist:

1. The most simple one suggests a linear relation between τ and $\dot{\gamma}$. Fluids, obeying this law, display a so-called Newtonian behaviour:

   $$\tau = -\mu \dot{\gamma}$$

   The constant μ represents the dynamical viscosity.

2. Other materials show a shear only when the shearing stress exceeds a certain minimum value: the yield value τ_0. For values of τ with:

   $$|\tau| > \tau_0$$

   the relationship is linear.

   Thus: $\dot{\gamma} = 0$ for $|\tau| < \tau_0$

   $-\mu\dot{\gamma} = \tau \pm \tau_0$ $|\tau| \geq \tau_0$

   Materials behaving as such are called Bingham plastics.

3. When the rate of shear increases more than linearly with the shear stress without occurrence of a yield value the material is said to show a pseudo-plastic behaviour.

   $$\tau = -\mu_a |\dot{\gamma}|^{n-1} \dot{\gamma} \qquad n < 1$$

where μ_a is the apparent viscosity.

4. Dilatant behaviour implies an increase of $\dot{\gamma}$ less than linear with τ, without existance of a yield value τ_o:

$$\tau = -\mu_a \, |\dot{\gamma}|^{n-1} \, \dot{\gamma} \qquad n > 1$$

Models 3 and 4 are also called power law models.

5. The Eyring model describes the rheological behaviour as follows:

$$\tau = A \operatorname{arcsinh} (-B\dot{\gamma})$$

which implies pseudo-plastic behaviour for finite values of τ and reduces to a linear relationship in the limiting case, when τ approaches zero:

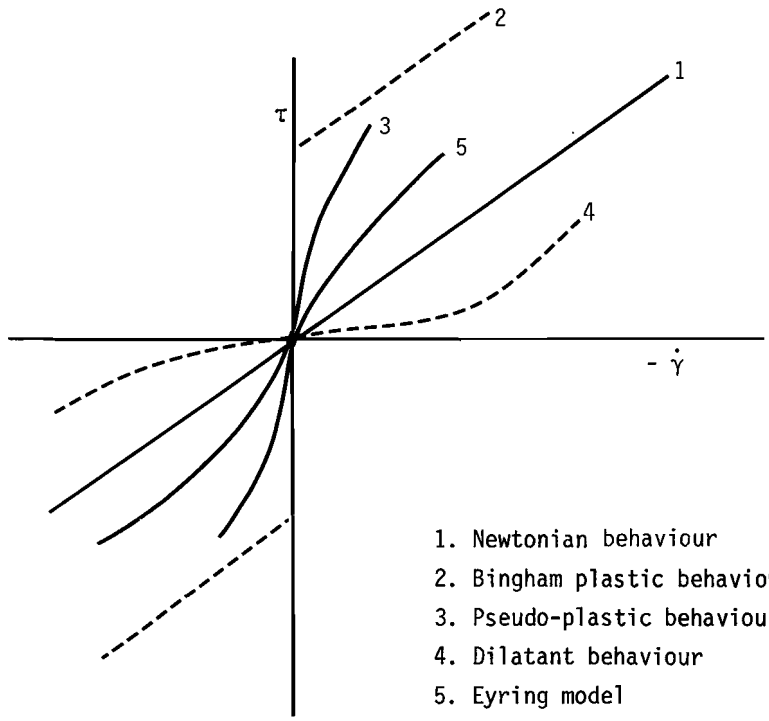

Figure 1.1 Sketch of the relationship between shear stress and shear rate for some common used models.

$\tau \approx -AB\ \dot{\gamma}$

The dynamical viscosity approaches the limiting value AB.
In Figure 1.1 these relations are sketched.

From the relation between shear stress and velocity gradient the velocity profile can be calculated. This will be done here for one simple case: the axial symmetrical flow in a cylindrical tube (radius R).

From a simple force balance follows:

$$\frac{dP}{dz} + \frac{1}{r}\frac{d}{dr}(r\tau) = 0$$

where $\frac{dP}{dz}$ is the pressure gradient in the direction of flow (z). By integration the expression for τ is obtained:

$$\tau(r) = \frac{r}{2}\left(-\frac{dP}{dz}\right)$$

i. For Newtonian flow this equation leads to:

$$v(r) = \frac{1}{4\mu}\left(-\frac{dP}{dz}\right) R^2 \left(1 - \frac{r^2}{R^2}\right) + v_{wall}$$

If v_{wall} is zero this reduces:

$$v(0) = v_{max} = \frac{R^2}{4\mu}\left(-\frac{dP}{dz}\right)$$

$$\bar{v} = \tfrac{1}{2} v_{max}.$$

$$\frac{v(r)}{\bar{v}} = 2\left(1 - \frac{r^2}{R^2}\right)$$

ii. The Bingham flow behaviour leads to:

$$v(r) = \frac{R^2}{4\mu}\left(1 - \left(\frac{r}{R}\right)^2 - \frac{2r_o}{R}\left(1 - \frac{r}{R}\right)\right)\left(-\frac{dP}{dz}\right) + v_{wall} \qquad R \geq r \geq r_o$$

$$v(r) = \frac{R^2}{4\mu}\left(1 + \left(\frac{r_o}{R}\right)^2 - \frac{2r_o}{R}\right)\left(-\frac{dP}{dz}\right) + v_{wall} \qquad r_o \geq r \geq 0$$

where $r_o = 2\tau_o / \left(-\frac{dP}{dz}\right)$

If v_{wall} is zero:

$$v(r) = \frac{R^2}{4\mu}\left(1 - \left(\frac{r}{R}\right)^2 - \frac{2r_o}{R}\left(1 - \frac{r}{R}\right)\right)\left(-\frac{dP}{dz}\right) \qquad R \geq r \geq r_o$$

$$v(r) = \frac{R^2}{4\mu}\left(1 + \left(\frac{r_o}{R}\right)^2 - \frac{2r_o}{R}\right)\left(-\frac{dP}{dz}\right) \qquad r_o \geq r \geq 0$$

$$\bar{v} = \frac{R^2}{8\mu} \left(- \frac{dP}{dz}\right) \left(1 + \frac{1}{3} \left(\frac{r_o}{R}\right)^4 - \frac{4}{3} \left(\frac{r_o}{R}\right)\right)$$

iii. The power law model gives:

$$v(r) = \frac{1}{2\mu} \left(- \frac{dP}{dz}\right)^{\frac{1}{n}} \cdot \frac{n}{n+1} \left(R^{\frac{n+1}{n}} - r^{\frac{n+1}{n}}\right) + v_{wall}$$

If v_{wall} is zero:

$$\bar{v} = \frac{1}{2\mu} \left(- \frac{dP}{dz}\right)^{\frac{1}{n}} \frac{n}{3n+1} R^{\frac{n+1}{n}}$$

$$\frac{v(r)}{\bar{v}} = \frac{3n+1}{n+1} \left(1 - \left(\frac{r}{R}\right)^{\frac{n+1}{n}}\right)$$

iv. The Eyring model leads to:

$$v(r) = \frac{2A}{B\left(- \frac{dP}{dz}\right)} \left[\cosh \left(\frac{R}{2A} \left(- \frac{dP}{dz}\right)\right) - \cosh \left(\frac{r}{2A} \left(- \frac{dP}{dz}\right)\right)\right] + v_{wall}$$

If v_{wall} is zero:

$$\bar{v} = \frac{8A^3}{B\left(- \frac{dP}{dz}\right)^3 R^2} \left[\cosh \left(\frac{R}{2A} \left(- \frac{dP}{dz}\right)\right) \left(\left(\frac{R}{2A}\right)^2 \left(- \frac{dP}{dz}\right)^2 + 2\right)\right.$$

$$\left. -2 \frac{R}{2A} \left(- \frac{dP}{dz}\right) \cdot \sinh \left(\frac{R}{2A} \left(- \frac{dP}{dz}\right)\right) - 2\right]$$

Graphs of $v/\bar{v}$ for the case that $v_{wall} = 0$ are given in Figure 1.2.

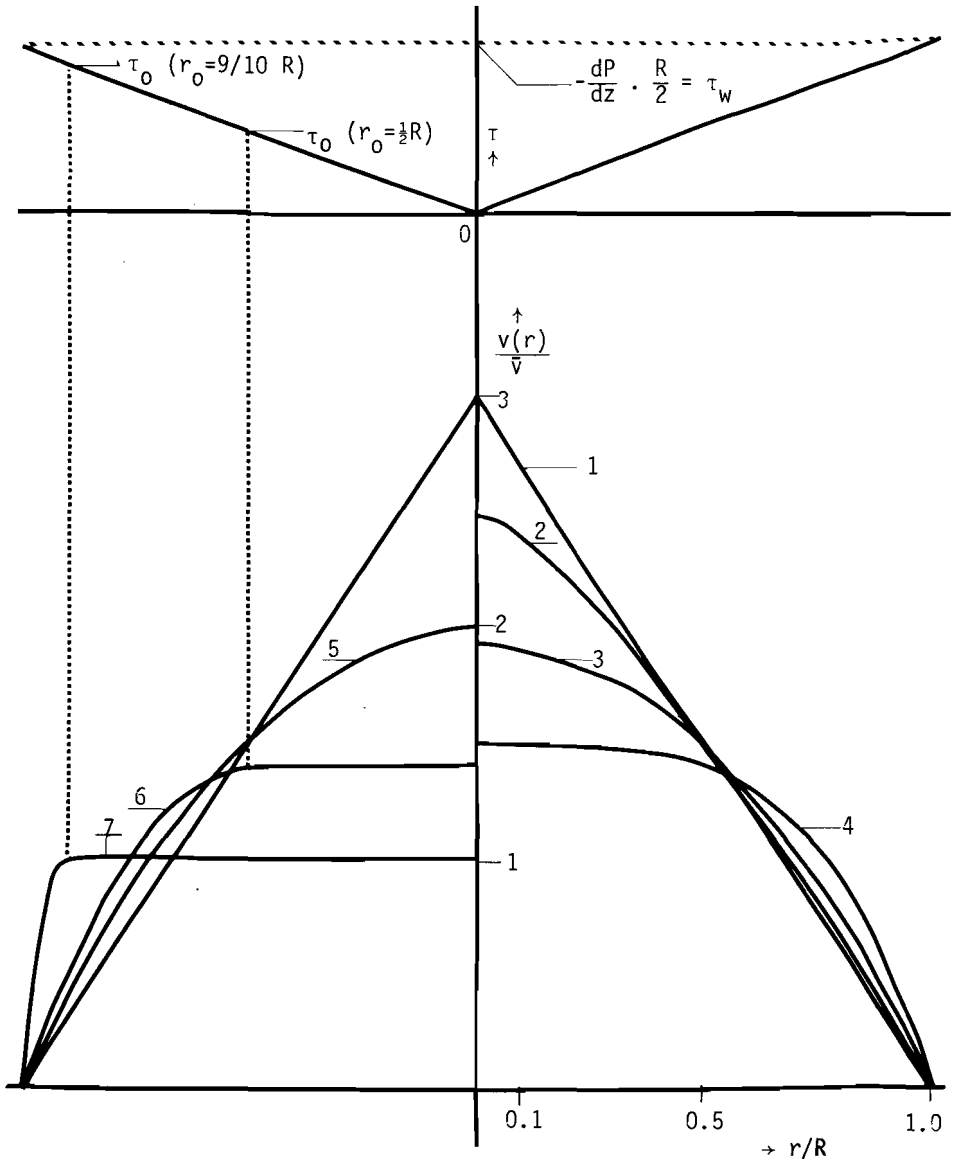

1. power law n=∞
2. power law n=3
3. Eyring
4. power law n=1/3
5. Newtonian
6. Bingham (r_o=0.5R)
7. Bingham (r_o=0.9R)

Figure 1.2 Sketch of the velocity profile of flowing material in a cylindrical pipe according to several models. The shear stress variation is also indicated.

List of symbols

A	constant in Eyring model	[-]
B	constant in Eyring model	[s]
n	constant in power law	[-]
$\frac{dP}{dz}$	pressure gradient	[Nm^{-3}]
R	radius of pipe	[m]
r	radial position	[m]
r_o	radius of the plug (Bingham model)	[m]
v	local velocity of flowing medium	[ms^{-1}]
$\bar{v}$	averaged velocity of flowing medium	[ms^{-1}]
v_{max}	maximum velocity of flowing medium	[ms^{-1}]
v_{wall}	wall slip velocity of flowing medium	[ms^{-1}]

Greek symbols

$\dot{\gamma}$	rate of shear	[s^{-1}]
μ	dynamical viscosity	[Poise]
μ_a	apparent viscosity (power law model)	[$Nm^{-2}s^n$]
τ	shear stress	[Nm^{-2}]
τ_o	yield shear stress	[Nm^{-2}]

CHAPTER 2

LITERATURE SURVEY

2.1 Introduction

Synopsis

A general discussion is given about the use of liquid viscosimeters in fluidized beds. The influence of bubbles is described. The discrepancy between liquid fluidized beds and gas fluidized beds is mentioned. The important quantities describing the rheological behaviour are summarized. Some general trends of the measured fluidized bed viscosity are given.

In literature many reports can be found describing investigations concerning the rheological behaviour of fluidized powders. Many investigators only mention the concept of viscosity in describing the rheological behaviour. It is, however, not clear that this concept is applicable and if so one can question if this concept is sufficient in describing the rheological behaviour. It is not proved that a fluidized system behaves Newtonian.

Often a viscosimeter is used, essentially developed for the use in liquids such as: Stormer viscosimeters (where the force on the blades of the rotor is measured as function of the rotation speed), Couette viscosimeters (where a set of two concentrical cylinders is used, one is rotating, the other is kept stationary; the torque needed to prevent rotation of the second cylinder is measured), falling or rising ball viscosimeters (the drag on a moving ball is determined), torsion pendulum viscosimeters (where the decay of amplitude of the oscillation with time is measured) and others. In these cases a moving measuring device is put in a stationary fluidized bed. In contrast to most authors Grace [3] did not use an extra measuring device in a stationary bed, but made use of rising bubbles. It is also possible to use a stationary measuring device in a flow of fluidized powder. This kind of measurements involves measurements in inclined channels or closed horizontal channels.

The frequent use of conventional viscosimeters is readily understandable since, just like in liquids, also in a fluidized bed a resistance against flow exists. This resistance is a kind of internal friction

between the particles and resembles the concept of "viscosity" used in describing the rheology of liquids. The friction is caused by statical forces, such as electrostatical forces, v.d.Waals forces, capillary forces, as well as by dynamical forces, which are due to the particle motion. It will be clear that the shape of the particles, the inter-particle distances (which are directly related to the bulk porosity), the gas velocity and the gas viscosity will influence this "viscosity". However, the structure of a liquid differs considerably from the fluidized bed structure. Secondly the liquid is a one phase system while a fluidized bed is at least a two phase system: solids and fluidizing medium, where the fluidizing medium is moving in one, well defined direction.

The problems met when trying to determine the viscosity of high concentrated suspensions only partly reflect the difficulties to be encountered in a fluidized bed. The use of measuring devices in relative motion with the fluidized bed will cause disturbances. It is a well-known fact that every obstacle in a fluidized bed causes preferential bubbling along the walls of the foreign object, moving or not. A moving object causes breaking up of rising bubbles improving in this way the fluidization quality. The usual rise pattern is disturbed too. When the fluidized bed is freely bubbling additional problems occur. The fluidized bed consists in that case of two distinct phases: a dense phase and a bubble phase. Because in the bubble phase there are no particles it is more plausible to speak about a viscosity of the dense phase rather than of an overall viscosity of the fluidized bed. When using a measuring device in a bubbling fluidized bed an overall viscosity is measured.
The bubbles will create also phenomena,which cause additional difficulties:

i. Extra overall solids circulation will be induced by the bubbles causing an increased shear stress.
ii. When a bubble hits the measuring device the shear stress will locally reduce to zero.
iii. Rising bubbles create extra momentum transport causing extra mixing and breaking up of boundary layers. This gives an increase in the shear stress at the measuring device.

iv. Depending on the measuring method the bubbles might influence the motion of the measuring device.

v. The conditions for which the usual relationship between shear stress and shear rate holds (i.e. laminar flow) are disturbed heavily.

For all these reasons it makes no sense to measure the "viscosity" in a bubbling fluidized bed. It is a great pity that most authors do not recognize this problem and do not mention if the bed in which they measured was freely bubbling or not. Only from the gas flow rate one can guess that in many cases this has been the case.

All methods in a stationary fluidized bed using an extra measuring device assume that the investigated medium sticks to the surface of the measuring device. Because the fluidized bed is less coherent than a liquid it is quite possible that slip occurs, especially when the surfaces of the measuring device are rather smooth and hard or the device is moving rather rapidly. The assumption that the medium sticks to the measuring device should always be checked. A verification, however, often lacks in the reports.

The size of the measuring device has to exceed the particle size considerably and has to be small compared to the fluidized bed dimensions. This condition is mostly no problem.

The most serious problem is the porosity variation that occurs near the moving foreign body. The "viscosity" will certainly depend on the interparticle distances as has been outlined in the foregoing. Because it is impossible to measure accurately the local bulk porosity near the measuring device without disturbing the fluidized bed behaviour and/or the viscosity measurement the obtained information is insufficient: At best the averaged bed porosity is obtained. But to relate the measured viscosity to the actual existing porosity at the wall of the measuring device seems impossible.

Another shortcoming is that it happens that assumptions are made concerning the rheological behaviour e.g. Newtonian behaviour or concerning the flow e.g. laminar flow. But often no investigations are reported that allow a check of the validity of the assumptions, therefore the evaluation of the measuring results is sometimes doubtful.

Measurements using rising bubbles as measuring device seem very attractive because no additional disturbing devices are used. On the other hand the evaluation of such measurements is doubtful. The equations of Grace [3] are based on measurements of rising bubbles in liquids and relate the shape of the bubble to its Reynolds number. The pressure field around a gas bubble in a fluidized bed, however, is not comparable to the pressure field around a gas bubble in liquid. This is caused by the flow of gas (from the dense phase) through the gas bubble (i.e. bubble phase). This effect will certainly influence the rising velocity and the shape of the bubble strongly.

There are also measurements in liquid fluidized beds which are certainly interesting but these are not comparable to measurements in gas fluidized beds because of the following reasons:

i. In liquid fluidized beds only homogeneous fluidization occurs. No bubbles are present in the bed.
ii. The degree of expansion is quite different in liquid fluidized beds compared to air fluidized beds. The particle-particle interaction, which is very important in air fluidized beds, is absent.
iii. In liquid fluidized systems the viscosity of the fluidizing medium -the liquid- is that high that it is no longer allowed to neglect it, as can be done in air fluidized beds.

In literature many papers can be found concerning the viscosity of fluidized stationary beds or the flow properties of powders -fluidized or not- in horizontal and inclined channels.

From the introduction (section 1.2) it will be clear that there are three important quantities, characterizing the rheological behaviour:

1. The wall slip velocity, i.e. the velocity of the fluidized bed at the walls of the measuring device (when using conventional viscosimeters in stationary fluidized beds) or at the walls of the channel (when measuring in channels containing a flowing powder).
   This quantity is not mentioned generally when using viscosimeters and is moreover difficult to estimate. In measurements in flowing powder the velocity at the walls and bottom of the channel is mostly assumed to be equal to zero. However, a check if the velocity at the bottom actually is zero mostly lacks.

2. The yield value of the shear stress. At the start of this investigation prelimenary measurements were carried out using a hollow cylinder, coated with a thin rubber foil to prevent slip, in a small gas fluidized bed (Ø 9 cm). These measurements [40,41] showed the problems and difficulties occurring in this kind of experimentation. Therefore another way for studying the rheological behaviour was sought which is described in this thesis. Our measurements revealed clearly, however, that a certain minimum shear stress is required to induce a motion of the fluidized bed. In literature the possibility of the existence of a yield value is often not mentioned. When assuming Newtonian behaviour this is not surprising, because this flow behaviour does not account for a yield shear stress.
3. The viscosity of the fluidized bed. Reading papers concerning the rheological behaviour of fluidized systems one gets the impression that often the attention is solely focussed on the viscosity value. It will be clear, however, from the foregoing that this concept only partly describes the flow behaviour of fluidized systems.

Concluding one can say that it seems very difficult to obtain reliable, sufficiently accurate measuring results when trying to determine the rheological behaviour of fluidized powders. Especially when using conventional viscosimeters care has to be taken when interpreting the measurements.
Some general trends can be given:

1. the viscosity value is of the order of magnitude of 0.1 to 10 poise.
2. the viscosity decreases with increasing gas flow rate i.e. with increasing porosity.
3. the viscosity decreases with decreasing particle size ($50\ \mu m < \bar{d}_p < 400\ \mu m$).

2.2 Literature survey concerning the viscosity of fluidized powders

Synopsis

A review is given about the literature concerning viscosity of fluidized powders, summarized in three tables.

Table 2.1 Measurements with conventional methods in stationary, air fluidized beds

reference number	author	bed diameter (cm)	measuring method	powder	$\overline{d_p}$ (μm)	size range
1,2	Ashwin/ Hagyard	6.6 7.6	torsion pendulum	graphite coated shellac spheres	125.4/304.8	narrow
3	Grace	14	rising bubble	ballotini silversand synclyst catalyst magnesite	60/550 72/500 52 240	narrow narrow wide wide
4	Leont'ev	10.5	floating ball	quartz sand	220	narrow
5	Matheson	4.6	Stormer	synthetic cracking catalyst (spherical) catalyst (irregular) sand metaloxide (spherical) iron (irregular)	47/254 45/456 28/96 163 33	narrow narrow narrow narrow narrow
6	Kramers	8.6	Stormer	riversand	≈130 ≈180	rather wide rather wide
7,8	Ohmae/ Furukawa	6	Stormer	polyvinyl acetate beads	277/755	narrow
9	Diekman	10	Brookfield	cracking catalyst	57/73	narrow
10	Fa-Keh Liu	4.45	Brookfield	glass beads SiAl cracking catalyst Polystyrene beads	44/123 45 349	narrow narrow narrow
11	v.d.Leeden	1.0/ 5.0	Brookfield	spent cracking catalyst	≈70	wide
12	Botterill	14	Brookfield	bauxilite silica sand zircon sand	102 80/300 ≈150	narrow wide wide
13	Woodruff	6	Brookfield	silica powder titanium powder	20/60 25/50	narrow narrow
14, 15	Schügerl	7.5 13.25 14.5	Couette	glass beads alumina plates cork polystyrol quartz silica carbide	50/500 90 ≈50 250 75/450 45/190	narrow - wide narrow narrow narrow
16, 17	Lehman/ Ritzmann	19 36 50	Couette	quartz	160	narrow

fluidization	remarks	viscosity (range) (Poise)
heterogeneous	$1<u_o/u_{mf}<12$; viscosity decreases with increasing u_o and with decreasing $\overline{d_p}$	0.5/3
heterogeneous	the viscosity of the dense phase is the relevant quantity. The viscosity decreases with decreasing $\overline{d_p}$.	7/9.5 8/12 4 9
homogeneous + heterogeneous	the theoretical expression shows a decrease in the viscosity with increasing porosity.	1.8/5.4
heterogeneous	the viscosity decreases as the superficial gas velocity increases and particle size and particle density decreases. spherical particles show larger viscosity than irregularly shaped particles; paddles-speed: 200 r.p.m.	0.16/1.6 0.06/3.4 0.8/2.1 3.2 2.6
heterogeneous	$1.7<u_o/u_{mf}<2.9$ paddles are replaced by a dumb-bell. speed smaller than 30 r.p.m. The viscosity decreases with increasing u_o/u_{mf}	16/64 18/48
homogeneous + heterogeneous	paddle speed 113 r.p.m. the viscosity decreases as the flow rate increases and $\overline{d_p}$ decreases.	0.7/22.5
heterogeneous	channeling and bubbling occured in the bed. Higher particle density and coarser particles cause higher viscosity.	0.26/6.5
heterogeneous	two concentric, thin walled brass cylinders were rotated. Viscosity decreases with increasing flow rate, decreasing particle size, decreasing bed weight	1/4.6 0.3/1.8 1/4.6
particulate	rotation speed up to 100 r.p.m. the torque is independent of the rotation speed (0.5-50 r.p.m.); independent of roughness of the cylinder, of the bed diameter (6.5-9.0 cm), does not change when water is substituted for air!	no values for μ were given, only the torque in arbitrary units.
heterogeneous	a hollow cylinder is used.	no absolute values were given 15/80 arbit.units 40/70 arbit.units 0.16/3.75 0.16/0.2
packed bed/ homogeneous heterogeneous		1.4/67 - - 0.9/2.5 5.8/261 4.8/34
heterogeneous	measured viscosity depends on the location in the bed	

Table 2.2 Measurements with conventional direct methods in liquid fluidized

reference number	author	bed diameter (cm)	measuring method	powder	$\overline{d_p}$ (μm)	size range
18	Trawinski		falling ball	glass beads	900/10000	narrow
19	Prudhoe	3	falling ball	glass beads	2100	narrow
4	Leont'ev	10.5	floating ball falling ball	polystyrene balls	410/500	narrow

Table 2.3 Measurements of air fluidized powders flowing through open inclined or

reference number	author	channel length (m)	channel width (mm)	powder	$\overline{d_p}$ (μm)	size range
20	Mori	85	50	sand alumina bauxite	200 37 90	narrow wide wide
21	Siemes	2.0	150	quartz sand	217	wide
22, 23, 24, 25	Neuzil, Turcajova	.808 1.2	43	corundum glass beads sand	500 1000 1100	narrow narrow narrow
26, 27 28 29 30 31	Botterill		104/288	dune sand bauxilite catalyst ash	138/185 102 77 380/590	wide narrow narrow wide
32	Muskett	2.4	75	sand	150	-
33	Mc Guigan	3.0	100/150	sand	150	wide
34	Shinohara	1.2	42	glass beads	60-80 mesh	
35, 36	Woodcock	6	100	Corvic	140	wide
37	Singh	.75 1.5	41	sand	241	wide
38	Ishida	.954	39	glass beads porous alumina sand	160/390 230 190	narrow/wide narrow narrow

stationary beds

fluidizing medium	remarks	viscosity (range) (Poise)
water	$1<u_o/u_{mf}<6$. u_{mf} depends on flow region of the fluidizing medium.	2/220
oil		8.4/10.7
water		0.015/0.06
salt solution	inverted fluidized bed	

horizontal channels.

channel slope (degree)	fluidization range u_o/u_{mf}	viscosity (Poise)	remarks
1/15	-	-	Only superficial gas velocities have been given: sand: 5.6/11.3 cm/s alumina: 1.0/2.6 cm/s bauxite: 3/7 cm/s
1/6	3/6	1/9	
1/7	1.3/2.5	-	Only relative viscosities are given: $\mu(u_o)/\mu(2.5\ u_o)$ which value ranges from 1 up to 3.5
0	2/4 2/3.5 1.75/3 1.5/2.25	 ≈1 ≈1	a closed horizontal channel is used, flow is caused by paddles Viscosity values only order of magnitude.
4/8	-	-	Only the superficial gas velocity is mentioned ranging from 1.5 cm/s up to 4.15 cm/s
0/30	1.6/5.5	1/1.5	
7.5/15		0.01/0.2	Only the superficial gas 8 up to 18 cm/s is mentioned
0/12	2/12	-	
0/5	1.25/5	59	
14/23	0/3.7	-	

A review will be given of some literature results in order to see how other investigators tackle the problems. The review is summarized in Tables 2.1, 2.2 and 2.3.
Table 2.1 contains viscosity measurements in stationary air fluidized beds using conventional viscosimeters. For the sake of completeness Table 2.2 gives some measurements in stationary liquid fluidized beds. Measurements of air fluidized powders, flowing under gravity in inclined channels, or by artificially induced pressure head in horizontal channels are summarized in Table 2.3.

2.3 Remarks and discussion about the literature

Synopsis
The literature is briefly discussed. The measurements in a horizontal flowing fluidized powder are discussed in more detail.

Ashwin [1,2] reported measurements of the kinematic viscosity of the fluidized bed, ν. In order to compare these results with measured values of the dynamical viscosity μ they have to be multiplied by the bulk density ρ_b, which itself is a variable dependent on the superficial gas velocity (u_0). The actual dependence of ρ_b on u_0 is not reported, however.
The measurements of Grace [3] are based on a relationship between Reynolds number and included angle of spherical cap bubbles rising in liquids. The validity of the use of this relationship for bubbles rising in fluidized beds is doubtful as outlined already. The method excludes determination of non-Newtonian behaviour.
The viscosity is probably non-isotropic due to the greater transient velocities of the particles in the vertical direction than in the horizontal. It is well-known that the porosity near a rising bubble is larger than the dense phase porosity elsewhere. In view of the dependence of μ on ε this gives some doubt on the measurements.
The balls used in the measurements of Leont'ev [4] were coated with a varnish causing a very smooth, hard surface. So slip between the balls and the powder is not unlikely.
The measurements using a Stormer viscosimeter [5,6,7,8] are unreliable because of the very high rotation speeds used (up to 200 r.p.m.) which makes the occurrence of slip very likely.

The measurements of Kramers [6] used a dumb-bell, which was certainly not small compared to the bed diameter (75 mm and 86 mm respectively). The wall influence cannot be neglected in this case.
The use of a hollow cylinder [9,10,11,12,13] instead of paddles reduces the disturbances of the fluidized bed. But when no special preventions have been made slip will occur along the smooth side wall. When this slip is not measured the "viscosity" cannot be calculated correctly.
Another problem is the evaluation of the measuring results. The original Brookfield viscosimeter [9,11,13] is made and calibrated for Newtonian liquids, using the standard massive spindles. A calibration factor found by rotating the hollow cylinder in a Newtonian liquid is not a priori applicable to fluidized powders. Our measurements [40, 41] show a different behaviour of the fluidized bed inside the hollow cylinder and outside it.
The Couette measurements [14,15,16,17] are based on the assumption that the velocity gradient extends over the entire space between the two concentric cylinders. Our measurements [40,41], however, have revealed that the velocity gradient extends only over a few millimeters around the rotating cylinder, so the supposition about the extent of the velocity gradient will in general not be correct. This observation also rules out the possibility to describe the rheological behaviour as Newtonian.

The measurements in liquid fluidized beds [18,19,4] are, as pointed out already, not representative for air fluidized powders. The use of smooth, hard balls will cause the occurrence of slip [18,19,4]. The large ratio of particle diameter/measuring device size for particles of diameter exceeding 1000 μm using balls of 25 mm diameter is certainly inappropriate [18]. The discrepancy between measured and calculated values for μ and the absence of difference in measured value for 5200 μm and 10000 μm particles enforce the doubt.

The measurements summarized in Table 2.3 concern measurements in inclined or horizontal channels through which the air fluidized powder is flowing. Here too the fluidizing air velocity is mostly high: up to six times the minimum fluidization velocity. Although bubbles will be broken up by the flowing movement the fluidizing velocity is that

high that bubbles must have occurred, especially when using powders with a small range of homogeneous fluidization such as sand.

Many reports [20,32,35,36,38] are restricted to measurement of the mass flow rate of powder as function of the fluidization air velocity and the sloping angle. Sometimes [20,26/31,38] a velocity profile has been measured. But because of the different resistance against flow along the bottom plate and along the smooth glass side walls there will be a velocity profile in both directions perpendicular to the bottom and perpendicular to the walls. This is a complicating factor. Pressure drop measurements give the total resistance of the walls and the bottom together. In general moveable wall sections [26/31] or other devices to measure the wall shear stress directly are necessary to entangle both quantities otherwise one would be limited to the case where one of the shear stresses is negligible compared to the other, e.g. in very wide channels using very shallow beds. This procedure -measuring the total shear stress and the wall shear stress separately- reduces the accuracy of the determination of the shear stress at the bottom.

Siemes [21] derived values for the bed viscosity by measuring the mass flow rate, the bed height and the bed density, assuming that along the walls and the bottom no slip occurs.
On the assumption of the analogy between the flow of fluidized powders and liquids in inclined channels Neuzil and Turcajova [22/25] obtain a friction factor for fluidized powder flow. The functional dependence of the bed viscosity, supposed to be Newtonian, on the superficial fluidizing air velocity is supposed to be comparable to the functional dependence of the Newtonian liquid viscosity on the temperature.

Botterill [26/31] measured the powder velocity in a horizontal channel locally by means of a self-built device [38]: a kind of anemometer (a rotor with twisted blades). The frequency of rotation measures the "local" powder flow velocity. The device itself is that large (about 3x1 cm) that it is impossible to measure the velocity nearer than 20 mm from the wall. The averaged bulk velocity was measured with a float, submerged for 90% of the bed depth. The dimensions of the float cannot be found in the papers so it is not clear what part of the

vertical cross section of the channel is covered by the vertical cross section of the float. Which kind of "averaged" bulk velocity is measured in this way is not clear.
The difference in pressure head is the driving force for flow.
This implies a decrease in bed height in the direction of flow. The total shear stress across a certain section is measured by pressure drop measurements. The shear stress at the wall is measured by a moveable wall section. The shear stress at the distributor can be derived from these two quantities: the force due to pressure drop ΔP is the sum of the drag force acting on the vertical walls and the drag force on the distributor.
The equivalent diameter, D_e, is defined in the most recent paper [31] such that the differences in wall and distributor shear stresses are accounted for:

$$D_e = 4\ b.h/[(\tau_d/\tau_w)b + 2h]$$

where b is the channel width
h is the bed height
τ_d is the distributor shear stress
τ_w is the wall shear stress.

A simple power law model is used for the evaluation:

$$\tau = -\mu_a|\dot{\gamma}|^{n-1}\ \dot{\gamma}$$

n, the flow behaviour index is given by, using Rabinówitz equation:

$$n = \frac{d\ \ln(D_e\ \Delta P/4L)}{d\ \ln(8\bar{v}_d/D_e)}$$

Where L is the section over which the pressure drop is measured, $\bar{v}_d$ is the averaged bed velocity.
Using Rabinówitz equation again the shear rate can be obtained:

$$-\dot{\gamma} = \left(\frac{dv}{dr}\right)_{wall} = \frac{8\bar{v}_d}{D_e}\left(\frac{3n+1}{4n}\right)$$

The Rabinówitz equation only holds when the velocity at the wall is zero. The author states that visual observation showed this to be true.

Figures 2.1 and 2.2 show the flow curves for catalyst (77 μm) and ash (380 μm) at various gas flow rates. The flow curve for ash shows a transition from pseudoplastic behaviour (n<1) to dilatant behaviour

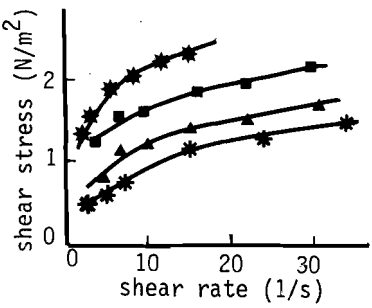

Figure 2.1
Flow curves, 77 μm catalyst in 140 mm wide channel (Botterill [31]).
✸ 1.5 u_{mf}, 85 mm bed height
■ 1.75u_{mf}, 87 mm bed height
▲ 2 u_{mf}, 90 mm bed height
✸ 2.5 u_{mf}, 94 mm bed height

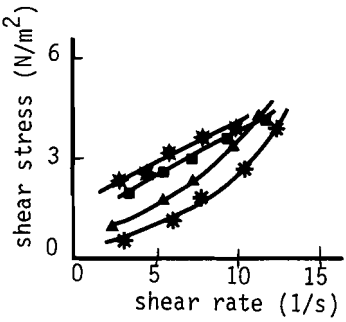

Figure 2.2
Flow curves, 380 μm ash in 140 mm wide channel (Botterill [31])
✸ 1.5 u_{mf}
■ 1.75u_{mf}
▲ 2 u_{mf}
✸ 2.5 u_{mf}

(n>1). This can also be seen in Table 2.4, which gives the flow indices and μ_a-values for ash, sand and catalyst. The flow indices for catalyst, ash and sand increase with increasing fluidizing gas flow rate, while the μ_a-values decrease with increasing fluidizing gas flow rate. The influence of the channel width on the flow index is not quite systematic: A weak tendency seems to be present showing for catalyst an increase in n with decreasing channel width (n<1) which means a more Newtonian behaviour in channels of small width.
For sand no systematic trend can be given. For ash a slight tendency can be seen showing a larger deviation from Newtonian behaviour with decreasing channel width. It is, however, not clear what the exact meaning is of n and μ_a (perhaps a kind of averaged profile?) because it is known, also by the author, that the velocity profile depends on the measuring height in the powder flow. This can be seen in Figures 2.3 and 2.4 showing velocity profiles at different heights, measured by means of the anemometer.

Material	Fluidization condition (u_o/u_{mf})	Channel width (mm)	n	μ_a
77 μm catalyst	1.5	180	0.23	1.5
70 mm packed bed	1.75	180	0.28	1.1
depth	2	180	0.43	0.7
	1.5	140	0.29	1.1
	1.75	140	0.13	1.0
	2.5	140	0.47	0.32
	1.75	120	0.30	0.64
	2	120	0.32	0.5
	2.5	120	0.34	0.32
	3	120	0.38	0.26
	1.75	100	0.3	0.48
	2	100	0.5	0.31
	2.5	100	0.6	0.12
	3	100	0.6	0.08
196 μm sand	1.5	180	0.69	2.25
90 mm packed bed	2	180	0.87	0.88
depth	2.5	180	1.3	0.3
	1.5	140	0.44	2.1
	2	140	0.5	1.8
	2.5	140	0.94	0.8
	3	140	1.08	0.8
	1.75	100	0.67	1.05
	2	100	0.96	0.66
	2.5	100	1.2	0.2
	3	100	1.5	0.04
380 μm ash	1.5	180	0.28	2.2
80 mm packed bed	1.6	180	0.44	1.6
depth	1.75	180	0.63	1.1
	2.25	180	1.0	0.2
	1.5	140	0.47	1.9
	1.75	140	0.58	0.8
	2	140	1.13	0.18
	2.25	140	1.42	0.06
	1.5	100	0.17	2.1
	1.6	100	0.44	1.25
	1.75	100	0.54	0.9
	2	100	1.0	0.1
	2.25	100	1.6	0.05

Table 2.4 The parameters n and μ_a of the power law for flowing fluidized powders (Botterill [31]).

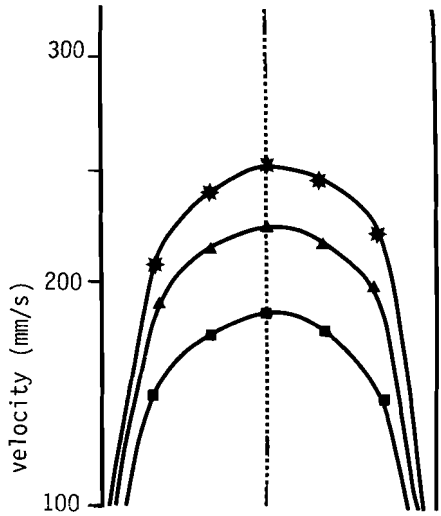

Figure 2.3
Velocity profiles across channel, 77 μm catalyst, u_o/u_{mf} = 2. 180 mm channel width, shear stress 1.8 N/m^2 at wall and 1.3 N/m^2 at distributor, average bed velocity 204 mm/s, height above distributor: ✸ 85 mm, ▲ 45 mm, ■ 25 mm (Botterill [30])

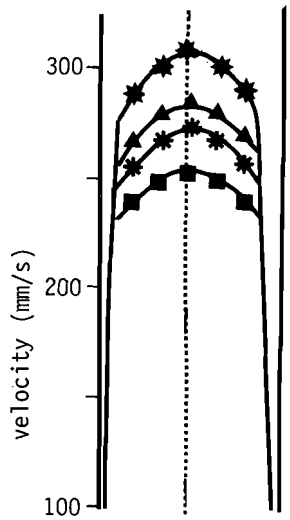

Figure 2.4
Velocity profiles across channel, 77 μm catalyst, u_o/u_{mf} = 2. 100 mm channel width, shear stress 1.3 N/m^2 at wall and 1.2 N/m^2 at distributor, average bed velocity 268 mm/s, height above distributor: ✸ 80 mm, ▲ 60 mm, ✸ 42 mm, ■ 20 mm (Botterill [30])

2.4 Conclusions and recommendations

Synopsis

Conclusions are made from the literature study for our measurements.

From the discussion given in the foregoing it is clear that to study the rheological behaviour of flowing powders the measurement of the velocity profile and the shear stress at the wall is the most suited method. To obtain reliable information care has to be taken to measure the velocity profile of the undisturbed flow. This rules out the use of devices such as rotating fans, which have to be put in the flowing powder. A method using radioactive labeling techniques has been developed (see chapter 4).

To avoid the problem of the presence of two velocity profiles -in horizontal and in vertical direction- an axisymmetrical system is

recommended. A vertically mounted circular pipe -a so-called standpipe- is appropriate. Because in that case the directions of powder flow and fluidization are parallel, all walls are equivalent and the shear stress at the wall is everywhere the same. The shear stress can be obtained from pressure drop measurement combined with simultaneous measurement of the bulk density of the flowing powder to account for the static head.

The regular stationary flow of fluidized cracking catalyst in a vertical, circular standpipe, connecting two fluidized beds is studied. The rig is called "huge sandglass" because of its resemblance of a sandglass and its dimensions (4.2 m height, volume of the beds $\pm$ 0.2 m^3 each). The huge sandglass enables quickly repeatable batchwise experimentation. To enable safe operation especially when using radioactive materials the whole system is completely closed, also the fluidizing gas flows form a closed loop.

The first experiments in the huge sandglass were carried out with a system of fresh cracking catalyst and air. This powder/gas system was chosen because it is frequently used in cracking installations and because it is a rather well-known system. The characteristics of the powder are summarized in Table 2.5.

Two methods are available for studying the flow behaviour:

1. Measurement of the shear stress at the wall, the averaged bulk velocity and the wall slip velocity.
   Using a modified Rabinówitz equation the rate of shear can be derived. Having derived the quantities τ_w, $\dot{\gamma}$ and v_w a rheological model can be fitted on the measuring results. This is a deductive way.
2. Measurements of the velocity profile directly and the shear stress at the wall.

Both methods have been used. The results and a comparison of the results of both methods are given in chapter 5.

Chemical composition:	SiO_2	74.03 wt.%
	Al_2O_3	25.02 wt.%
	SO_4	0.91 wt.%
	Fe	0.03 wt.%
	Na_2O	0.01 wt.%

Mean surface to area diameter, $\overline{d_p}$	73 μm
d_p range	up to 165 μm
relative spread in $\overline{d_p}$	0.45
particle density of the fraction used (containing 13.5 wt.% moisture on dry weight)	727 kg/m^3
skeleton density	2135 kg/m^3
internal porosity	0.70
internal pore volume	0.88×10^{-3} m^3/kg
surface area	540×10^3 m^2/kg
mean weight per particle	0.15 μg

Table 2.5 Characteristics of fresh cracking catalyst (High Alumina, High Pore Volume)

References

1 Ashwin, B.S., Haggard, T., Saunders, I.C.B., Young, T.E.,
Jl.Sci.Inst.37 (1960), 480

2 Haggard, T., Sacerdote, A.M.,
I. and E.C.Fundamentals 5 (1966),500

3 Grace, J.R.,
Can.Jl. Chem.Eng. 48 (1970) 30

4 Leont'ev, A.P., Vakhrushev, I.A.
Khim.Tekhnol.Topl.Masel 4 (1976) 35

5 Matheson, G.L., Herbst, W.A., Holt, P.H.
Ind.Eng.Chem. 41 (1949) 1099

6 Kramers, H., Chem.Eng.Sci. 1 (1951) 35

7 Ohmae, T., Furukawa, J.
Kogyo-Kagaku Zasshi 57 (1954) 788

8 Furukawa, J., Ohmae, T.
Ind.Eng.Chem. 50 (1958) 821

9 Diekman, R., Forsythe, W.L.
Ind.Eng.Chem. 45 (1953) 1174

10 Fa-Keh Liu, F., Orr, C.
Jl. Chem.Eng.Data 5 (1960) 430

11 v.d.Leeden, P., Bouwhuis, G.J.
Appl.Sci.Res. 10 (1961) 78

12 Botterill, J.S.M., v.d.Kolk,M., Elliott, D.E., Mc Guigan, S.
Powder Technology 6 (1972) 343

13 Woodruff, H.
Powder Technology 8 (1973) 283

14 Schügerl, K.
in Fluidization, Davidson and Harrison, Academic Press 261.

15 Schügerl, K., Merz, M., Fetting, F.,
Chem.Eng.Sci., 15 (1961) 1

16 Lehmann, J., Ritzmann, H., Schügerl, K.
Proceedings of the international symposium Fluidization and its
Applications. Toulouse (1973) 107

17 Ritzmann, H., Schügerl, K.
Chem.Eng.Sci. 29 (1974) 427

18 Trawinski, H.,
Chemie-Ing. Techn. 25 (1953) 229

19 Prudhoe, J., Whitmore, R.L.
Brit.Chem.Eng. 9 (1964) 371
20 Mori, Y.,
Kagaku Kogaku 9 (1955) 16
21 Siemens, W., Hellmer, L.
Chem.Eng.Sci 17 (1962) 555
22 Neuzil, L., Turcajova, M.
Coll.Czechoslov Chem.Commun. 34 (1969) 3652
23 Turcajova, M., Neuzil, L.
Scientific papers of the Prague Inst.of Chem.Techn. K11 (1976)
24 Neuzil, L., Turcajova, M.
Collection Czechslov Chem.Commun. 42 (1977) 599
25 Turcajova, M., Neuzil, M.
Collection Czechslov Chem.Commun. 42 (1977) 612
26 Botterill, J.S.M. v.d.Kolk, M.
AIChE Symposium series 67 (1971) 70
27 Botterill, J.S.M. Bessant , D.J.
Powder Technology 8 (1973) 213
28 Botterill J.S.M. Bessant , D.J.
Fluidization Technology, volume II, Dale Keairns 7.
29 Bessant, D.J., Botterill, J.S.M.
Proceedings of the international symposium Fluidization and its Applications. Toulouse (1973), 81.
30 Botterill, J.S.M., Abdul Halim, B.H.
Proceedings of the 2nd Engineering Foundation Conference 1978 April 78, Cambridge, 122
31 Botterill, J.S.M., Abdul Halim, B.H.
Powder Technology 23 (1979) 67
32 Muskett, W.J., Mason, J.S.
Pneumotransport 2, Sept. 1973, Guildford, paper F1
33 Mc Guigan, S.J., Pugh, R.P.
Pneumotransport 3, April 1976, Bath.
34 Shinohara, K., Sarto, K., Tanaka, T.
Micromeritics 19 (1974) 64
35 Woodcock, C.R., Mason, J.S.
Pneumotransport 3, April 1976, Bath, paper E1
36 Woodcock, C.R., Mason, J.S.

37 Singh, B., Callcott, T.G., Rigby, G.R.
Powder Technology 20 (1978) 99

38 Ishida, M., Hatano, H., Shirai, T.
Powder Technology 27 (1980) 7

39 Bessant, D.J.,
Thesis, Birmingham (1973) 31

40 Schenk, G., Rietema, K.
Internal Report, Eindhoven University of Technology

41 Schenk G.,
Viscosimetrie in een fluid bed, Internal Report, Eindhoven University of Technology (1979)

Symbols

b	channel width
D_e	equivalent diameter
$\overline{d_p}$	mean particle diameter
h	bed height
L	length of test section
n	flow behaviour index (power law)
ΔP	pressure drop
u_o	superficial gas velocity
u_{mf}	superficial gas velocity at minimum fluidization
$\overline{v_d}$	averaged bed velocity

Greek symbols

$\dot{\gamma}$	rate of shear
ϵ	porosity
μ	dynamical viscosity
μ_a	apparent viscosity
ν	kinematic viscosity
ρ_b	bulk bed density
τ	shear stress
τ_d	shear stress at the distributor
τ_w	shear stress at the wall

CHAPTER 3

THE HUGE SANDGLASS

3.1 Description of the apparatus

Synopsis

The experimental rig is described element by element.

1. Essentially the equipment consists of two circular fluidized beds above each other, connected by a vertical standpipe. The standpipe is situated at the centre of the beds. The standpipe is that long that a stationary flow pattern can be built up, when the powder flows down the standpipe in less than 15% of the discharge time.

2. The tilting mechanism.
   The frame in which the apparatus is mounted can be rotated about a horizontal axis. A motor with a mechanical delay (1:2), a chain-transfer and a cogwheel at the worm axis of the mounting frame enable two-sides rotation. Simple provisions have been made to prevent twisting of all electrical wires and manometer tubes etc. A special rotating coupling has been constructed for the fluidizing air supply pipes and of the air pressure cylinders. The system is made as follows: when the apparatus is rotated about 150^{o} a micro-switch is passed. A protuberance at the frame serves this micro-switch, which on its turn switches of the driving mechanism. The apparatus moves on by its inertia and stops when the apparatus is "almost" vertical again. The stopping point can be adjusted by replacing the already mentioned microswitch. When the apparatus is at rest, the frame can be blocked by two counteracting air pressure cylinders (coupled on the stationary frame) which are adjusted in such a way, that the rotating frame is exactly vertical when blocked. A rectangular block has been attached to the "bottom" and "upper" side of the rotating frame for blocking purpose. This principle has been proved to work correctly. Resetting of the microswitch was not necessary during months of working.

3. The fluidized beds.
   The fluidized beds are contained in two stainless steel vessels of about 200 liter volume each. The external diameter is 60 cm. The

bottom plate is built up of two perforated perspex plates and a porous flexolite plate (10 mm thick). This combination did give a homogeneous gas distribution and a sufficiently high pressure drop across the bottom plates.
Each fluidized bed has its own closed fluidizing gas circuit (see Figure 3.1). Gas is circulated by a compressor (Becker type GVO with with contraves KHM 250-c for control of the rotation speed). The gas pressure at the pressure side of the compressor can be kept almost constant by means of a gravitational valve in the compressor bypass (see Figure 3.1). An oil collector prevents oil of the compressor to be blown into the bed. A large dust collector, effective surface area 660 cm^2, mounted in the vessel in the return line, prevents catalyst powder to be entrained towards the compressor. The flow rate can be controlled by a needle valve.
When the fluidized powder flows downwards gas is sucked by the powder from the upper vessel towards the lower vessel. This extra gas would increase the gas pressure in the bottom vessel at the expense of the pressure in the upper vessel. The change in pressure drop across the standpipe would induce a change in the mass flow of powder. In order to maintain a stationary powder flow a gas bypass has been made from the pressure side of the lower compressor to the suction side of the upper compressor. A needle valve enables gas flow control. The gas flow in the bypass determines the powder velocity in the standpipe.
To transport the powder upwards through the dipleg and the standpipe the gas pressure in the bottom vessel has to be increased sufficiently. To realize this gas pressure increase a second gas bypass is mounted from the pressure side of the upper compressor to the suction side of the lower compressor. Magnetic valves enable choice whether the gas bypass lines are open or closed.

4. The standpipe and the dipleg.
The original idea was to invert the whole apparatus 180^o (like a sandglass) after each experiment. In that case there would be no need for a dipleg. Preliminary experiments have shown, however, that without the dipleg it was impossible to maintain a stationary and regular powder flow in the standpipe, i.e. a flow without bubbles, not exhibiting stick-and-slip flow. An additional advan-

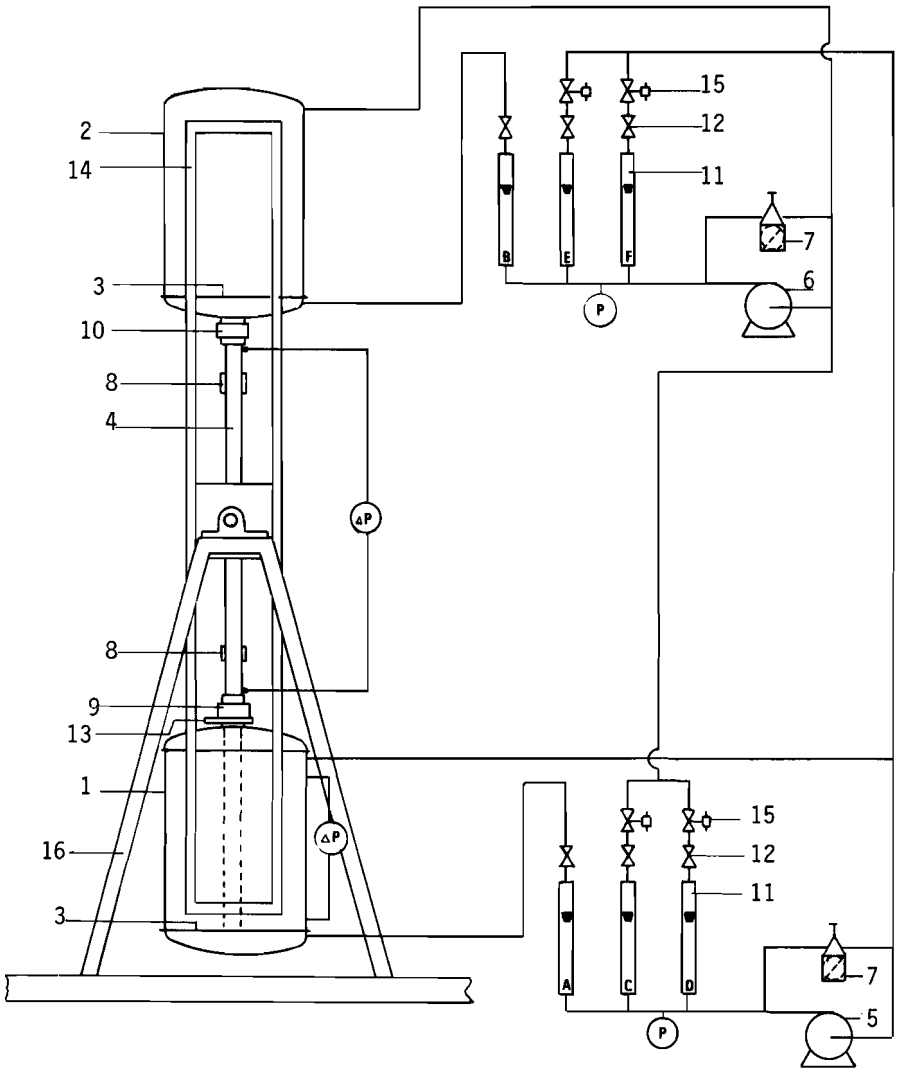

Figure 3.1 Schematic drawing of the equipment.

1. vessel A
2. vessel B
3. bottomplate
4. standpipe
5. compressor A
6. compressor B
7. gravitational valve
8. capacitive porosity measuring device
9. butterfly valve A
10. butterfly valve B
11. rotameter (A up to F)
12. needle valve
13. sieving apparatus
14. rotating frame
15. magnetic valve
16. stationary frame

tage of the dipleg is the possibility to transport the powder upwards through the dipleg and the standpipe without tilting the whole apparatus.

The visible part of the standpipe (see Figure 3.1) is 142 cm long. The internal diameter is 6 cm, external 7 cm.
Several pipes were used: a smooth glass pipe, a smooth perspex pipe and a perspex pipe roughened by a layer of silicone-rubber to which a layer of powder particles did adhere. In this way the influence of the shear stress at the wall could be studied roughly.
The standpipe is lengthened by a dipleg in the lower vessel. A brass pipe of 6 cm internal diameter plunges into the lower fluid bed, 4.2 cm above the bottom plate.

5. The butterfly valves.
The standpipe can be closed at both ends by two multiblade butterfly valves. The valves consist of siz trapezium-shaped segments, which all can rotate about their own axis of symmetry simultaneously (see Figure 3.2). A transition from circular to hexagonal cross-section and vice versa is built in. The valves are used to adjust the porosity in the down flowing powder at a chosen averaged powder flow rate. The position of the blades of the valve can be checked from the outside by means of a graduated scale.
The valves are operated pneumatically. Also the control pressure of the air pressure cylinders is an indication of the position of the blades but due to the hysteresis in the mechanical transmission, which is increasing with time, this is less accurate.
The relation between control pressure and position of the butterfly valve blades at one time is sketched in Figure 3.3. The hysteresis is eliminated by working with increasing pressure only. The valves are also used for hold-up experiments. The construction is made such that by pushing one button both valves close completely simultaneously.

6. The sieving apparatus.
Beneath the lower butterfly valve a mechanism is built in which enables a simple reliable separation of powder and labeled particles by sieving. It consists of a block containing two holes of Ø 60 mm

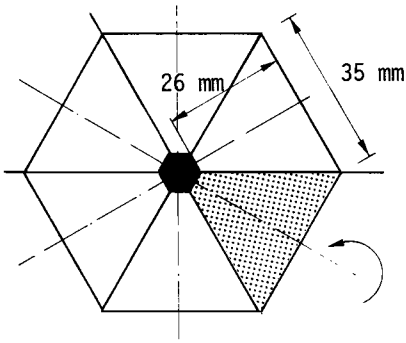

Figure 3.2
Sketch of a butterfly valve.
Full lines indicate the blades; dotted lines the axis of symmetry = rotation axis.
Black area: common, rigid centre.

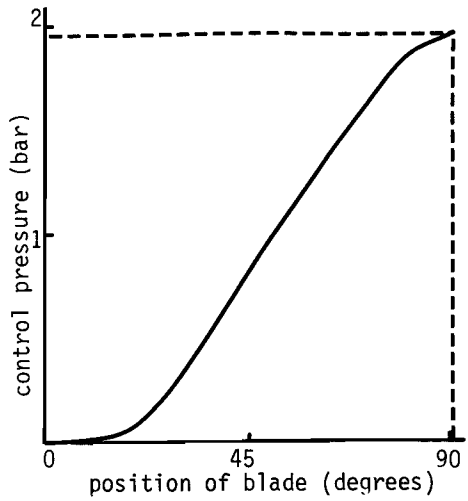

Figure 3.3
Sketch of the relation between (increasing) control pressure and blade position

(the internal diameter of the standpipe): one is really empty, the other contains a wire netting (500 μm), tilted 15^{o} with the horizontal (see Figure 3.4). This block can be moved to and fro in a rigid housing such that one of the holes is exactly in line with the standpipe. Operation is again pneumatically.
A rod is fixed to the moveable block, parallel to the driving axis. The rod has an asperity which serves one of two microswitches, indicating in which position the moveable block is.
Two control lights, corresponding to the microswitches, indicate in the control room the position of the sieve. To prevent blockage of the powder flow during sieving a pulsatory air flow is applied to the sieve. This is done by using a small compressor (reciprotor type YQ6 G) which sucks air from the bottom vessel and blows it in the standpipe just above the sieve surface beneath the powder column at a frequency of 60 Hz. To cover the whole sieve area the air is injected at two diametrically positioned points.
The labeled particles that are catched by the sieve can be easily removed from the apparatus using the tilting facility.
The construction is such that a hole is made in the upper plate of

the rigid housing of the sieve at the "out-position" of the sieve. A specially adapted lead container can be pressed at this hole. A construction with two springs and an air pressure cylinder is built. The springs press the lead container against the housing. When the lead container has to be removed the air pressure cylinder works against the springs. Sketch 3.4 might clarify the whole procedure: After sieving the hole of the moveable block is moved in the standpipe, the sieve is then out of the pipe, just beneath the lead container. The apparatus is tilted 180^{o}: the labeled particles fall into the lead container. The lead container is set free by switching the air pressure cylinder of the container and the container can be taken away. The procedure to put the freshly labeled particles in the system is just reverse and will not be described in full detail.
The lead container is put by hand in and out of the apparatus.

Ad Figure 3.4 (see next page)

1. moveable block of the sieve
2. rigid housing of the sieve
3. standpipe
4. butterfly valve
5. wire netting of the sieve
6. spring
7. lead container
8. mounting cover
9. adaptor
10. guiding rods
11. plate attached to 8
12. rigid plate attached to vessel
13. driving rod of 14
14. air pressure cylinder
15. driving rod of 1
16. indication rod with asperity
17. fixed rod with micro switches

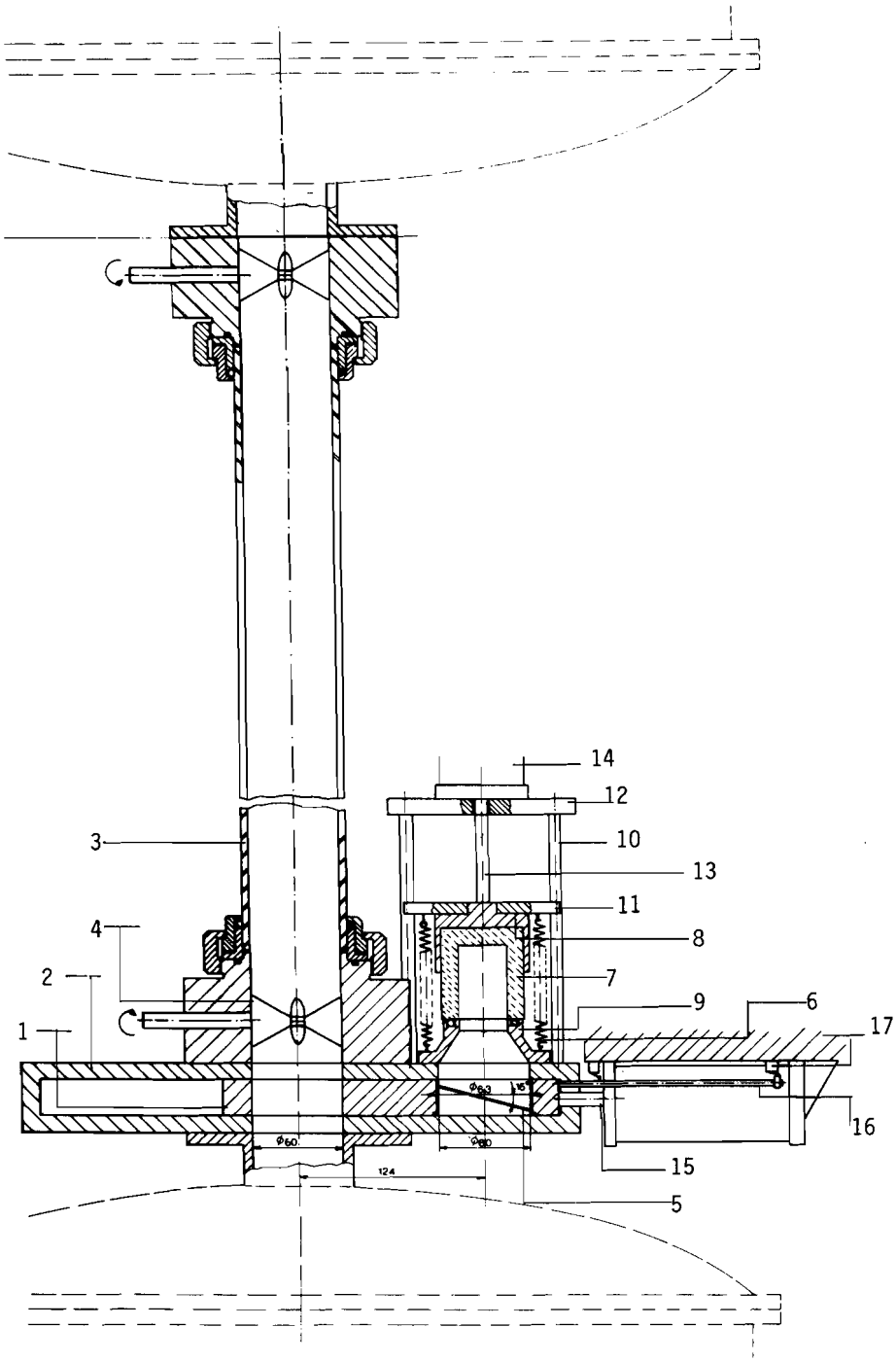

Figure 3.4 Sketch of the sieving installation.
For legenda see foregoing page.

3.2 The measuring system

Synopsis

The measuring devices, used in the so-called bulk measurements, are described briefly: the pressure drop meters and the measuring device for determination of the bulk density of the flowing powder. The principles of the bulk measurements are mentioned.

1. Gas flow rate measurements

All gas flows are measured by calibrated rotameters. Reference is made to Figure 3.1. Rotameter A measures the fluidizing gas flow rate towards vessel A. Rotameter B gives the fluidizing gas flow rate towards vessel B. The gas bypass flow rate at powder transport downwards is indicated by rotameters C for fast transport and D for slow transport. Rotameter E gives the gas flow rate in the bypass when the powder is transported upwards; while rotameter F gives the gas bypass flow rate when the powder is stationary in the standpipe. The accuracy of the gas flow rates measurements is about 1.5%, 1.5%, 0.6%, 0.6%, 0.6% and 0.6% full scale for rotameter A up to F respectively.

2. Pressure drop measurements

The pressure drop across the fluidized bed in vessel A is measured by a calibrated inductive ΔP-meter (Hottinger Baldwin 0.1 bar probe with kws 3073 measuring bridge; accuracy better than 1%). The analog output of the measuring bridge is recorded by a two-lines recorder. The pressure drop across 137 cm of the standpipe (between the butterfly valves) is measured by a calibrated inductive ΔP-meter (Hottinger Baldwin 1 bar probe with kws 3073 measuring bridge; accuracy better than 1%). The second line of the recorder is used to record the output signal of this measuring device.

3. Absolute pressure measurements

For safety reasons the absolute pressure in both vessels is measured too. The measuring points are located just above the bottom plates. Differential pressure gauges are used (range 0 - 1.4 bar for vessel A, range 0 - 4.0 bar for vessel B, accuracy for both meters 0.07% full scale).

4. Porosity measurements

The bulk density of the flowing powder is measured by means of a capacitive probe system.
Two flat brass plates (70 x 70 x 0.1 mm) are mounted in a perspex housing, which can be tightened around the standpipe, by means of two springs. The system is shielded electrically from the environment by a brass wire netting, fixed in the perspex housing. When the powder flows through the standpipe the dielectric constant of the medium varies, inducing a variation of the capacity of the "flat plate condensator". By means of a capacitive displacement meter (type CVM V v.Reysen electronics) of the bridge-type, and a probe (extra-sensitive probe 0-100 pF - v.Reysen electronics) the change in capacity of the "flat plate condensator" is translated into a voltage, which is recorded by a recorder.
To obtain easily interpretable results the system is calibrated using the standpipe as a fluidized bed, with a flexolite bottom plate and a known amount of powder. Each bed height can be converted to an overall bulk density and correlated to the output of the condensator system. If the water content of the powder is measured too in an independent experiment, the bulk density can be translated into an overall bed porosity.
Checks of the results of the flat plate condensator system against collaps experiments in the sandglass during powder transport gave the same results.
Preliminary experiments in the sandglass with two condensator systems at different heights showed that within the measuring accuracy (standard deviation in ε less than 0.4%) no porosity gradient over the length of the standpipe exists during downward powder transport.

5. Determination of the powder velocity at the wall

The powder velocity at the wall has been measured by visual observation of black painted powder particles. An amount of the powder particles has been painted by dipping them in black ink and drying them again. In this way no disturbing increase in weight of the particles is induced.
The black particles are followed over a distance of 200 mm and their time of flight is measured by a stop-watch. This method only works for

not too fast travelling particles ($v_w \leq 15$ cm/s) and if the wall of the standpipe is transparent.

6. The detection system

The detection system for the measurement of the velocity and radial position of individual particles will be described in chapter 4.
The frame bearing this detection system is mounted horizontally in the rotatable frame at 2/3 of the visible height of the standpipe.

The bulk measurements

With the devices described so far it is possible to determine the averaged powder velocity, the shear stress at the wall and the velocity of the powder particles at the wall.

i. The mass flow rate of powder through the standpipe equals the increase of powder per second in the lower bed. The powder content of a fluidized bed follows from the pressure drop across the bed and the bed surface area.

$$Q = \frac{\Delta P}{\Delta t} \cdot \frac{A'}{g}$$

where Q is the mass flow rate of powder through the standpipe (kg/s)
$\frac{\Delta P}{\Delta t}$ is the increase of the pressure drop across the fluidized bed per second ($N/m^2.s$)
A' is the surface area of the bed which equals the surface area of the bottom plate minus the surface area of the standpipe (m^2)
g is the acceleration due to gravity (m/s^2)

$\frac{\Delta P}{\Delta t}$ can be obtained from the recordings of the pressure drop across the lower fluidized bed versus time (see Figure 3.5). The slope of the straight part of the line gives $\frac{\Delta P}{\Delta t}$.
The bed surface area can be calculated knowing the internal diameter of the vessel (596 mm) and the external diameter of the standpipe (70 mm).

Q is directly related to the averaged powder velocity $\bar{v}_d$: $\bar{v}_d = \frac{Q}{A_{pipe}\,\rho_b}$

where A_{pipe} is the internal cross sectional area of the standpipe (m^2)

and ρ_b is the bulk density of the flowing powder, obtained from measurements by means of the flat plate condensator (kg/m^3)

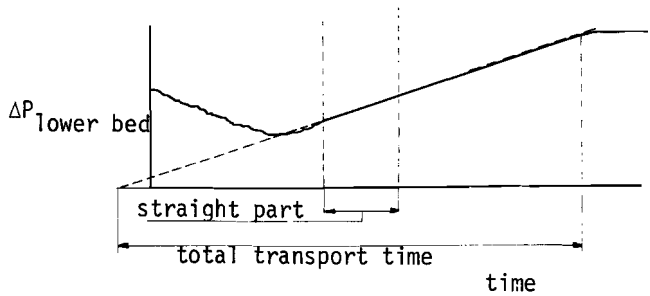

Figure 3.5 Output of the recorder of the pressure drop across the lower powder bed versus time during powder transport.

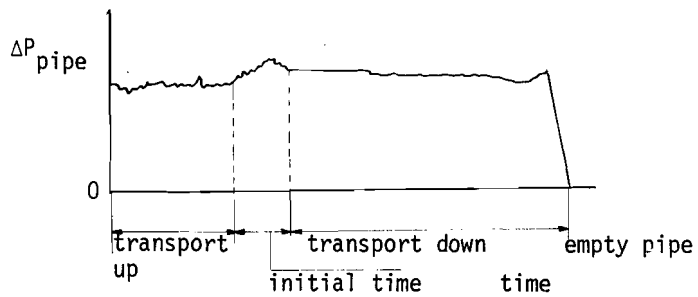

Figure 3.6 Output of the recorder of the pressure drop across the standpipe section (137 cm) versus time.

ii. The shear stress at the wall follows from the pressure drop across the standpipe (see Figure 3.6). For this cylinder symmetrical vertical system the relation between pressure gradient and shear stress at the wall runs as follows:

$$\tau_w = \frac{R}{2}\left(\frac{dP}{dz} - \rho_b \cdot g\right)$$

where τ_w is the shear stress at the wall (N/m^2)
R is the internal radius of the standpipe (m)
$\frac{dP}{dz}$ is the pressure gradient (N/m^3)

Preliminary experiments in which the pressure drop across various sections of the standpipe has been measured showed that the pressure gradient is constant. This means that a simple pressure drop measurement across a certain, known, length section of the standpipe gives directly the pressure gradient.
ρ_b and g have the already known meaning. Summarizing:
from pressure drop across the lower fluidized bed versus time and bulk density measurement (knowing the dimensions of the apparatus) follows the averaged powder velocity;
from the pressure drop across a standpipe section and the bulk density measurement (knowing the geometry) follows the shear stress at the wall.

Another interesting quantity that can be measured is the slip velocity i.e. the averaged linear powder velocity minus the linear gas velocity. The volume balance for our system during transport reads:

$$Q_{d,bypass} = Q_{d,solid} + Q_{d,gas}$$

Q_d is the volume flow rate.
The subscript bypass means: the gas flowing through the gas bypass from the pressure side of compressor A towards the suction side of compressor B.
subscript solid indicates: the powder particles flowing through the standpipe.
subscript gas indicates: the gas, entrained by the powder particles through the standpipe.
This equation can be rewritten in linear velocities:

$$Q_{d,bypass} = \bar{v}_d(1-\varepsilon)A_{pipe} + v_c \cdot \varepsilon \cdot A_{pipe}$$

where ε is the averaged bed porosity
v_c is the linear velocity of the continuum: gas.
Using the definition of the slip velocity it follows:

$$v_s = \frac{\bar{v}_d - Q_{d,bypass} / A_{pipe}}{\varepsilon}$$

$Q_{d,bypass}$ can be obtained directly from the rotameter readings (rotameter C or D, see Figure 3.1).

3.3 Criterions to obtain stationary powder flow

Synopsis

The criterions for stationary fluidized powder flow are formulated. The experimental conditions are given satisfying these criterions.

The vessels A and B are being fluidized heterogeneously. When powder transport occurs from vessel B to vessel A interstitial gas will be dragged along by the powder. This causes a pressure increase in vessel A at the expense of the gas pressure in vessel B. The displacement of powder increases the gas pressure in vessel A still more. This gas pressure increase in vessel A will cause irregular powder transport. To prevent this gas pressure increase a gas bypass line is mounted from the pressure side of compressor A to the suction side of compressor B (see Figure 3.1).

To transport powder through the dipleg and the standpipe in reversed direction the gas pressure in vessel A has to be increased. This can be realized by a gas bypass line from the pressure side of compressor B to the suction side of compressor A.

It will be clear that the fluidizing gas flows through the vessels A and B and the gas bypass flow will influence each other and also the regular powder flow. Only some combinations of gas flows will give a stationary powder flow in the standpipe (Figure 3.7). At lower bypass flow rates a stick-and-slip flow behaviour occurs, at higher bypass flow rates the start and end phenomena take unacceptable long time. The powder flow is considered sufficiently stationary if the following criterions are fulfilled:

1. ΔP_{pipe}, fluctuations less than 4%
2. ΔP_{bed} vs time: linear during more than 50% of the time of transport
3. ε, recorder output fluctuates less than 4%
4. visual observation: no stick-and-slip flow, nor bubbles are seen.

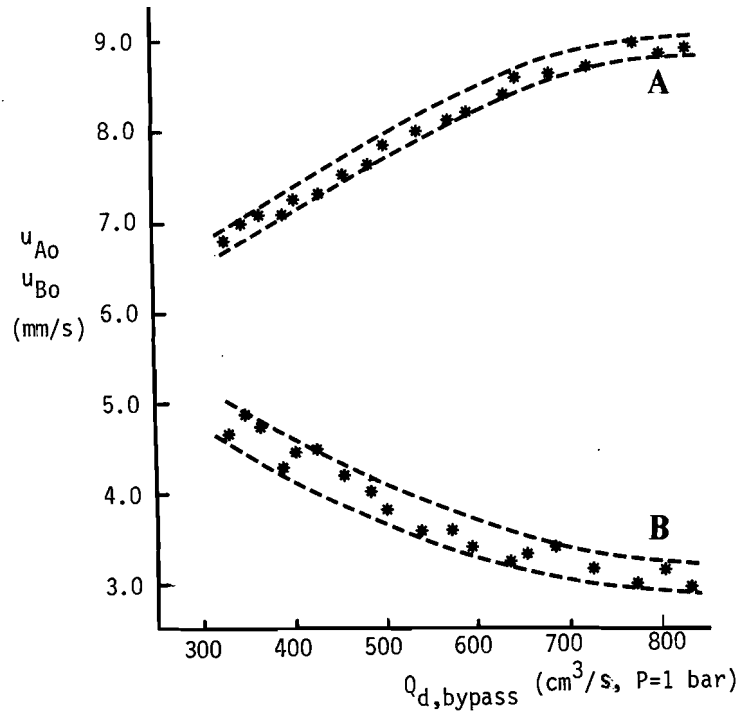

Figure 3.7 Combinations of gas flows giving stationary powder flow.

When $u_{A,o}$ is chosen lower than the values indicated by Figure 3.7 the porosity in the pipe is very low ($\varepsilon<0.4$), the powder transport is stagnant.
When $u_{A,o}$ is higher and $u_{B,o}$ is lower than indicated the "powder flow" is very irregular: the flow decreases, the bulk density increases, the pressure gradient across the pipe seems to change sign. Then the powder leaves the tubes as a plug with a relatively high velocity and the cycle starts again.
When $u_{B,o}$ and $u_{A,o}$ are higher than indicated the porosity is rather high ($\varepsilon>0.5$), the pressure drop across the pipe fluctuates and when $u_{B,o}$ is very high even bubbles originate in the pipe.

The bulk measurements involve measurement of the following quantities:

i. shear stress at the wall by measuring the pressure drop along 1.37 m of the standpipe and simultaneously the bulk density of the flowing powder.

ii. the averaged powder velocity by measuring the pressure drop across the fluidized bed in vessel A versus time and simultaneously the bulk density of the flowing powder in the standpipe.

iii. the velocity of the powder at the wall of the standpipe. When both butterfly valves are completely open the powder velocity at the wall is that high that visual determination is impossible. By closing butterfly valve B a little bit the mass flow rate of powder can be controlled, the gas volume flow rate through the gas bypass can be controlled by the needle valves C or D (see Figure 3.1). In this way it is possible to realize stationary fluidized powder flow in the standpipe at an averaged powder velocity sufficiently low to measure the powder velocity at the wall visually. This requires a suitable choice of the fluidizing gas flow rates A and B. The superficial gas velocity in vessel B should enable the supply of the maximum required powder flow rate from vessel B towards the pipe - no gas pockets should enter into the pipe.

The upper limit for visual observation of the powder velocity at the wall is about 0.1 m/s; the corresponding averaged powder velocity is of the same order of magnitude. This implies a maximum allowed powder mass flow rate of about 125 g/s. When the superficial gas velocity in vessel B is $u_{B,o}$ = 4 mm/s the required powder mass can be supplied.

The powder flows through the standpipe in the powder bed A. The superficial gas velocity in vessel A, $u_{A,o}$, should be that high that the incoming powder can easily be accepted by and mixed up with the powder in vessel A.

Table 3.1 gives some suitable combinations of $u_{A,o}$, $\bar{v}_d$, Q and butterfly valve position.

Q (kg/s)	opening of butterfly valve B (degrees)	$\bar{v}_d$ (m/s)	$u_{A,o}$ (mm/s)
45×10^{-3}	15 - 18 ^{o}	4×10^{-2}	3.5 - 5.0
75×10^{-3}	21 - 25	7×10^{-2}	4.0 - 6.0
110×10^{-3}	29 - 34	1×10^{-1}	5.0 - 6.5

Table 3.1 Combination of mass flow rate of powder in the standpipe, opening of butterfly valve B, averaged powder velocity in the standpipe and superficial air velocity in vessel A.

List of symbols

A'	surface area of the bed in lower vessel	$[m^2]$
A_{pipe}	internal cross sectional area of the standpipe	$[m^2]$
g	acceleration due to gravity	$[m/s^2]$
ΔP_{bed}	pressure drop across the fluidized bed in lower vessel	$[N/m^2]$
ΔP_{pipe}	pressure drop across the standpipe	$[N/m^2]$
$\frac{dP_{pipe}}{dz}$	pressure gradient across the standpipe	$[N/m^3]$
Q	mass flow rate of powder through the standpipe	[kg/s]
$Q_{d,bypass}$	volume flow rate of gas through the gas bypass	$[m^3/s]$
$Q_{d,solids}$	volume flow rate of powder through the standpipe	$[m^3/s]$
$Q_{d,gas}$	volume flow rate of gas through the standpipe	$[m^3/s]$
R	internal radius of the standpipe	[m]
Δt	time interval	[s]
$u_{A,o}$	superficial fluidizing gas velocity in lower vessel (A)	[m/s]
$u_{B,o}$	superficial fluidizing gas velocity in upper vessel (B)	[m/s]
v_w	wall slip velocity of the powder	[m/s]
$\bar{v}_d$	averaged powder velocity	[m/s]
v_c	linear gas velocity	[m/s]
v_s	slip velocity gas/powder	[m/s]

Greek symbols

ε	porosity of flowing powder	[-]
ρ_b	bulk density of the flowing powder	$[kg/m^3]$
τ_w	wall shear stress	$[N/m^2]$

CHAPTER 4

MICRO MEASUREMENTS IN THE HUGE SANDGLASS BY MEANS OF RADIOACTIVE LABELING TECHNIQUES

4.1 Why radioactive labeling?

Synopsis

Various methods for the measurement of velocity profiles are indicated. The feasibility of radioactive labeling is briefly discussed. An outline of the measurement of the position of the labeled particles is given based on physical principles. The fundamentals of the detection equipment are described.

To measure the velocity profile of stationary flowing powder in a standpipe directly there are two distinct methods.

i. Measurement of the local bulk velocity in a mechanical way using devices such as rotating fans, etc.
   This method implies insertion of obstacles in the flow, which certainly will disturb the flow pattern (see chapter 2). In fact a disturbed velocity profile is measured in this way.

ii. When the particles are (made) perceptable from the outside of the standpipe three different measuring techniques are available.
   a) Injection of tracer particles at a certain, well-known radial position and measurement of the passage time.
   b) Pulse response measurement either based on pulse-injection of tracer particles or based on a random distribution of tracer particles.
   c) Simultaneous measurement of the radial position and the velocity of a number of randomly distributed tracer particles.

   To ensure identical rheological behaviour of powder particles and tracer particles only a very small increase in weight (about 5%) of the tracer particles is allowed (see section 4.3).

   ad.a

   To ensure that the tracer particles behave like the bulk particles the injection level should be well above the measuring level. A large distance between injection level and measuring level is unacceptable if radial diffusion occurs, because this renders the

radial position determination unreliable.
Furthermore, it is very difficult to inject particles in such a way that they represent the undisturbed flow pattern.
Using a number of tracer particles mixed with the powder and determining the radial position of the tracer particles by sampling the powder just beneath the measuring level each time a tracer particle has passed is very difficult, time consuming and will certainly disturb the velocity profile.

ad.b

Pulse response measurements enable determination of the velocity profile if the following conditions are fullfilled:

1. There exists axial symmetry
2. There is no radial diffusion.

After creating a thin horizontal layer of tracer particles the number of tracer particles passing per second a certain level downstream the creation level has to be measured. From this number the velocity profile can be obtained under special conditions. (See Appendix 4.1).
Pulse injection of a plug of tracer particles gives a layer of tracer particles but will cause disturbance of the flow.
A possible alternative is a labeling technique which can be applied from the outside of the standpipe. Using for instance tracer particles containing a nuclide which can be activated a thin layer of activated radioactive particles can be created. Practically, however, it is impossible to find a nuclide which gives a sufficiently high radiation activity using the allowed, small amounts of nuclide, in the available time with common proton flux intensities.

ad.c

A method which enables simultaneous determination of the radial position and the velocity is preferred. Suppose a labeling technique can be found enabling determination of the distance of the tracer particle to the detector. Mixing up a number of tracer particles and determining the passage time and the distance to at least two detectors the radial position and the velocity of the passing tracer particles can be obtained.

The labeling technique

Radioactive labeling suits the conditions: the radio-activity of the particles does not disturb the flow pattern*), the particles are perceptable from the outside of the standpipe (also the particles in the bulk), the distance of the particles to the detector can be derived from the detected absolute radiation intensity if the radioactivity of the particles is known. If not so, more detectors are required. The relative radiation intensities enable calculation of the position of the labeled particle.
Chosen for radioactive labeling the question arises which kind of radiation is most suited. Ionizing radiation or radioactive radiation as it is often erroneously called can be divided in two main categories: corpuscular radiation (e.g. α, β^+, β^-, neutron radiation) and electromagnetic radiation (e.g. gamma and x radiation).
α particles are ruled out because of the very small range, just as β^- particles.
β^+ particles combine in material with free electrons i.e. both particles annihilate, emitting their mass energy as two photons of 510 keV each, which are emitted, because of momentum conservation diametrically. Using a β^+ emittor and detecting the two annihilation photons in fact the place where the annihilation took place is being determined instead of the place the β^+ particle has been emitted. This causes an additional uncertainty in the position determination of two times the range of the β^+ particle.
Neutrons are very difficult to collimate. Secondly the neutrons cause secondary corpuscular or gamma radiation. In general the entire environment is being activated. Furthermore, the half life time of neutron sources is generally rather long.
Gamma and x radiation. The difference between these two types stems from the origin of the radiation. While gamma radiation is being emitted when a radioactive nucleus falls back from a higher energy level towards a lower one, x rays are produced when an electron in

*) The radioactivity will cause ionization, which will reduce static electric charging. Because this phenomenon does not play a role in our system, the effect mentioned will be of no interest.

the shell around the nucleus falls back from a higher energy level towards a lower one.
In general the discrete energies of electromagnetic radiation (due to electron capture, photoelectric effect, e.g.) are characteristic for the radio nuclide involved in contrast to the continuous energy spectrum (due to Bremsstrahlung). This gives the possibility to reduce the background radiation of other radio nuclides by detecting only the electromagnetic quanta of interest in a small energy range.
From the foregoing it is clear that only gamma and x radiation are suited for our measurements.

Physical principles for the determination of the position of the labeled particle.

The intensity of electromagnetic radiation diminishes due to interaction with matter. The degree of attenuation depends on 1) the energy of the electromagnetic radiation, 2) the type of the absorbing material and 3) its thickness according to $I=I_0 \exp(-\rho.a.d)$ in which

I is the attenuated intensity
I_0 is the unattenuated intensity
d is the thickness of the absorber [m]
a is the mass attenuation coefficient of the absorber, which is a function of the photon energy [$m^2\ kg^{-1}$]
ρ is the density of the absorber [$kg\ m^{-3}$]

This relation describes the attenuation of a parallel beam of electromagnetic rays. The ratio I/I_0 is called the transmission coefficient.
However, the emission of electromagnetic radiation is purely isotropic. In that case, apart from absorption, the intensity at a distance r from the source is proportional to r^{-2}. This enables the determination of the distance between source and detector, knowing the source activity. If the source activity is unknown at least two intensity measurements are necessary.
It is almost impossible to produce labeled particles of uniform activity after activation in a neutron reactor, while also many other criterions play a role. This is caused by various reasons:

1. The non-uniform distribution of radio nuclide in the tracer particles.

2. The variation of the amount of radio nuclide per tracer particle.
3. The variation in geometry and size of the tracer particles.
4. The flux gradient in the reactor, the flux depression and the mutual shielding of the tracer particles during neutron bombardment.

Secondly the measurement of the absolute radiation intensity requires repeatedly an absolute efficiency calibration. An error made in this calibration gives a systematic error.
All these reasons tell strongly in favour of measurement of relative intensities using more detectors with known relative detection efficiencies. By using the r^{-2} law a first approximation of the distances to the detectors can be obtained. By using the absorption relation and again the r^{-2} law a second approximation can be obtained. In an iterative way the position of the source can be derived.

Fundamentals of the detection system

Anticipating the arguments that will be given in the next sections a short description of the ultimate detection system will be given.

The detection system consists of three identical detection chains, each made up of a lead collimator, a NaI(Tl) crystal with photomultiplier tube and preamplifier, a high voltage power supply, a main timing filter provided with differentiation and integration facilities, a discriminator, a logic interface and a counting register.
The three collimators are placed symmetrically around the standpipe at mutual angles of 60^{0}, enclosing the standpipe completely (see Figures 4.3, 4.5 and 4.6). Each collimator has two horizontal slits. The width of the slits equals the internal diameter of the standpipe. The time interval between the passage of these slits gives the vertical velocity of the labeled particle.
By measuring with a multiscale system in the time mode, i.e. by measuring the radiation intensity during successive time intervals, the response curve of the detection system is obtained. The shape of this response curve is determined by the velocity of the labeled particle, the radioactivity of the labeled particle, the detection system efficiency and the radiation absorption.

The detection efficiency of the system is determined by the efficiency of the detector with its electronics and the geometrical efficiency. The latter is a function of the collimator and slit dimensions and the position of the labeled particle in the horizontal plane. As outlined in the foregoing it is possible to derive the position of the labeled particle from the relative detected radiation intensities of the three detectors.

The tracer particles contain the nuclide $^{197}_{79}Au$. They are activated by neutron bombardment mainly to $^{198}_{79}Au$. This radio nuclide gives a gamma radiation, mainly with an energy of 412 keV. Its half life time is 2.7 days. The particles have a diameter of about 1.9 mm and a density equal to the bulk density of the powder (cracking catalyst, $\rho_{\ell_p} = \rho_b$ = 380 kg m^{-3})(see also section 4.3).

4.2 Detection system and data handling

Synopsis

First will be discussed the general criterions for detection, in particular the geometry of the collimators. The principles of the determination of the velocity and radial position of the labeled particles are outlined. The electronics are briefly mentioned. The principles of the computer program are given. Based on the required accuracy the minimal activity per labeled particle will be calculated.

The geometrical arrangement of the detection equipment

In order to be able to optimize the geometrical arrangement of the detection equipment, first the method to calculate the velocity and position of the labeled particle from the response curve should be chosen. If no radial displacement occurs and the vertical velocity is constant a graph of the number of detected gamma quanta versus time will look as sketched in Figure 4.1.
From A to B the particle comes in the field of vision of the detector. From B to C the particle is travelling at the height of the collimator slit. Going from C to D the labeled particle is getting lost from the field of vision of the detector.

The length of the plateau BC is determined by the particle velocity at known slit height.
The height of the plateau is a function of the geometrical efficiency, detector efficiency and the activity of the particle. At known collimator slit dimensions the geometrical efficiency is a function of the position of the particle only. The geometrical efficiency is calculated in Appendix 4.2. The slope of the curve between A and B is given by the particle velocity, geometrical efficiency and the plateau height.
The curves I and II in Figure 4.1 indicate the difference in response due to different particle-to-detector distances, other parameters being the same.
The curves I and III show the influence of the vertical velocity of the particle.
From comparison of curves I and IV the effect of the activity of the detected particle can be seen.

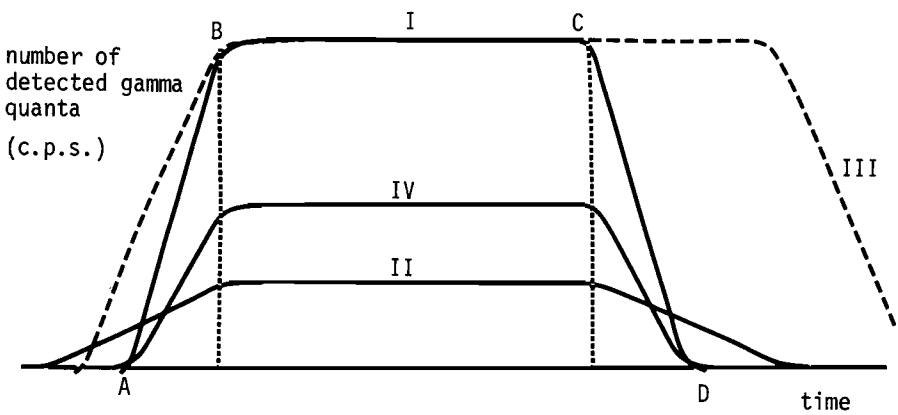

Figure 4.1 Time distribution of the number of detected gamma quanta during passage of a labeled particle in front of the detector.
I velocity v_0, activity A_0, distance to collimator d_0
II velocity v_0, activity A_0, distance to collimator d, $d > d_0$
III velocity v, $v < v_0$, activity A_0, distance to collimator d_0
IV velocity v_0, activity A, $A < A_0$, distance to collimator d_0

Essentially the velocity and the distance of the particle to the detector can be obtained from the response curve for a one slit system. In practice, however, difficulties occur due to the statistical fluctuations in the number of registered counts. Determination of the height involves the determination of the plateau height ($cts.s^{-1}$) as well as the background intensity ($cts.s^{-1}$). To obtain both quantities with sufficient accuracy a weighing procedure will be necessary. Before doing so the limits between which the quantities should be weighed must be determined. A logical choice for the plateau height seems the time interval between B and C. The determination of B and C, however, is rather difficult. It would necessitate to store all points of the response curve for mathematical manipulation afterwards. Due to the huge number of points and the high speed at which they are produced storage of all points is impossible with simple devices. This implies that in our case it was not possible to determine the particle velocity from the plateau length. The method using the slope of the curves give rise to problems due to the fact that the slope is rather large and that the method needs the knowledge of the particle distance. The method will be rather inaccurate due to statistical fluctuation and the use of another measuring result (particle distance).

The following procedure overcomes the problems and difficulties mentioned. By using a collimator with two horizontal slits the amount of information is doubled without the disadvantages of two detection systems with one slit each. Furthermore, use is made of the fact that the slope is rather large.

The principles of the procedures are the following:
A reference level is chosen well above the background level and well below the maximal counting level (the plateau height). The time the counting rate exceeds the reference level first is stored and from this time on the number of counts per measuring interval is summed until the counting rate is lower than the reference level. This time is also stored. For the second slit the same quantities are determined and stored. To elucidate the procedure the idealized response curve is sketched in Figure 4.2.

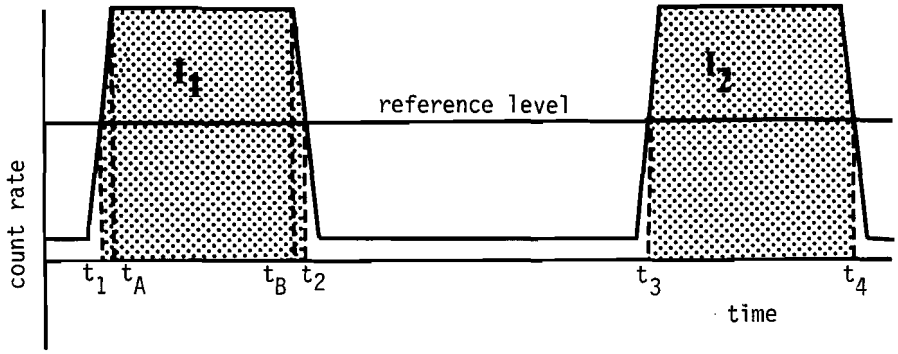

Figure 4.2 Idealized response curve of the passage of one labeled particle in front of the two-slit collimator. Indicated are the reference level, the points of intersection t_1, t_2, t_3 and t_4 and the sums of counts I_1, I_2.

The velocity can be obtained from the time intervals (t_3-t_1) and (t_4-t_2), knowing the geometry of the collimator. The slope being very high the plateau height can be assumed to be $I_1/(t_2-t_1)$ and $I_2/(t_4-t_3)$. Where I_i is the sum of the counts in interval $(t_{2i}-t_{2i-1})$.
As outlined already in section 4.1 the method of more detection systems is used, because the absolute radioactivity of the individual labeled particles is unknown. Because the position in the horizontal plane is described by two parameters at least three detection systems are required. One detection system is used as a "master": the times t_i are determined using this system. Of all passages I_1 and I_2 are determined. Thus one passage of a labeled particle gives ten measuring results:

t_1, t_1, t_3, t_4
$I_1(i)$, $I_2(i)$ $\quad i \in \{1,2,3\}$

The velocity is determined twice and the averaged value is stored as being the velocity of the particle.

The position can be obtained eight times by taking all possible combinations of $I_\ell(1)$, $I_m(2)$ and $I_n(3)$

$\ell \in \{1,2\}$; $\quad m \in \{1,2\}$; $\quad n \in \{1,2\}$

The averaged value of the eight results is used.

The discussion given in the foregoing leads to the choice of using three identical detection systems in a horizontal plane. Each detection system has a collimator with two horizontal slits. To ensure that each labeled particle in front of one of the slits is seen by all three detectors, the width of the slit equals the internal diameter of the standpipe.
For symmetry reasons the three detection systems are placed symmetrically around the standpipe (see Figures 4.3, 4.4, 4.5, 4.6).

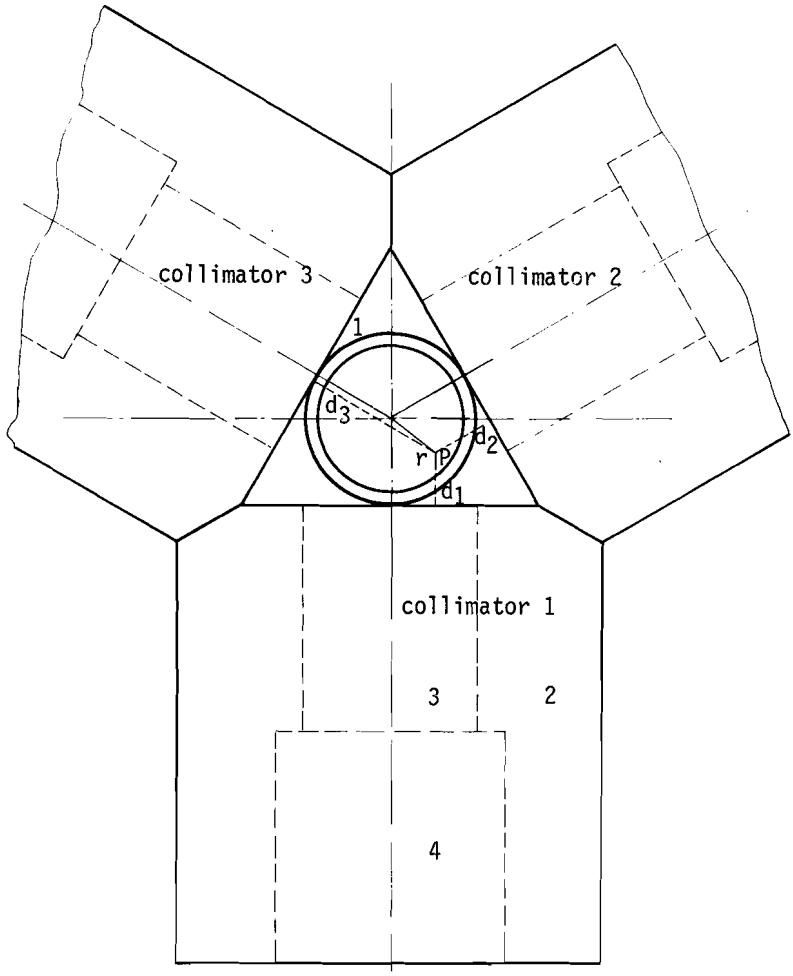

Figure 4.3 Sketch of the configuration of the three detectors. Horizontal cross-section.
1. standpipe 3. collimator slit
2. lead collimator 4. 3" x 2" NaI(Tl) crystal

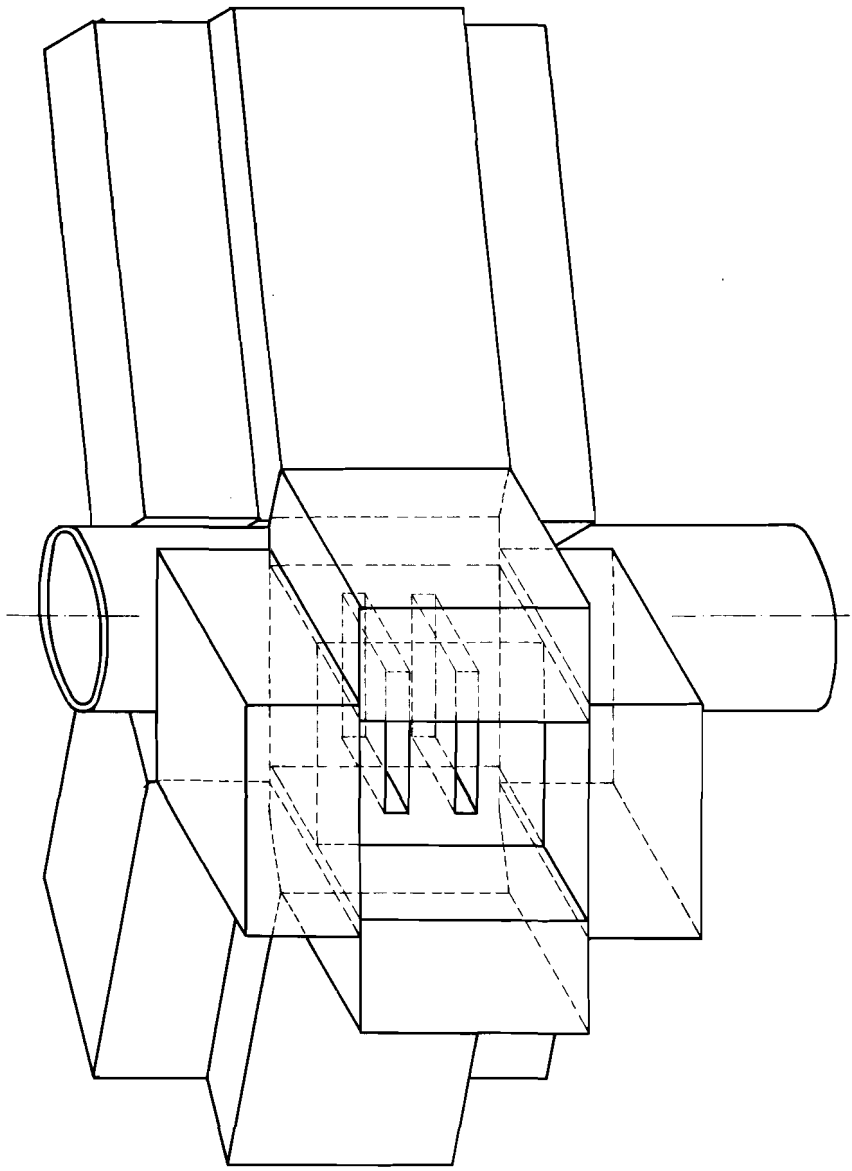

Figure 4.4 The arrangement of the three collimators around the standpipe. Only in one collimator the collimator slits are indicated.

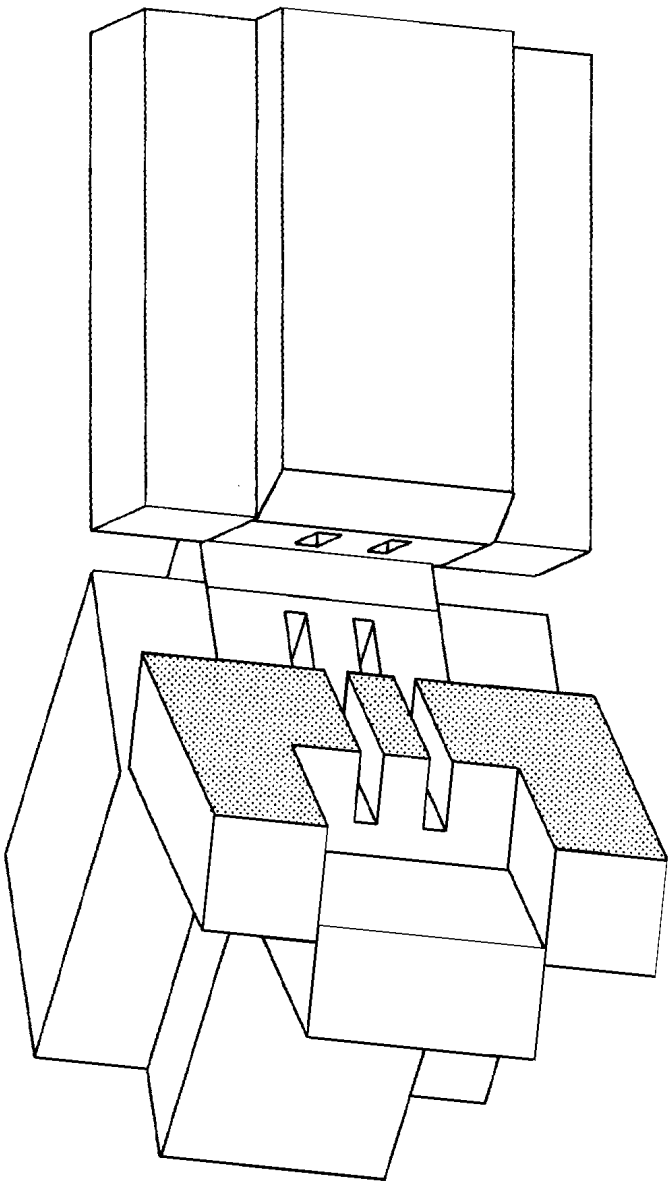

Figure 4.5 Look at the collimators. For the sake of clearness a part of the front collimator has been omitted.

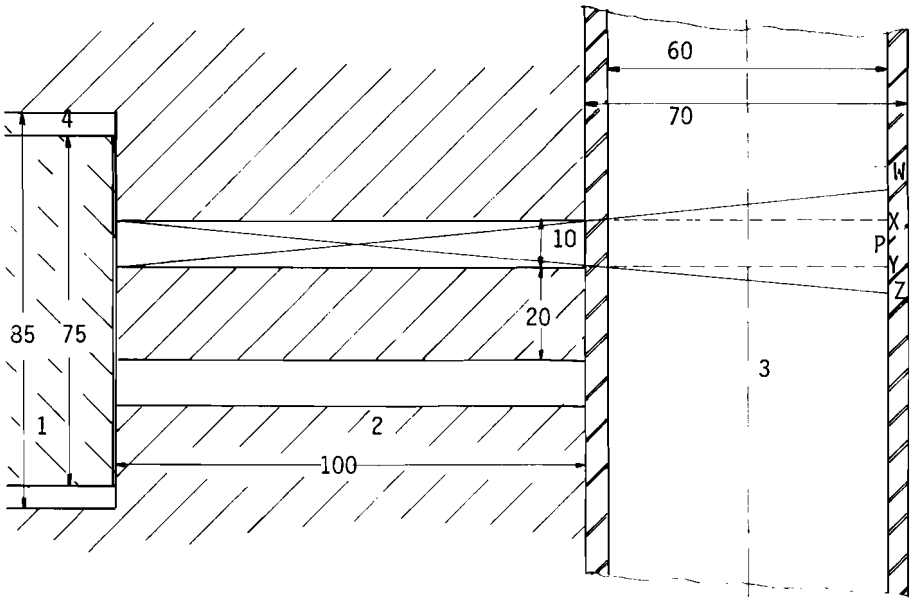

Figure 4.6a Vertical cross-section of the gamma detection system.

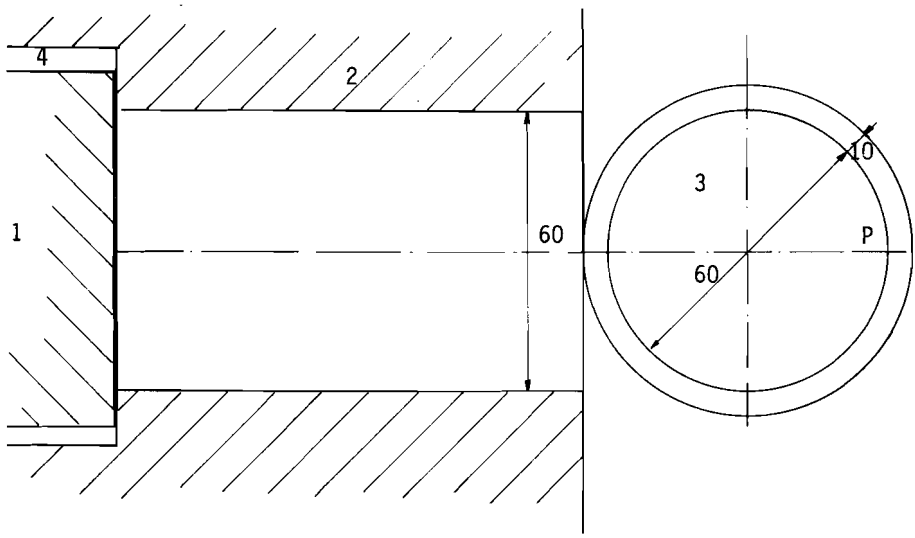

Figure 4.6b Horizontal cross-section of the gamma detection system

1. 3" x 2" NaI(Tl) crystal
2. lead collimator
3. standpipe
4. housing of crystal and photo-multiplier tube

All measures in mm

The dimensions of the collimator slits are: slit height = 10^{-2} m, the slit depth = 10^{-1} m and the slit width = 6×10^{-2} m.
The choice of these dimensions has consequences for the required activity per labeled particle required to obtain a certain accuracy. This will be discussed in section "Calculation of the required activity of the gamma emittor".
The distance between the two slits accounts for the following considerations.

1. The measuring method is based on the assumption that the radial displacement of the labeled particles, travelling from the first slit to the second slit is negligible. This implies that the diffusion length is much smaller than the distance between the collimator slits. The diffusion coefficient $\mathbb{D}$ of gases in air is of the order of 10^{-5} m^2/s. The Fourier length equals: $\sqrt{\mathbb{D}.t}$, where t is the passage time. Assuming the particle velocity is about 0.1 m/s and the slit distance is x.m the Fourier length is: $10^{-2}\sqrt{x}$.m.
   The condition reads: $x >> 10^{-4}$ m.
   This approach is in addition pessimistic because the unknown "diffusion coefficient of a solid particle in powder" can be expected to be much smaller than that of gases in air.
2. When two or more labeled particles are simultaneously in the field of vision of the collimator slits the interpretation of the detected signal will give rise to problems and errors, especially when faster travelling labeled particles overtake the slower ones. This is caused by the fact that the labeled particles cannot be distinguished individually.
   The probability that these problems occur can be reduced by reducing the total number of labeled particles in the system or the volume in front of the slits. The probability that more than one labeled particle is in front of the collimator slits can be calculated rather easily. The critical volume, i.e. the volume of the standpipe seen by the two slits and the volume inbetween, is calculated from the geometry (see Figure 4.7). The slit height is 10^{-2} m; the slit distance is x m. The slit depth is 10^{-1} m.
   h_2 equals $(x \times 10^2 + 2 \times 1.05)10^{-2}$ m
   h_1 equals 0.6×10^{-2} m
   The volume of the two sided truncated cylinder is:

$$V = \frac{\pi(6\times10^{-2})^2}{4} \times (x + 21\times10^{-3}) + 2 \times \frac{1}{2} \times \pi \times \frac{(6\times10^{-2})^2}{4} \times 6 \times 10^{-3}\ m^3 =$$

$$9\pi(x + 27\times10^{-3}) \times 10^{-4}\ m^3$$

The probability of m particles being present in volume V is

$$P\ [m \text{ particles in volume } V] = \frac{\lambda^m}{m!}\ e^{-\lambda}$$

where λ is the mean number of labeled particles in volume V. If the total number of particles in the system is N_t then

$\lambda = V \times N_t/(\text{total powder volume})$

The total amount of powder is 0.2 m^3. This implies

$\lambda = N_t \times 9\pi(x \times 10^3 + 27) \times 10^{-7}/0.2$

$$P[m\geq2] = 1 - P[m=0] - P[m=1]$$
$$= 1 - e^{-\lambda} - \lambda e^{-\lambda}$$
$$= 1 - e^{-\lambda}(1+\lambda)$$

A reasonable condition seems: $P[m\geq2] \leq 0.5\%$

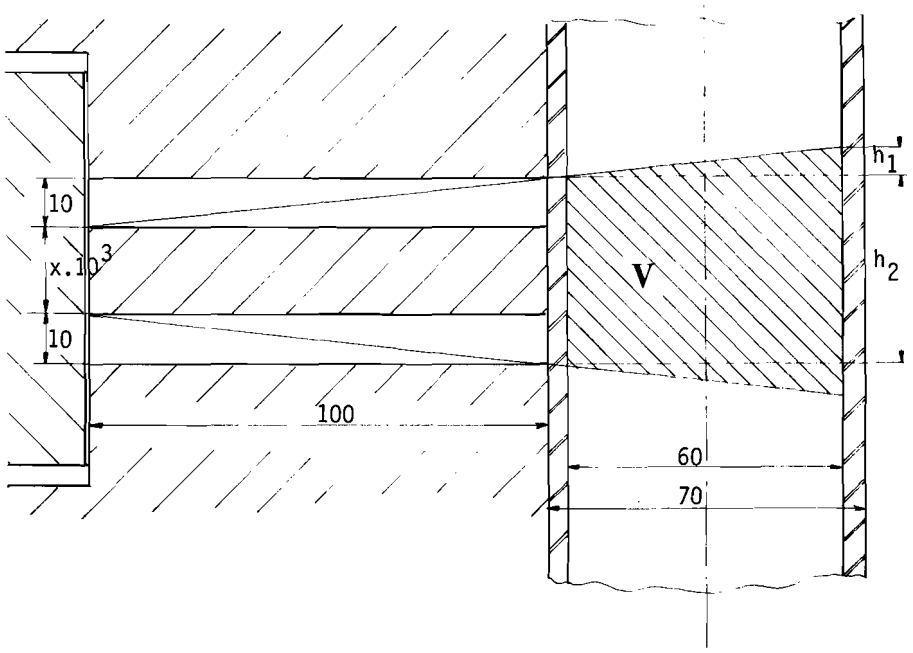

Figure 4.7 Standpipe with collimator. Indicated is the critical volume V. All measures are in mm.

Because a decrease in N_t decreases the amount of information obtained per measuring run it is not advisable to lower N_t at will. On the other hand from the point of view of health physics the number of labeled particles should be as low as possible.

N_t \ x	1	1.5	2	2.5	3
100	.13	.17	.21	.26	.31
150	.29	.38	.47	.58	.67
200	.48	.67	.80	1.00	1.17
250	.78	1.02	1.24	1.52	1.78
300	1.11	1.44	1.74	2.14	2.49

Table 4.1 $P[m \geq 2]$ (in %) as function of N_t and x

A reasonable choice for N_t is $100 < N_t < 200$ (see Table 4.1).

3. To reduce the relative measuring uncertainty in the velocity, which quantity has to be determined from two other quantities: time and distance, it is necessary to lower the uncertainty in both quantities. Because the absolute measuring uncertainty is fixed by the measuring devices, the only way to reduce the relative uncertainty is to increase the quantities themselves by increasing the distance between the slits.
The uncertainty in the measurement of the length is assumed to be 10^{-4} m; the relative spread is: $(10^{-4}/(10^{-2}+x))$. The averaged velocity will be of the order of 0.10 m/s. The uncertainty in the time measurement will be 2 channels (see section 4.2 "the detection"). The channel width is 1 msec. The relative uncertainty therefore is:

$$\frac{2.10^{-3}}{(10^{-2}+x)/0.1} = \frac{2.10^{-2}}{1+10^{2}.x}$$

While the relative uncertainty in the velocity will be:

$$\left(\left(\frac{10^{-2}}{1+10^{2}.x}\right)^2 + \left(\frac{2.10^{-2}}{1+10^{2}.x}\right)^2 \right)^{\frac{1}{2}} = \frac{\sqrt{5} \; . \; 10^{-2}}{1+10^{2}.x}$$

Requiring this quantity be less than 1% gives:

$$\frac{\sqrt{5}}{1 + 10^{2}x} < 1.$$

A value of $x = 2.10^{-2}$ (slit distance: 2×10^{-2} m) meets all the requirements, and this value is used in practice.

The detection and the data handling

The detection of the gamma quants takes place by means of three identical chains. A block scheme is given in Figure 4.8.
The detector is a NaI(Tl) crystal (3"x2") with a photomultiplier tube and a preamplifier. The preamplifier is a self-built system, essentially an emittor follower with amplification slightly less than unity. The pulses of the preamplifier are fed to a timing filter with facilities for differentiation, integration and transformation to uniform block pulses (aplification 2 up to 250, integration 200 ns, differentiation 100 ns). A discriminator transforms the fast negative pulses of the timing filter which exceed an adjustable threshold in standard negative pulses. The standard negative pulses are transformed to standard positive pulses in a logic interface and these positive pulses are fed to a counting register in the CAMAC interface system, which is coupled to the computer (PDP 11/03). The data handling is based on the multichannel analyzer method in the time mode, which is realized in the following way.
A timing register is made by feeding a counting register with pulses of a certain frequency (in our case 10^5 Hz) from a clock. When a certain number (in our case 100) of clock pulses has been counted by the timing register an inhibit pulse is given to the counting registers and the counting activity in these registers is stopped. In this way a channel time of 1 msec is made. One counting register is used as a reference counting register. The content of the reference counting register is compared to a reference channel level, which is chosen in between the background counting level and the counting level when labeled particles pass the collimator slits. If the content of the reference register is less than the reference level the counting registers are cleared and a new measuring interval (of 1 msec) is started. If the content of the reference register exceeds the reference level the contents of the counting registers are stored. The channel number, i.e. the number of the measuring time interval is stored too. Then the counting registers are cleared and a new measuring interval is started. As long as the new content of the reference

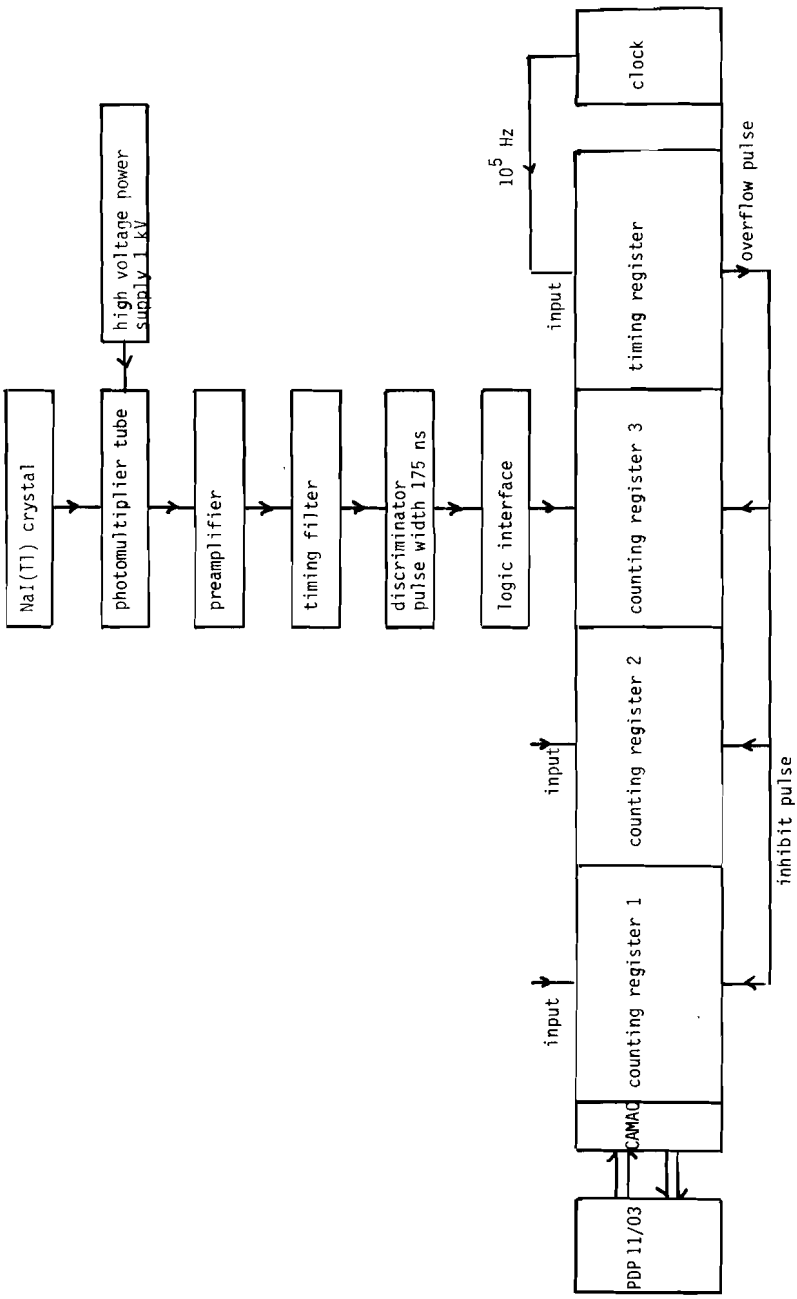

Figure 4.8 Block scheme of the data processing equipment.
Only one detection chain is indicated completely.

counting register exceeds the reference level the content of each counting register is summed with the contents of the foregoing measuring intervals. As soon as the new content of the reference counting register is less than the reference level the channel number is stored too. After a measuring run the begin channel number and stop channel number of each block (t_1 and t_2 respectively from Figure 4.2) and the sum of the channel contents during the time interval t_1,t_2 are stored. The sum of the channel contents is stored for all three detectors; the times t_1 and t_2 only from the reference register. These quantities enable the determination of the plateau heights and the block distances, which parameters are sufficient to derive the velocity and position of the labeled particles. The data are checked and selected based on several criterions.

1. A time criterion is used to find out which blocks can be ascribed to one particle passing the two slits.
2. The possibility that more than one labeled particle is in front of the collimator slits at one time is rather low in our case. Given the slit dimensions and chosing the total number of particles in the system equal to 100 an numerical value of about 0.2% follows from Table 4.1. A comparison of the contents of the two blocks, belonging to the passage of "a particle" enables determination of the occurrence of this phenomenon.
3. To minimize the effect of statistical fluctuations the following measures were taken:
   a. a three-point smooth routine is incorporated in the program deriving t_1 and t_2.
   b. when the number of counts in a number of channels within the block is less than the reference level the fragments of the block are collected to one block, if the length of the gaps is less than a certain number.
   c. when the number of counts in a small number of channels outside the blocks exceeds the reference level these pseudo-blocks are rejected if their lengths are less than a certain number.

When calculating the velocity of the labeled particles the real time per interval should be used: this time is a sum of the actual measuring time (chosen 1 msec) and the dead time of the computer (time required to carry out the instructions). This time was for the program used 200 μs.

To obtain the radial position the relation between plateau height and particle-to-collimator distance (given in Appendix 4.2) should be converted to a relation giving the particle-to-collimator distance as function of the plateau heights. This was done experimentally in calibration measurements, working with a single labeled particle, moving at known positions and velocity and measuring the plateau height in the already described way. From these calibration measurements it was found in first approximation:

$$\frac{1}{\sqrt{H_i}} = \sqrt{A}\,(\alpha_i d_i + \beta_i) \qquad (1)$$

where H_i is the plateau height of detector i
A is the activity of the labeled particle
d_i is the particle-to-collimator i distance (mm)
α_i, β_i are constants, dependent on detector efficiency and geometry (slit depth for instance).

This is the simple r^{-2} law (see section 4.1) and holds for particles at the centreline of the collimator.

A correction has to be applied for the sideways displacement, i.e. the distance x of the particle from the centreline.
The relation found experimentally and checked with the formulas of Appendix 4.2 is

$$H(x) = H(0)\ (1 - \gamma x^2)$$

where $H(x)$ is the plateau height at sideways displacement of x mm from the centreline.
γ is a constant, dependent on the distance d (mm)

$$\frac{1}{\sqrt{\gamma}} = 0.8148\ d + 83.16$$

The sideways displacement can be expressed in the distances d_1, d_2 and d_3 by:

$$x_i = \left| \frac{d_k - d_\ell}{\sqrt{3}} \right| \qquad \text{where } i,k,\ell \text{ cyclic}, \quad i,k,\ell \in \{1,2,3\}$$

This correction is always less than 5%.
The correction necessary due to the absorption is larger, up to 20% (see Appendix 4.3).

The plateau height decreases due to the absorption by the transmission factor: $\exp(-a\rho_b d_i^+)$

where a is the mass attenuation coefficient of catalyst (m^2/kg)

ρ_b is the bulk density of the catalyst (kg/m^3)

d_i^+ is the path length of the gamma rays in the powder and equals: $d_i^+ = d_i$ - wall thickness of the standpipe.

a can be calculated as is indicated in Appendix 4.3. a equals 0.00954 m^2/kg.

From the distances d_1, d_2 and d_3 the radial position can be calculated:

$$3r^2 = 4(d_1(0) - d_1)^2 + 4(d_2(0) - d_2)^2 + 4(d_1(0) - d_1)(d_2(0) - d_2)$$

$d_i(o)$ is the distance from the centre of the standpipe to collimator i ($i \in \{1,2,3\}$)

The program calculates essentially the radial position by using the above given principles.

From the relations 1 and the relation for d_i:

Σd_i = 108.4 mm (obtained from simple planimetry)

the following expression can be obtained:

$$\begin{Bmatrix} \frac{1}{\sqrt{H_1}} \\ \frac{1}{\sqrt{H_2}} \\ \frac{1}{\sqrt{H_3}} \end{Bmatrix} = (\text{matrix M}) \begin{Bmatrix} d_1 \\ d_2 \\ 1 \end{Bmatrix}$$

inversion gives:

$$\begin{Bmatrix} d_1^o \\ d_2^o \\ d_3^o \end{Bmatrix} = c\,(M^{-1}) \begin{Bmatrix} \frac{1}{\sqrt{H_1}} \\ \frac{1}{\sqrt{H_2}} \\ \frac{1}{\sqrt{H_3}} \end{Bmatrix}$$

using the calibration: $d_3^o = 1$ it follows

$d_i = d_i^o/d_3^o \qquad i \in \{1,2\}$

$d_3 = 108.4 - d_1 - d_2$.

The absorption of the gamma rays is accounted for by defining:

$H_i^{(1)} = H_i \exp(a\rho_b d_i^+) \qquad i \in \{1,2,3\}$

With these new H_i values the distances d_i are calculated by iteration until the difference between two successive calculated d_i values is less than a certain chosen value (0.5 mm). $|d_i^{(k)} - d_i^{(k-1)}| < 0.5$ mm. At last the correction for the sideways displacement is carried out by defining:

$$H_i^{(k)*} = \frac{H_i^{(k)}}{1 - \gamma x_i^2} \qquad i \in \{1,2,3\}$$

and calculating the d_i values again.
Because each passage of one labeled particle gives two values for H_i and because these two values should be the same, assuming the particle does not change its radial position eight combinations of d_i values are possible to obtain r:

$d_1(1), d_2(1), d_3(1) \rightarrow r_1$
$d_1(1), d_2(1), d_3(2) \rightarrow r_2$
$\vdots \quad \vdots \quad \vdots$
$d_1(2), d_2(2), d_3(2) \rightarrow r_8$

The averaged value of r_i is used as r.
The variation in the individual r_i values gives an indication of the accuracy of the measurement and the justification of the assumption, about the constant radial position. It turned out that the spread in r_i was about 4 mm, as could be expected based on dummy measurements. All measuring results were checked on this criterion, when the individual r_i values varied more than 4 mm the measurement was rejected.

Calculation of the required activity of the gamma emittor

The calculation will be given for the radionuclide $^{198}_{79}Au$ with a gamma energy of 412 keV.
The solid angle by which the detector is seen by a particle in the standpipe at maximal particle-to-collimator distance at point B is approximately 2.2×10^{-2} sterad (see Appendix 4.2). The geometrical efficiency equals:

$$\varepsilon^*_{geo} = 1.75 \times 10^{-3}$$

Going from B to C (see Figure 4.9) the geometrical efficiency is almost constant, going from C to D the geometrical efficiency decreases to 0. Assuming the reference count level is about half the plateau height

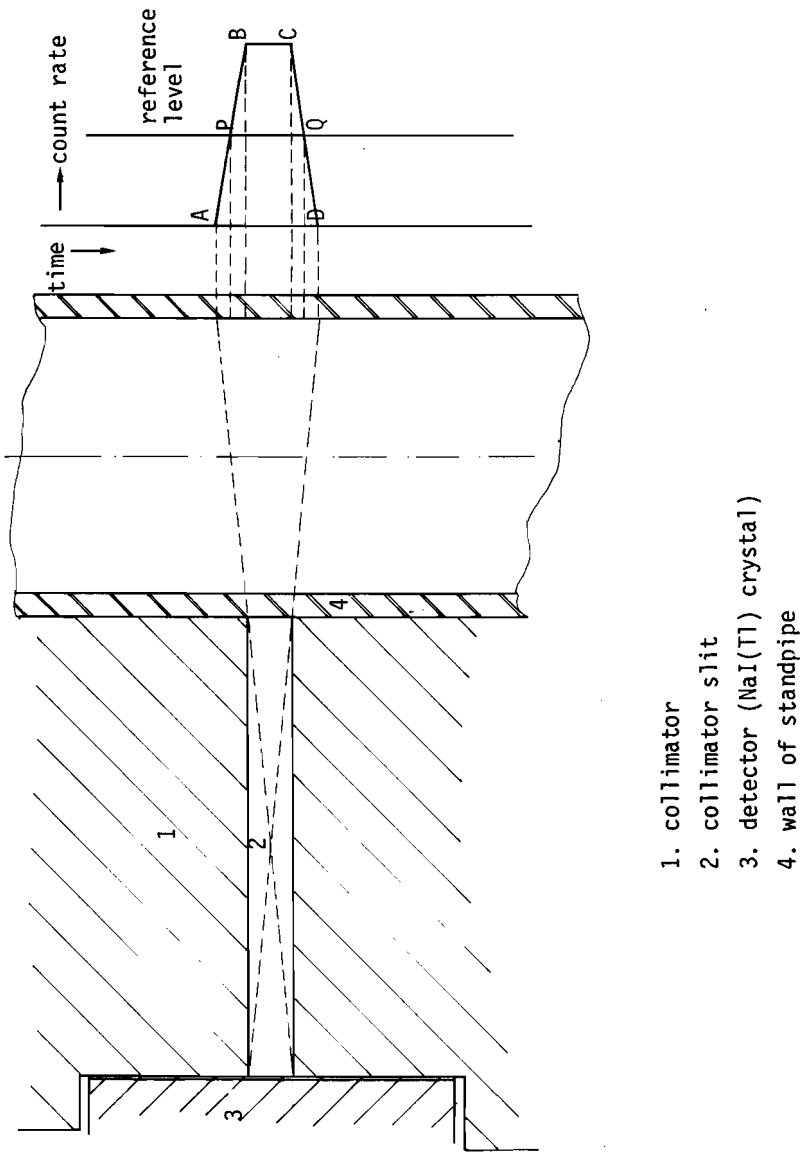

Figure 4.9 Sketch of the passage of a labeled particle in the standpipe. Particle-to-collimator distance maximum. At the right is indicated the response curve of the detection system (count rate versus time) with the reference level and the points of intersections (P and Q).

the geometrical efficiency in Q is $\varepsilon_{geo}(Q) = \frac{1}{2}\,\varepsilon^{*}_{geo}$. The averaged geometrical efficiency of the path length QC is $0.75\ \varepsilon^{*}_{geo}$. From the geometry the path lengths PB, BC and CQ can be calculated to be 3.25, 10 and 3.25 mm respectively.
The averaged geometrical efficiency over the total path length PQ equals:

$$\bar{\varepsilon}_{geo} = 0.902\ \varepsilon^{*}_{geo}$$

The total detector efficiency (Compton and photon effects) of a 3" x 2" NaI(Tl) crystal for 412 keV gamma quanta is 60% (see Figures 4.10, 4.11).
The total detection efficiency averaged over the measuring time equals:

$$\varepsilon = \bar{\varepsilon}_{geo} \cdot \varepsilon_{de} = 0.902 * \varepsilon^{*}_{geo} * 0.6 = 0.95 * 10^{-3}$$

The total number of detected gamma quanta during passage of a labeled particle with activity A (Bq) is:

$$N_p = A \cdot \varepsilon \cdot \frac{16.5}{v} \cdot 0.986 \cdot 0.8$$

The factor 16.5/v gives the time in which the particle travels from P to Q, if v is the particle velocity (mm/s).
The factor 0.986 accounts for the emission probability of 412 keV gamma quanta of $^{198}_{79}Au$, as may be seen in Figure 4.12.
The factor 0.8 accounts for the transmission of the gamma quanta through a layer of 60 mm of catalyst of density 400 kg/m^3 (see Appendix 4.3).
Taking for v an averaged value of 130 mm/s N_p equals: $0.95 * 10^{-4}$. A.
As outlined already about one hundred measuring points are necessary to obtain the response curve with sufficient accuracy.
Because the particles themselves are rather big in size (diameter 1.9 mm) (see section 4.1) it makes no sense to require an accuracy in the determination of the radial position better than 2 mm. This requirement implies a rather good statistic, thus a rather high count rate. Calculation gives that at least 40 cts per channel are required to obtain this accuracy.
This implies that the total number of counts per passage should be equal to or exceed: 4000. This leads to the requirement that the activity per labeled particle is at least 4.21×10^{7} Bq (1.14 mCi).

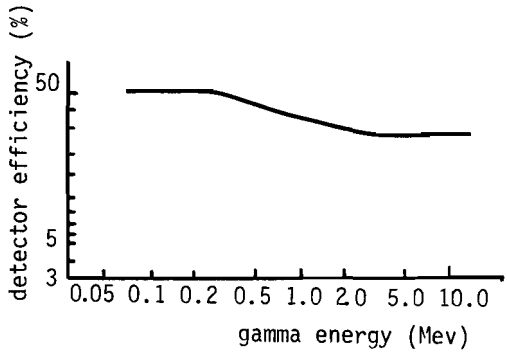

Figure 4.10 Total detector efficiency for a gamma source placed directly on a 3" x 3" NaI(Tl) crystal as function of the gamma energy ($\Omega = \pi$). (Reference Harshaw catalog).

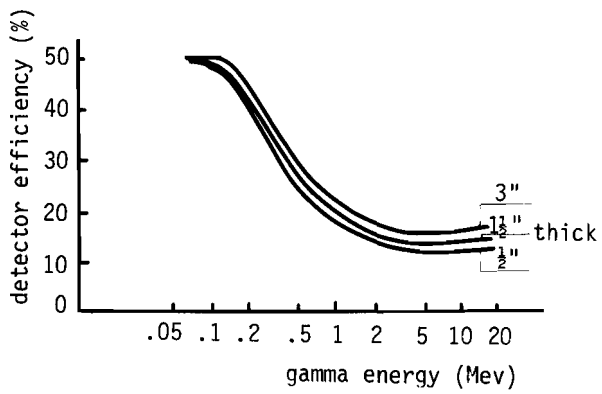

Figure 4.11 Total detector efficiency of NaI(Tl) crystal (1½" diameter) for a point source in contact with the crystal. ($\Omega=\pi$).(Reference Harshaw catalog).

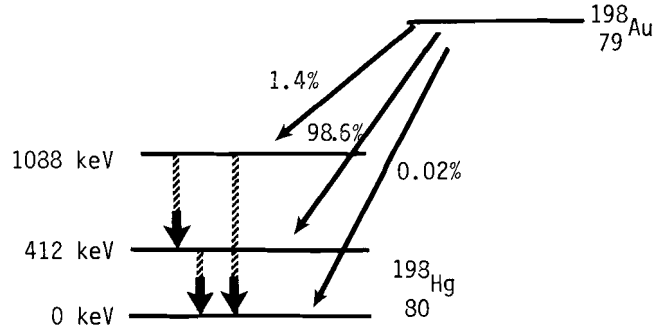

Figure 4.12 Decay scheme of $^{198}_{79}Au$.

4.3 The labeled particles

Synopsis

The production method of the labeled particles is described. The tests for checking whether the produced labeled particles satisfy the imposed specifications are briefly described and the results of the tests are summarized.

The labeled particles to be used should fulfill the following criterions in order to enable accurate and precise measurement of the velocity and the radial position of the particles and to guarantee safe and easy operation.

1. The slip velocity of the labeled particles relative to the powder particles should equal zero. The labeled particles should not disturb the powder flow and represent the velocity profile of the flowing powder.
2. Because the activity of the labeled particles is decreasing steadily it is necessary to refresh them periodically. An acceptable time interval is one week, which implies that the half life time of the active radio-nuclide must exceed 2 days. Therefore the labeled particles should be easily separable from the powder and removable from the experimental rig.
3. As outlined in section 4.2 the activity per labeled particle should be 4.2×10^7 Bq (1 mCi) per particle in order to measure the velocity and radial position with sufficient accuracy and precision.

Ad.1

The criterion that the slip velocity of the labeled particles relative to the powder particles is zero, implies that the drag force on the particle excerted by the powder equals zero and simplifies the force balance of the labeled particle. In the stationary case only three forces are acting on the labeled particle:

i. the Archimedes force
ii. the gravity force
iii. the drag by the gas flow.

The Archimedes force is given by:

$$\vec{F}_A = V_p \cdot \overline{\rho_b} \cdot g \, \hat{z}$$

The gravity force can be expressed as:

$$\vec{F}_g = -V_p \cdot \rho_{\ell p} \cdot g \cdot \hat{z}$$

where V_p is the labeled particle volume

$\bar{\rho}_b$ mean bulk density

$\rho_{\ell p}$ labeled particle density.

The drag by the gas flow can be expressed as (see Appendix 4.4):

$$\vec{F}_D = 30 \, \pi\mu \, v_s \, d_{lp} \, (\frac{1-\varepsilon}{\varepsilon})$$

where μ is the gas viscosity

v_s the slip velocity of the labeled particles relative to the gas, which equals the slip velocity of the powder relative to the gas

d_{lp} the labeled particle diameter

ε the external porosity of the flowing powder

This expression follows by equating the pressure drop across the labeled particle, as given by the Ergun relation for packed beds, to the sum of the drag forces acting on the labeled particles. Using the current values of the parameters, putting the particle volume 3 mm^3, the ratio $|\vec{F}_D|/|\vec{F}_A|$ can be estimated. It turns out to be much smaller than one ($\approx$0.05).

Neglecting the drag force the force balance reduces to:

$$\vec{F}_A + \vec{F}_g = 0$$

which implies that the density $\rho_{\ell p}$ of the labeled particle should be equal to the average density $\overline{\rho}_b$ of the powder.
The velocity of the labeled particle is assumed to represent the powder velocity at the same position. The position of the labeled particle is defined as the position of the centre of the particle. The particle velocity will be some mean value between the values at its boundary. This mean value may differ from the velocity at the centre, depending on the particle/standpipe diameter ratio and the velocity profile (see Figure 4.13).

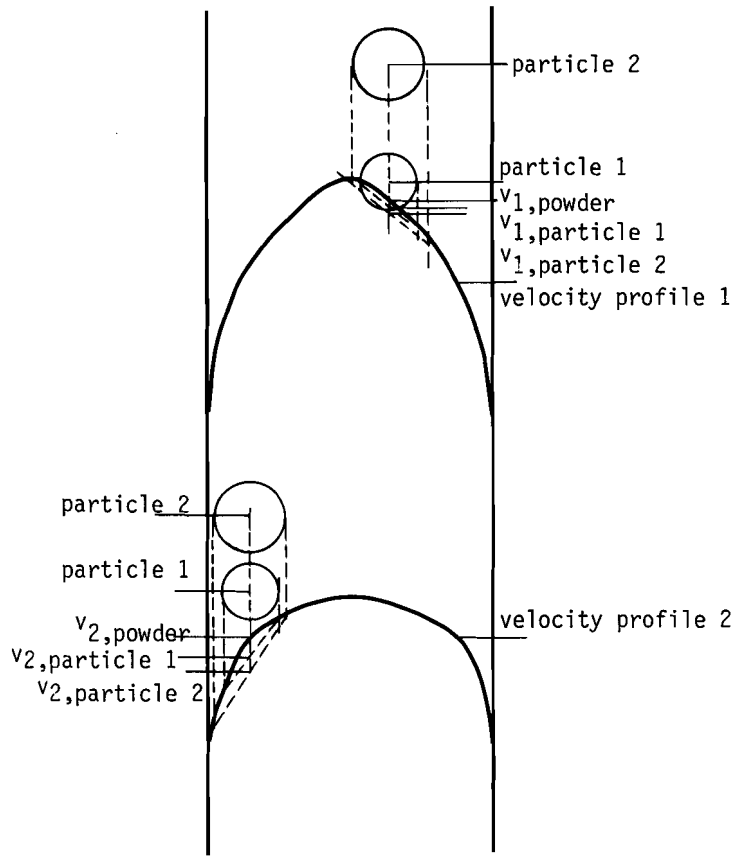

Figure 4.13 Illustration of the discrepancy between the measured velocity of the tracer particle and the powder velocity due to the dimensions of the tracer particle.

In the case of poiseuille flow this effect is given by Simha [1] to be:

$$\frac{\Delta v}{v_o} = -\frac{2}{3}\left(\frac{d_{lp}}{D}\right)^2$$

where Δv is the velocity difference of the labeled particle referred to the undisturbed bulk velocity (v_o) and d_{lp}/D is the ratio of the labeled particle diameter and the standpipe diameter (60 mm). Assuming the labeled particle diameter is about 2 mm, the relative velocity difference is approximately 0.08%, which is negligible.

Ad.2

Sieving, based on different size of labeled particles and powder particles is the most reliable method of separation. Quick separation with high efficiency is assured if the labeled particles size is at least ten times the average powder particle size.
This rules out the use of labeled powder particles and leads to the choice of labeled specially designed particles with a density equal to the bulk density of the flowing powder and a diameter at least ten times the powder particle diameter. The last criterion enables separation by sieving and the possibility to put a reasonable amount of radioactive nuclide in the labeled particles.

The choice of the radioactive nuclide

The following characteristics of the radio nuclide play an important role:

1. the attainable activity per labeled particle
2. the energy of the gamma quanta; E_γ
3. the half life time; $T_{\frac{1}{2}}$
4. practical aspects: easiness, cost, safety of preparation.

An additional criterion is that no other additional radioactive nuclides should be present in the labeled particles.

Ad.1

The activity per gram radio nuclide obtained by neutron bombardment can be expressed by the following equation if no secondary reactions occur:

$$A/G = \frac{dN^*}{dt} = \phi\ \sigma\ N\ \theta(1-e^{-\lambda T_b})\lambda$$

where A is the activity of G gram nuclide

N^* is the number of activated nuclei per gram nuclide

ϕ is the neutron flux (cm^{-2} s^{-1})

σ is the cross section for neutron reaction (cm^2)

N is the number of atoms per gram of nuclide to be activated, before bombardment (g^{-1})

θ isotopic abundance of the nuclide to be activated

λ is the decay constant ($\lambda = \ln 2/T_{\frac{1}{2}}$) ($s^{-1}$)

T_b is the time of neutron bombardment (s)

The detectable activity per gram radio nuclide of the selected energy equals:

$$A^*/G = B_f \cdot \frac{1}{1+\alpha} A/G$$

where B_f is the branching factor, indicating the ratio of the emitted gamma rays of different energies

α is the conversion factor, indicating which part of the selected transition does not lead to the emission of the selected gamma quanta.

Some remarks about the different parameters can be made:

ϕ depends on the neutron reactor

N is restricted by the criterion concerning the labeled particles density

θ should be as large as possible

σ should be large

B_f should be about 1

while α should be about zero.

T_b is restricted by cost and the possibility of damage of the labeled particles by the bombardment

remembering λ equals $\ln 2/T_{\frac{1}{2}}$ a high activity implies a short $T_{\frac{1}{2}}$.

Ad.2

The energy of the emitted gamma quanta is an important property for three reasons:

i. The absorption of the gamma quanta by the catalyst has to be small or at least the variation in absorption due to variation in the porosity of the bulk powder should be as small as possible. Therefore the gamma energy has to be rather high. Calculation reveals that the variation in the transmission in a layer of 6 cm catalyst, assuming a variation in the bulk density from

380 kg/m^3 to 400 kg/m^3 equals 47% and 1.4% for E_γ = 15 keV and E_γ = 200 keV respectively (see Appendix 4.3). These values show that a high gamma energy (about 100-500 keV) is favourable to reduce the influence of the density variations on the transmission.

ii. To obtain an optimal spatial resolution the geometrical efficiency should be very well defined. This requires a very precise collimation. Because the transmission of low energetic gamma quanta in lead is appreciable less than for high energetic gamma quanta, collimation of low energetic gamma quanta is easier to obtain, with less lead thickness than for high energetic gamma quanta. This implies a large source-to-detector distance for high energetic gamma quanta and so a small geometrical efficiency. The difference in transmission for low respectively high energetic gamma quanta also clarifies that the shielding problems occurring with high energetic gamma quanta are more serious than for low energetic gamma quanta. Also for safety reasons soft gamma rays are preferred.

iii. The detector efficiency of NaI(Tl) crystals depends on the gamma energy. The efficiency diminishes with increasing gamma energy and decreasing crystal diameter and thickness, as can be seen from Figures 4.10 and 4.11.

It can be concluded that a gamma energy in between 300-600 keV is appropriate.

Ad.3

The choice of the half life time of the radio nuclide is determined by several contradicting arguments.

i. The required high specific activity demands a short half life time. The activity of a nuclide is inversely proportional to the half life time.

ii. For safety reasons it is favourable to use a nuclide with a short life time because in that case the possible contamination of the equipment is less serious. When using radio nuclides with short half life time higher radioactivity values are allowed.

iii. In order to make efficient operation possible it is better to have a nuclide with large $T_{\frac{1}{2}}$. Because of the slow attenuation in activity with time the particles can be used longer. This saves

the time to separate the labeled particles from the bulk and the apparatus and to bring in new, freshly activated labeled particles. A rather good compromise is a half life time of 2-4 days. One week then equals about two half life times. In that case the attenuation in activity is a factor 4 and a batch of freshly activated labeled particles is sufficient for one week of experimentations.

Ad.4

i. The emission probability should be high, i.e. the main part of the desintegrations should lead to a gamma quanta of the desired energy which are emitted as such ($B_f \approx 1; \alpha \approx 0$).
ii. To reduce the total weight of the labeled particles the density of the nuclide should be low.
iii. The nuclide should be a solid of high chemical stability. The nuclide is not allowed to react with surrounding materials.
iv. The nuclide should be easily available and the cost should be acceptable. This implies that the need of enrichment to increase the abundance of the specific nuclide has to be avoided.

The nuclide which meets all requirements as best as possible is natural gold $^{197}_{79}Au$. The natural abundance of $^{197}_{79}Au$ is 100%. The neutron cross section of $^{197}_{79}Au$ (σ = 100 barn) is such that the attainable specific activity of the product ($^{198}_{79}Au$) in a neutron flux of 10^{13} neutrons/cm^{2}s in one day is approximately 5.10^7 Bq/g. The product $^{198}_{79}Au$ itself is a target for the neutrons, giving $^{199}_{79}Au$. But for the times of bombardments used ($T_b < 1$ day) and the neutron flux used ($\phi < 10^{14}$ neutrons/cm^{2}s) the secondary reaction is negligible. Furthermore a small amount of $^{199}_{79}Au$ is not too much disturbing: The gamma energy is low ($E_\gamma \approx 100$ keV) and the half life time is comparable ($T_{\frac{1}{2}}$ = 3.3 days). The calculation of the activities of $^{198}_{79}Au$ and $^{199}_{79}Au$ is given in Appendix 4.5. The energy of the gamma radiation is 412 keV, the emission probability is 98,6%. The decay scheme of $^{198}_{79}Au$ is given in Figure 4.12. The half life time is 2.7 days. As will be described in the following, it is possible to build labeled particles with a volume of about 3 mm^3, containing up to 29 weight% $^{197}_{79}Au$, with a particle density of 0.38 g/cm^3. The activity of one labeled particle just

after bombardment is 22.5×10^7 Bq (6.1 mCi), 7 days later the activity has been decreased with a factor 6 to a value of about 3.7×10^7 Bq (1 mCi). This was the activity required for our measurements.

So the required time of bombardment is less than one day. Compared to artificially made or enriched isotopes the cost of ^{197}Au is rather low. Gold powder is easily to handle, it is chemically stable.

Production of the tracer particles

The heart of the tracer particles are small polystyrene foam balls (density about 80 kg/m^3, diameter about 1.6 mm). These are coated with a two component resin, in which the gold powder is finely dispersed (2 x mg gold in 5 x mg resin is sufficient to coat x mg polystyrene balls).

The coated, sticky particles are loosened by gently rubbing with fine glass powder. The particles are dried during at least five hours at 70^{o}C and shaked during about half an hour on a shaking sieve to remove loosely attached glass powder. Then the whole procedure is repeated. The result are particles of about 1.8 à 2 mm diameter, with a density of about 380 kg/m^3, containing about 3.5 mg gold per particle. This amount suffices to obtain the required activity in neutron bombardment during 12 hours in the high flux reactor ($\phi = 10^{13}$ neutrons/cm^{2}s) of the Inter-University Reactor Institute of Delft.

i. The particles were selected on their density, related to their flow behaviour. The ultimate check was made in the sandglass itself. Tracer particles were put in the sandglass and after mixing with the powder they were transported through the standpipe up and down. The particles which did follow the powder movement could be removed by sieving. These particles were selected. Visual observation of the tracer particles in a two dimensional fluidized bed of cracking catalyst did not show any deviating behaviour.

ii. The particles were selected on their size by sieving. The fraction in between 1800 μm and 2000 μm was selected.

iii. The particles were also selected on their radioactivity after neutron bombardment. A large amount of labeled particles was put in a special container (Figure 4.14). The construction of the

container was such that the neutron flux for all particles was as equal as possible. The spread in resulting activity due to neutron flux variation etc. was first investigated by putting small pieces of brass of known weight in this special container. The spread in resulting specific activity of the brass pieces

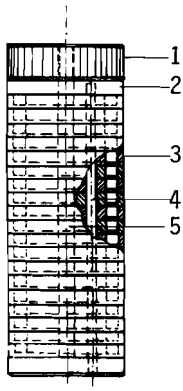

Figure 4.14
Sketch of the container for selection on the radioactivity of the labeled particles.

1. perspex screw
2. perspex end disk (Ø 25 mm, height 8 mm) without groove
3. perspex disk with groove (2.5 mm height, 3 mm width)
4. stainless steel match rod
5. plastic fixing rod.

was ascribed to neutron flux variation. A variation of about 10% was found. For activity spread measurement the tracer particles were put in the special container and activated slightly. Then the number of detected gamma quanta in the energy range around 412 keV of individual particles was compared.
This number is proportional to the radioactivity of the particles. All particles with an activity between 2/3 and 4/3 times the averaged value were selected. This was 68% of the total amount.

iv. The energy spectrum of the emitted gamma radiation of the activated particles was pretty clean: except the three peaks of $^{198}_{79}Au$ (412 keV, 676 keV and 1088 keV, in the correct ratio (see Figure 4.13)) only two very weak peaks at 1369 keV and 2754 keV were found due to ^{24}Na.

v. The attrition of the activated tracer particles was checked by fluidizing a number of activated tracer particles during a rather long time (147 hours) at a superficial gas velocity of 0.038 m/s in a bed of fresh cracking catalyst. The particles and the powder were separated and their radioactivities were measured separately. The activity of the catalyst was due to $^{198}_{79}Au$ as revealed the

energy spectrum of the emitted gamma quanta and was less than 0.001% of the activity of the particles. To check whether the particles could resist mechanically the high neutron flux and the increase in temperature during their stay in the reactor some particles were bombarded repeatedly (5 times, under conditions equal to the normal working conditions). These particles were fluidized 14 days at a superficial gas velocity of 0.01 m/s. The activity in the 412 keV peak of the powder was hardly measurable but was certainly less than 0.001% of the activity of the particles.

All these tests show that the tracer particles satisfy all the criterions that were made and that they can be used in the huge sandglass.

Appendix 4.1

Pulse response measurements by pulse activation

Theoretically it is possible to deduce the velocity profile by measuring the pulse response if

1. the totally measured activity is proportional to the number of particles.
2. axial symmetry exists.
3. a monotonous strictly decreasing or strictly increasing relation between velocity and radius exists.
4. neither radial diffusion nor radial velocity components occur.

Particles at a radius between r and $r+\Delta r$ have a velocity between v_r and $v_r+\Delta v_r$. These particles pass the measuring level in the time interval $t-\Delta t$ and t. If L is the vertical distance between the activating level and the measuring level then

$$t-\Delta t = \frac{L}{v_r+\Delta v_r} \; ; \quad t = \frac{L}{v_r}$$

The number concentration of tracer particles at the activating level is c. The number of tracer particles that pass the measuring level having a velocity between v_r and $v_r+\Delta v_r$ equals: $c.v_r.2\pi r.\Delta r$.
This is a fraction of the total number of tracer particles passing the measuring level:

$$\frac{v_r.2\pi r.dr}{Q_d} = f(r)\ dr = g(v)dv$$

where Q_d is the volume powder flow.
Because passage time and velocity of the tracer particles are related by the pathway L it holds

$$g(v)dv = h(t)dt$$

and

$$g(v) = h(t)\ \frac{dt}{dv} \qquad (1)$$

The measurement will give the number of tracer particles passing the measuring level as function of the time. So the function h(t) can be obtained. This function can be converted to the function g(v) by relation (1).

Define a function $G(v^*)$ (see Figure A4.1.2) by

$$G(v^*) = -\int_{v_{max}}^{v^*} \frac{g(v)}{v}\,dv = \int_0^{r^*} \frac{v(r)\,2\pi r\,dr}{Q_d v(r)} = \frac{2\pi}{Q_d} \cdot \frac{r^{*2}}{2}$$

By inverting the relationship $G(v^*)$ to a relationship $v^*(G)$ Figure A4.1.4 can be obtained and by taking the square root of the abscissa Figure A4.1.5 results. As an illustration the procedure is elucidated for a parabolic velocity profile with non-zero wall slip velocity in Figure A4.1.1 to Figure A4.1.5.

The assumption of homogeneous number concentration of tracer particles is rather doubtful, because the porosity in a layer of a few particle diameters thickness at the wall of the standpipe will be higher than anywhere else in the standpipe.

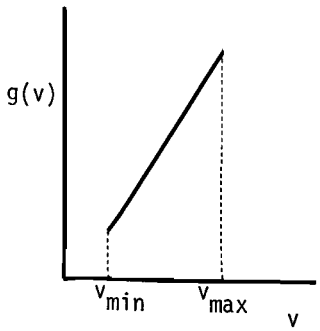

Figure A4.1.1

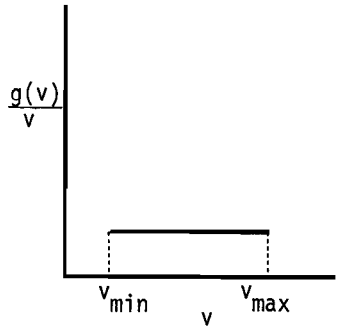

Figure A4.1.2

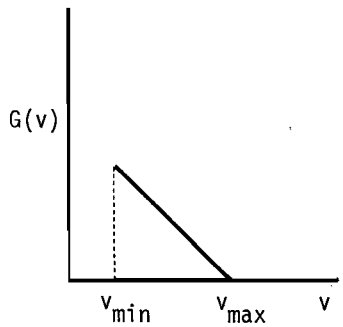

Figure A4.1.3

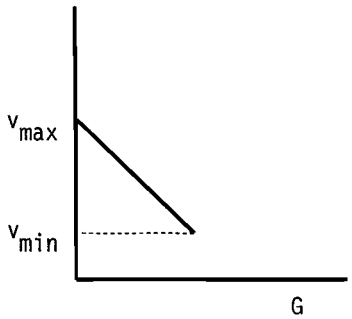

Figure A4.1.4

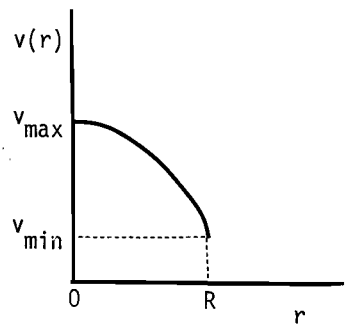

Figure A4.1.5

1. $g(v) = \frac{\pi}{Q_d} v = \frac{v}{v_o R^2}$

2. $\frac{g(v)}{v} = \frac{\pi}{Q_d}$

3. $G(v) = (v_{max}-v) \frac{\pi}{Q_d}$

4. $v(G) = v(\frac{\pi}{Q_d} r^2) = -\frac{Q_d}{\pi} .G + v_{max}$

5. $v(r) = v_{max} - r^2$

$$Q_d = \int_0^R v(r) 2\pi r \, dr = (v_{max} - \tfrac{1}{2}R^2)\pi R^2$$

$$Q_d = v_o \pi R^2; \quad v_o = v_{max} - \tfrac{1}{2}R^2$$

Figures A4.1.1-A4.1.5 Parabolic velocity profile with non-zero slip velocity

Appendix 4.2

Calculation of the geometrical efficiency of the gamma ray detection system

The tracer particle is moving in a cylinder with external radius R. A right-angled lead collimator is placed tangentially to the cylinder. Behind the collimator the detector with photomultiplier tube is located.

The coordinate system is chosen such that the cylinder axis is the z-axis. In the horizontal plane the other cylinder coordinates, r and ϕ, are defined. The plane z=0 is symmetrical with respect to the collimator slit (see Figure A4.2.1). From Figure A4.2.2 it can be seen that there are three distinct regions I, II and III. A photon emitted in region I will never reach the detector. Ω is defined as the solid angle by which the detector is seen by the photon. In region I Ω equals zero. The geometrical efficiency ε_{geo}, defined by:

$$\varepsilon_{geo} = \Omega/4\pi$$

equals zero.

Region I is determined by the value of $z(\alpha)$ and $z(\alpha')$ where α and α' are on the boundaries of region I/II (see Figure A4.2.2). The distance perpendicular to the collimator from a point A, situated on the boundary of region I/II is: $y = R - r\cos\phi$ (see Figure A4.2.2).

From Figure A4.2.2 it can be seen that holds:

$$\frac{x}{y} = \frac{z(\alpha) - \frac{b}{2}}{R - r\cos\phi} = \frac{b}{d}$$

from which follows:

$$z(\alpha) = \frac{b}{d}(R - r\cos\phi) + \frac{b}{2}$$

Similarly for α':

$$\frac{-z(\alpha') - \frac{b}{2}}{R - r\cos\phi} = \frac{b}{d}$$

With the result for $z(\alpha')$:

$$|z(\alpha')| = \frac{b}{d}(R - r\cos\phi) + \frac{b}{2}$$

Hence, region I is determined by:

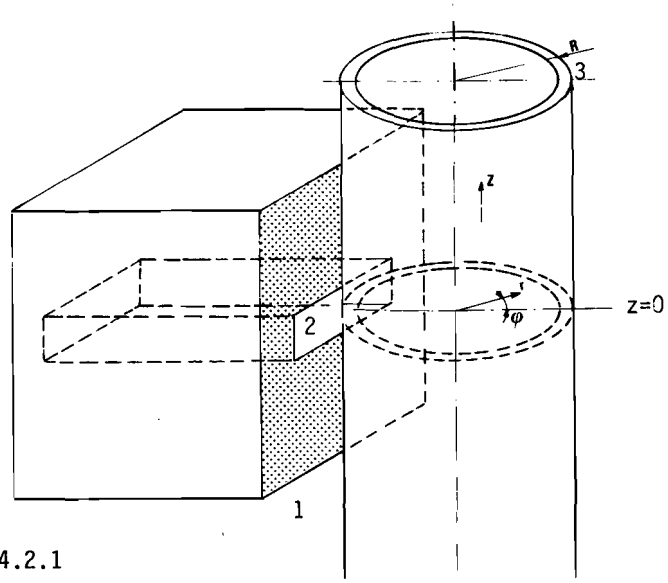

Figure A4.2.1
The standpipe and the lead collimator with collimator slit. Indicated is the cylinder coordinate system (r, Φ, z).
1. lead collimator; 2. collimator slit; 3. standpipe

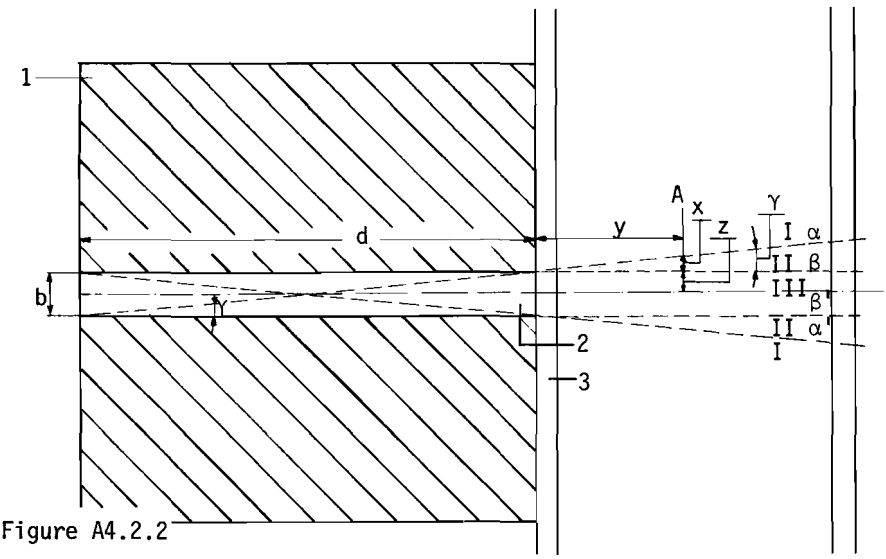

Figure A4.2.2
Vertical cross section of Figure A4.2.1, indicating the regions I, II and III with the boundaries α(α') and β(β') respectively. A is a point on the boundary of regions I and II. Indicated are the distances x and y and the angle γ.
1 lead collimator; 2 collimator slit (dimensions b, d mm); 3 standpipe

$$|z| \geq \frac{b}{d}(R - r\cos\phi) + \frac{b}{2} \qquad (1)$$

In region III the detector is seen completely by the tracer particle. The equation for region III reads

$$|z| \leq \frac{b}{2} \qquad (2)$$

as can be seen from Figure A4.2.2.

Let Q be the position of the tracer particle, somewhere in region III ($r<R$, $|z|<\frac{b}{2}$, $0\leq\phi\leq 2\pi$). From Q the detector is seen as a rectangular region. Determination of Ω involves projection of this rectangle on a spherical surface around Q. The middle of the rectangle is called M. Because it is rather complicated to determine the surface area of this curved surface the calculation is approximated by projection on the tangent plane in M (see Figure A4.2.3). Because Ω is small the error made in this way is small too: about 1%. The point with r=0 and z=0 is called O, $\overrightarrow{OM}$ is perpendicular to the front plane of the detector. The surface area of the projection is called A (see Figure A4.2.3). The solid angle Ω is approximated by:

$$\Omega = \frac{A}{\overline{QM}^2}$$

Calculation of $\overline{QM}^2$ (see Figure A4.2.3).

The projection of Q on the z=0 plane is called P, S is the projection of P on $\overrightarrow{OM}$.

$\overline{OM} = R + d$

$\overline{OS} = r\cos\phi$

$\overline{MS} = R + d - r\cos\phi$

$\overline{PS} = r\sin\phi$

$$\overline{PM}^2 = \overline{PS}^2 + \overline{MS}^2 = (r\sin\phi)^2 + (R + d - r\cos\phi)^2$$

$$\overline{QM}^2 = \overline{QP}^2 + \overline{MP}^2 = z^2(Q) + (R + d)^2 + r^2 - 2r\,(R + d)\cos\phi \qquad (3)$$

The projection (see Figure A4.2.3).

If $\phi \neq 0$ and $\phi \neq \pi$ then the front plane of the detector is not seen at right angles from P. The length of the rectangle has become $a\cos\theta$. The height b is unaltered by going from S towards P. Going from P towards Q b is shortened to $b\cos\delta$ (see Figure A4.2.3.). The surface area A equals $ab\cos\theta\cos\delta$.

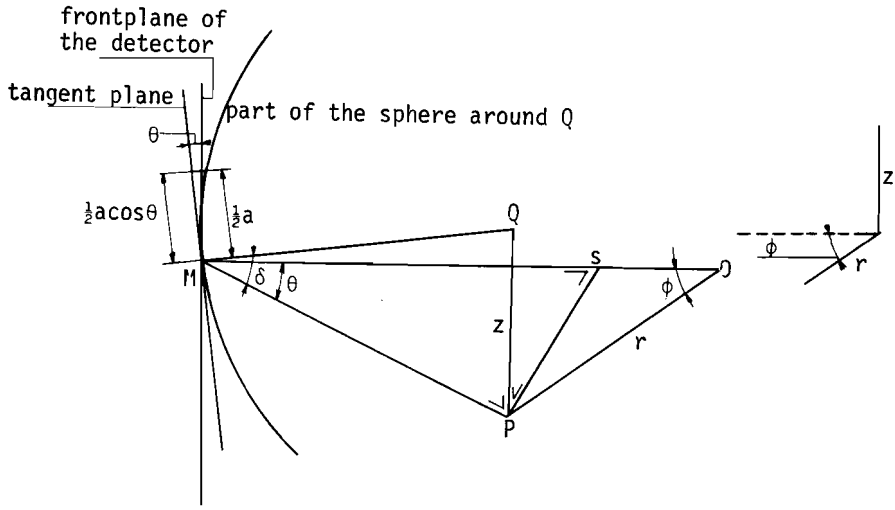

Figure A4.2.3

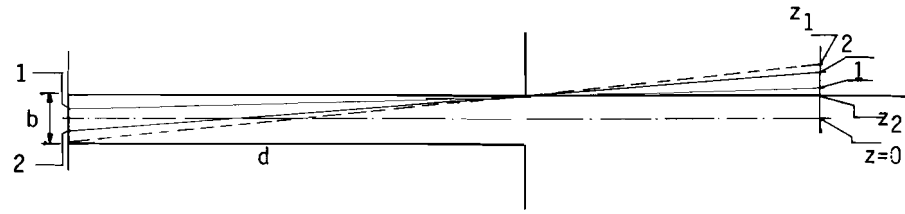

Figure A4.2.4

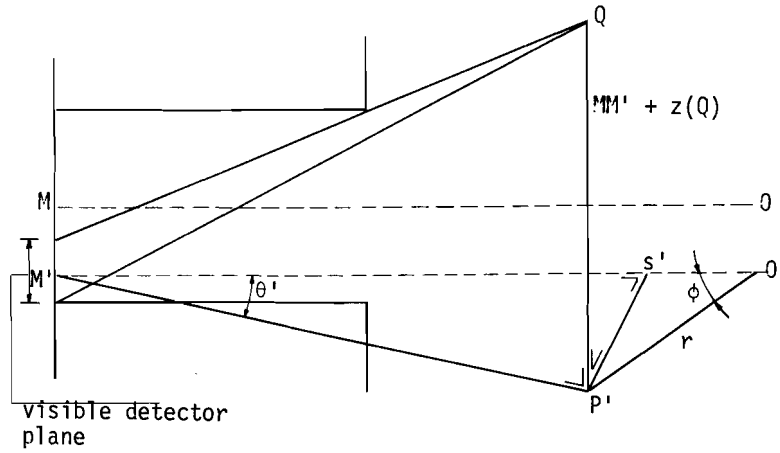

Figure A4.2.5

The angles θ and δ.
From Figure A4.2.3 it can be seen that holds:

$$\cos\theta\,\cos\delta = \frac{MS}{MP}\cdot\frac{MP}{MQ} = \frac{MS}{MQ} = \frac{R + d - r\cos\phi}{\sqrt{z^2 + (R+d)^2 + r^2 - 2r(R+r)\cos\phi}} \qquad (4)$$

Combination of formula (3) and (4) gives for the solid angle Ω in region III:

$$\Omega = \frac{A}{\overline{QM}^2} = \frac{ab\,(R + d - r\cos\phi)}{[z^2 + (R+d)^2 + r^2 - 2r\,(R+d)\,\cos\phi]^{3/2}} \qquad (5)$$

For region II Ω depends on r, ϕ and z. At the boundaries with region I and III Ω is known. For fixed r and ϕ the effect of variation of z on the visible detector plane area is calculated. The first effect is that only a part of the detector plane can be seen. The width of the visible detector plane, $a\cos\theta$, does not change, the height of the visible detector plane decreases.
The second effect is that M is no longer the middle of the visible detector plane. The distance from Q to the middle of the visible detector plane M', $\overline{M'Q}$, is larger than $\overline{MQ}$.

The first effect is, as can be seen from geometry (see Figure A4.2.4), linear in the coordinate z in between the boundaries of regions I and III. The area of the visible detector plane will be calculated by linear interpolation between these boundaries:

$$A' = f.A \qquad (6)$$

The boundaries of region II are z_1 and z_2. (For symmetry reasons it suffices to look only for z>0) $z_1 = b/d.(R - r\cos\phi) + b/2$, $z_2 = b/2$. f equals zero for $z = z_1$, and equals one for $z = z_2$. Hence f can be expressed as:

$$f = \frac{z - z_1}{z_2 - z_1} = \frac{b/2 - z}{b/d(R - r\cos\phi)} + 1 \qquad (7)$$

To account for the second effect calculation of $\overline{QM'}$ is needed
$(\overline{QM'})^2 = (\overline{P'M'})^2 + (z + \overline{MM'})^2$ (see Figure A4.2.5).
$\overline{P'M'} = \overline{PM}$
$\overline{MM'} = (1-f).\frac{b}{2}$

Hence:

$$(\overline{QM'})^2 = (R + d)^2 + r^2 - 2r(R + d)\cos\phi + (z + \frac{d}{2}\,\frac{z - \frac{b}{2}}{R - r\cos\phi})^2 \qquad (8)$$

So we get for region II:

$$\Omega = \frac{A'}{(\overline{QM'})^2} =$$

$$\frac{ab.\left[\frac{\frac{b}{2} - z}{\frac{b}{d}(R - r\cos\phi)} + 1\right] \cdot (R + d - r\cos\phi)}{\left[(R+d)^2 + r^2 - 2r\,(R+d)\,\cos\phi + (z + \frac{d}{2}\frac{z - \frac{b}{2}}{R - r\cos\phi})^2\right]^{3/2}} \tag{9}$$

Summarizing we have found:

region I.

$$\Omega(\bar{r}) = 0 : |z| > \frac{b}{d}(R - r\cos\phi) + \frac{b}{2} \tag{10}$$

region II.

$$\Omega(\bar{r}) = \frac{ab.(R + d - r\cos\phi).\left[\frac{\frac{b}{2} - z}{\frac{b}{d}(R - r\cos\phi)} + 1\right]}{\left[(R+d)^2 + r^2 - 2r\,(R+d)\cos\phi + (z + \frac{d}{2}\frac{z - \frac{b}{2}}{R - r\cos\phi})^2\right]^{3/2}} \tag{11}$$

$$\frac{b}{2} < |z| < \frac{b}{d}(R - r\cos\phi) + \frac{b}{2}$$

region III

$$\Omega(\bar{r}) = \frac{ab\,(R + d - r\cos\phi)}{\left[(R+d)^2 + r^2 - 2r\,(R+d)\cos\phi + z^2\right]^{3/2}} \tag{12}$$

$$|z| < \frac{b}{2}$$

To illustrate these results the calculated $\Omega(z)$ has been plotted in Figure A4.2.6 for some special cases:
$a = 60$, $b = 10$, $d = 100$, $R = 35$
$(r = 0)$, $(r = 30, \phi = 0)$ and $(r = 30, \phi = \pi)$.

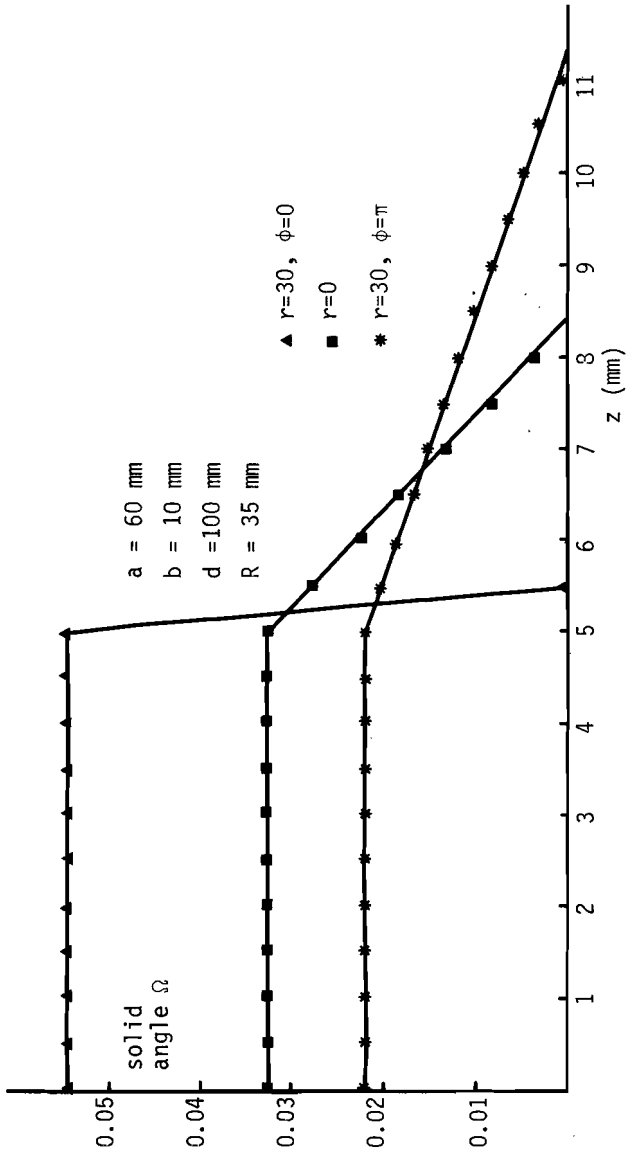

Figure A4.2.6 The solid angle Ω as function of z for (r=30, Φ=0), (r=0) and (r=30, $\Phi=\pi$)

Appendix 4.3

Calculation of the absorption of gamma rays by fresh cracking catalyst

The attenuation of the gamma rays by the catalyst is determined by the lenght of the path through the catalyst (maximum 60 mm), the bulk density of the catalyst (approximately 380 kgm^{-3}), the chemical composition of the catalyst and the energy of the photons.
The mass attenuation coefficient a can be calculated from the chemical composition. The cross section for photon absorption as function of the photon energy for several chemical components is known from the literature [2,3,4,5,6]. The chemical composition of catalyst in weight percentages is given in Table A4.3.1. The weight percentages of the elements, present in catalyst, are given in Table A4.3.2.

The mass attenuation coefficient of catalyst is given by:

$$a_{cat} = \sum_i a_i \cdot \alpha_i$$

where the summation extends over the chemical elements present in the composition, a_i is the mass attenuation coefficient of element i, while α_i is the corresponding weight percentage.

The values of a_{cat} calculated by this formula are given in Table A4.3.3, together with values for the transmission of the incident photon flux for two bulk densities: ρ_b = 380 kg m^{-3} and ρ_b = 400 kg m^{-3} respectively (see Figure A4.3.1).

Chemical composition of dry fresh catalyst	
	weight perc.
SiO_2	74.03
Al_2O_3	25.02
SO_4	0.91
Fe	0.03
Na_2O	0.01
	100.00

Table A4.3.1

Weight percentages of the elements in fresh catalyst	
O	51.81
Si	34.61
Al	13.24
S	0.30
Fe	0.03
Na	0.01
	100.00

Table A4.3.2

photon energy (keV)	$a_O \times 10$ (m^2kg^{-1})	$a_{Al} \times 10$ (m^2kg^{-1})	$a_{Si} \times 10$ (m^2kg^{-1})	$a_S \times 10$ (m^2kg^{-1})	$a_{Fe} \times 10$ (m^2kg^{-1})	$a_{Na} \times 10$ (m^2kg^{-1})	$a_{cat} \times 10$ (m^2kg^{-1})	transmission through a layer of 60 mm fresh catalyst	
								ρ_b=380 kg m^{-3}	ρ_b=400 kg m^{-3}
10	5.34	24.3	31.5	49.5	169	15.5	17.09	1.195×10^{-17}	1.538×10^{-18}
15	1.69	7.48	9.78	15.25	56.2	4.58	5.31	5.52×10^{-6}	2.92×10^{-6}
20	0.794	3.26	4.25	6.59	25.2	2.01	2.34	4.82×10^{-3}	3.64×10^{-3}
25	0.504	1.81	2.30	3.40	13.7	1.10	1.31	5.04×10^{-2}	4.31×10^{-2}
30	0.362	1.08	1.38	2.08	8.01	0.705	0.817	15.52	14.07
40	0.251	0.543	0.670	0.978	3.55	0.395	0.438	36.84	34.95
50	0.207	0.353	0.421	0.580	1.90	0.281	0.302	50.23	48.44
60	0.188	0.268	0.311	0.404	1.18	0.228	0.242	57.59	55.95
80	0.167	0.197	0.219	0.257	0.590	0.181	0.189	64.99	63.53
100	0.155	0.169	0.182	0.201	0.370	0.159	0.166	68.49	67.14
150	0.137	0.138	0.144	0.150	0.196	0.134	0.140	72.67	71.46
200	0.124	0.122	0.127	0.130	0.146	0.120	0.125	75.20	74.08
300	0.107	0.104	0.108	0.109	0.110	0.103	0.106	78.53	77.54
400	0.0956	0.0927	0.0961	0.0968	0.0939	0.0918	0.0954	80.45	79.54
500	0.0871	0.0844	0.0873	0.0879	0.0840	0.0836	0.0968	82.04	81.19
600	0.0805	0.0779	0.0805	0.0810	0.0769	0.0774	0.0802	83.29	82.49
800	0.0708	0.0683	0.0708	0.0708	0.0668	0.0678	0.0705	85.15	84.43
1000	0.0636	0.0614	0.0635	0.0637	0.0598	0.0609	0.0633	86.56	85.91

Table A4.3.3

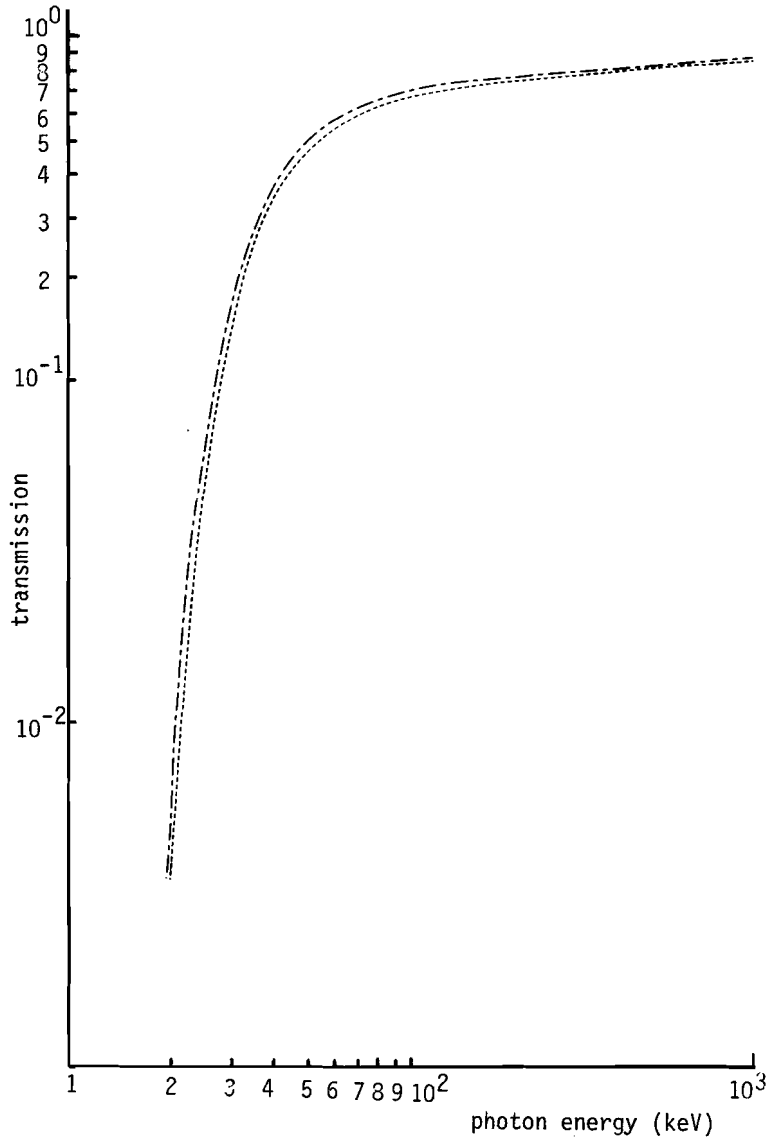

Figure A4.3.1 Transmission of gamma photons through a layer of 60 mm of catalyst

—·—·—·— ρ_{bulk} = 380 kg/m^3

····· ρ_{bulk} = 400 kg/m^3

Appendix 4.4

Calculation of the drag force excerted by the gas on the labeled particles

The slip velocity, v_s, between the gas and the labeled particles is expressed by the Ergun relation:

$$v_s = \frac{d_{\ell p}^2 \cdot \Delta\rho \cdot g}{180\mu} \frac{\varepsilon^2}{1-\varepsilon} \qquad (1)$$

where $d_{\ell p}$ is the diameter of the labeled particle
$\Delta\rho$ is the density difference between gas and labeled particles
g is the acceleration due to gravity
μ is the gas viscosity
ε is the bulk porosity

The drag force per labeled particle, F_D, is expressed by the Stokes force for one isolated labeled particle and an -yet unknown- function of the porosity, $h(\varepsilon)$.

$$F_D = F_{Stokes} \cdot h(\varepsilon) = 3\pi\mu\, v_s\, d_{\ell p}\, h(\varepsilon) \qquad (2)$$

Of course F_D can be related to the interaction force F_S between gas phase and dispersed phase per unit volume dispersed system by:

$$F_D = \frac{F_S}{1-\varepsilon} \cdot V_{\ell p} \qquad (3)$$

here $V_{\ell p}$ is the volume of the labeled particle.

F_S follows from a force balance for both phases for stationary unidirectional uniform flow:

$-\varepsilon\nabla P - \varepsilon\rho_c \underline{g} + \overline{F}_S = 0$ for the gas phase

$-(1-\varepsilon)\nabla P - (1-\varepsilon)\rho_{\ell p} \underline{g} - \overline{F}_S = 0$ for the dispersed phase

where ∇P is the pressure gradient
ρ_c is the density of the gas

From these equations follows for $\overline{F}_S$:

$$\overline{F}_S = \varepsilon\, \rho_c \underline{g} + \varepsilon\nabla P = \underline{g}\varepsilon(1-\varepsilon)(\rho_c - \rho_{\ell p})$$

and thus F_D can be expressed by:

$$F_D = g\ \varepsilon\ \Delta\rho\ \pi\ \frac{d_{\ell p}^{\,3}}{6} \tag{4}$$

From equations (2) and (4) follows for F_D:

$$F_D = \varepsilon\ \Delta\rho\ g\ \pi\ \frac{d_{\ell p}^{\,3}}{6} = 3\pi\ \mu\ v_s\ d_{\ell p}\ h(\varepsilon) \tag{5}$$

Thus v_s can be expressed as:

$$v_s = \frac{d_{\ell p}^{\,2}}{18\mu} \cdot \Delta\rho \cdot g\ \frac{\varepsilon}{h(\varepsilon)} \tag{6}$$

Using equations (1) and (5) $h(\varepsilon)$ can be expressed by:

$$h(\varepsilon) = \frac{10(1-\varepsilon)}{\varepsilon}$$

From equations (2) and (7) follows for F_D:

$$F_D = 3\pi\ \mu\ v_s\ d_{\ell p}\ \frac{10(1-\varepsilon)}{\varepsilon}$$

Appendix 4.5

Calculation of the activity of ^{198}Au and ^{199}Au after neutron bombardment of ^{197}Au.

The reaction reads:

$$^{197}Au \underset{I}{\overset{n}{\rightarrow}} {}^{198}Au \underset{II}{\overset{n}{\rightarrow}} {}^{199}Au$$

The essential constants are:

The cross section of ^{197}Au for neutron reaction: $\sigma_1 = 99$ barn

The cross section of ^{198}Au for neutron reaction: $\sigma_2 = 2.6 \times 10^4$ barn

The half life time of ^{198}Au: $T_{\frac{1}{2},1} = 2.7$ days

The half life time of ^{199}Au: $T_{\frac{1}{2},2} = 3.3$ days

The neutron flux, $\sigma \approx 10^{13}$ $cm^{-2}s^{-1}$ (for BEFA at IRI at Delft).

The differential equation for reaction I is:

$$\frac{dN_1}{dt} = \phi\sigma_1 N_o(t) - \lambda_1 N_1(t) - \phi\sigma_2 N_1(t) \qquad (1)$$

where

$$N_o(t) = N_o - N_1(t) - \int_o^t \lambda N_1(\tau)d\tau - \int_o^t \phi\sigma_2 N_1(\tau)d\tau \qquad (2)$$

here in is:

$N_o(t)$ the number of ^{197}Au nuclei per gram gold at time t.

N_o the number of ^{197}Au nuclei per gram gold before bombardment:

$N_o = \frac{6 \times 10^{23}}{M}$, where M is the atomic mass of gold.

$N_1(t)$ the number of ^{198}Au nuclei per gram gold at time t.

λ_1 the decay constant of ^{198}Au:

$\lambda_1 = \frac{\ln 2}{T_{\frac{1}{2},1}}$

λ_2 the decay constant of ^{199}Au,

$\lambda_2 = \frac{\ln 2}{T_{\frac{1}{2},2}}$

The boundary conditions are:

$$N_1 (t=0) = 0 \qquad (3)$$

$$\frac{dN_1}{dt} (t=0) = \phi\sigma_1 N_o$$

The first term at the right hand side of equation (1) indicates the increase of the number of ^{198}Au nuclei due to reaction I, the second term gives the decrease in N_1 due to radioactive decay of ^{198}Au, while the third term accounts for the activation of ^{198}Au by neutron bombardment to ^{199}Au. A similar interpretation holds for equation (2).

By differentiation of equation (1) to t the integrals in equation (1) disappear:

$$\frac{d^2N_1}{dt^2} + \frac{dN_1}{dt} \cdot (\phi\sigma_1 + \lambda_1 + \phi\sigma_2) + N_1 \phi\sigma_1 (\lambda_1 + \phi\sigma_2) = 0 \qquad (4)$$

Solution of equation (4) reads:

$$N_1 = e^{\gamma t}$$

where γ equals:

$$2\gamma_{1,2} = -(\phi\sigma_1 + \lambda_1 + \phi\sigma_2) \pm \sqrt{(\phi\sigma_1 + \lambda_1 + \phi\sigma_2)^2 - 4\phi\sigma_1 (\lambda_1 + \phi\sigma_2)}$$

The general solution is:

$$N_1 = B_1 e^{\gamma_1 t} + B_2 e^{\gamma_2 t}$$

Taking into account the boundary conditions the constants B_1 and B_2 can be calculated.

The final form of the solution is:

$$N_1(t) = \frac{\phi\sigma_1 N_o}{\sqrt{(\phi\sigma_1 + \lambda_1 + \phi\sigma_2)^2 - 4\,\phi\sigma_1(\lambda_1 + \phi\sigma_2)}} \times$$

$$\left(\exp\left(\frac{-(\phi\sigma_1 + \lambda_1 + \phi\sigma_2) + \sqrt{(\phi\sigma_1 + \lambda_1 + \phi\sigma_2)^2 - 4\phi\sigma_1(\lambda_1 + \phi\sigma_2)}}{2} \cdot t \right) \right.$$

$$\left. -\exp\left(\frac{-(\phi\sigma_1 + \lambda_1 + \phi\sigma_2) - \sqrt{(\phi\sigma_1 + \lambda_1 + \phi\sigma_2)^2 - 4\phi\sigma_1(\lambda_1 + \phi\sigma_2)}}{2} \cdot t \right) \right) \qquad (5)$$

Taking the current values for the parameters the quantitative result for the number of ^{198}Au nuclei per gram gold after t days neutron bombardment is:

$$N_1(t) = 9.43 \times 10^{17} \left[\exp(-0.864 \times 10^{-4} \times t) - \exp(-2.792 \times 10^{-1} \times t)\right] \qquad (6)$$

The activity of ^{198}Au per gram gold just after bombardment during t days equals:

$$A_1 = \frac{\lambda_1 N_1(t)}{3.7\times10^{10}} \text{ Ci/g} = 75.728(\exp(-0.864\times10^{-4}\times t) - \exp(-0.2792\times t)) \quad (7)$$

After one day bombardment the activity is: 68×10^{10} Bq/g, which means that the activity per labeled particle, which contains approximately 0.4 mg gold is about 27×10^{7} Bq (7.4 mCi).

The differential equation for reaction II reads:

$$\frac{dN_2}{dt} = \phi\sigma_2 N_1(t) - \lambda_2 N_2 \quad (8)$$

The first term of the right hand side gives the increase in the number of ^{199}Au nuclei due to neutron activation of ^{198}Au. The second term accounts for the decay of the formed ^{199}Au. The boundary condition is:

$$N_2 = 0 \quad \text{at} \quad t = 0 \quad (9)$$

The solution is:

$$N_2(t) = \frac{\phi^2\sigma_2\sigma_1 N_o}{V}\left[\frac{2\exp\left(\frac{-(\phi\sigma_1 + \lambda_1 + \phi\sigma_2) + V}{2}\cdot t\right)}{V - (\phi\sigma_1 + \lambda_1 + \phi\sigma_2 - 2\lambda_2)}\right.$$

$$+ \frac{2\exp\left(\frac{-(\phi\sigma_1 + \lambda_1 + \phi\sigma_2) - V}{2}\cdot t\right)}{V + (\phi\sigma_1 + \lambda_1 + \phi\sigma_2 - 2\lambda_2)}$$

$$\left. - \frac{4 V e^{-\lambda_2 t}}{(\phi\sigma_1 + \lambda_1 + \phi\sigma_2 - 2\lambda_2)^2 - V^2}\right] \quad (10)$$

where V is: $\sqrt{(\phi\sigma_1 + \lambda_1 + \phi\sigma_2)^2 - 4\phi\sigma_1(\lambda_1 + \phi\sigma_2)}$ (11)

Substitution of the current values for the parameters yields:

$$N_2(t) = 2.45 \times 10^{18} [0.041 \exp(-0.864 \times 10^{4} \times t)$$

$$+ 0.125 \exp(-2.792 \times 10^{-1} \times t) - 0.166 \exp(-0.210 \times t)] \quad (12)$$

which formula gives the number of ^{199}Au nuclei per gram gold after t days neutron bombardment.

The activity of ^{199}Au per gram gold just after bombardment during t days equals:

$$A_2(t) = \frac{\lambda_2 N_2(t)}{3.7 \times 10^{10}} \quad Ci/g =$$

$$1.6 \times 10^{2} \, [0.041 \exp(-0.864 \times 10^{-4} \times t) + 0.125 \exp(-0.2792 \times t) - 0.166 \exp(-0.210 \times t)] \qquad (13)$$

After one day bombardment the resulting activity of ^{199}Au of one gram gold is 0.588×10^{10} Bq (0.159 Ci).

References

1 Simha, R.
Kolloïd Zeitschrift, 76/1 (1936) 16

2 Handbook of Chemistry and Physics 58 (1977-8), E 139-140

3 Siegbahn, K.
Beta and gamma ray spectroscopy, NHPC 1955

4 Storm, E., Israel, H.I.
Nuclear Data Table 7/6, 565

5 Blatz,
Radiation hygiene handbook 1959, McGraw-Hill

6 Radiological Health Handbook, 1970

List of symbols

A	activity of labeled particle	[Bq]
A'	detectable activity of the selected energy	[Bq]
a_i	mass attenuation coefficient of element i	[m^2kg^{-1}]
B_f	branching factor	[-]
c	number concentration of tracer particles	[m^{-3}]
D	diameter of standpipe	[mm]
$\mathbb{D}$	diffusion coefficient of gas in air	[m^2s^{-1}]
d	path length of gamma radiation in the absorber	[m]
$d_{\ell p}$	diameter of labeled particle	[mm]
d_i	distance particle-to-collimator i	[mm]
d_i^+	path length of the gamma radiation in the powder towards detector i	[mm]
E_γ	energy of gamma radiation	[KeV]
$\vec{F}_a$	Archimedes force on the labeled particle	[N]
$\vec{F}_g$	gravity force on the labeled particle	[N]
$\vec{F}_D$	drag force exerted by the gas on the labeled particle	[N]
G	total mass of radio nuclide	[g]
g	acceleration due to gravity	[ms^{-2}]
$H_i(x)$	plateau height of detector i at a sideway displacement of the labeled particle from the centreline of x mm	[$msec^{-1}$]
I_o	unattenuated radiation intensity	[-]
I	attenuated radiation intensity	[-]
$I_i(j)$	sum of counts in time interval $t_{2i} - t_{2i-1}$ of detector j	[-]
N	number of atoms per gram nuclide	[g^{-1}]
N'	number of activated nuclei per gram nuclide	[g^{-1}]
N_t	total number of labeled particles in the system	[-]
N_p	number of detected gamma quants during passage	[-]
P	pressure	[Nm^{-2}]
∇P	pressure gradient	[Nm^{-3}]
P(event A)	possibility of occurrence of event A	[-]
Q_d	volume powder flow	[m^3s^{-1}]
R	radius of standpipe	[mm]

r	distance of radioactive source to the detector	[m]
T	transmission coefficient of gamma radiation	[-]
$T_{\frac{1}{2}}$	half life time of radio nuclide	[s]
T_b	time of neutron bombardment	[s]
t	passage time of a labeled particle	[msec]
t_i	intersection i of the response curve with the reference count level	[msec]
V	critical volume	[m^3]
V_p	particle volume	[mm^3]
$v(r)$	local powder velocity	[ms^{-1}]
v_{max}	maximum powder velocity	[ms^{-1}]
v_{min}	minimum powder velocity	[ms^{-1}]
v_o	mean, undisturbed powder velocity	[ms^{-1}]
v_s	slip velocity of the labeled particle relative to the gas	[ms^{-1}]
v	vertical particle velocity	[ms^{-1}]
Δv	velocity difference of the labeled particles and the undisturbed powder	[ms^{-1}]
x	slit distance	[m]
x_i	sideways displacement of the particle from the centreline of detector i	[mm]

Greek symbols

α	conversion factor	[-]
α_i	weight percentage of element i	[-]
β_i	constant	[s]
γ	constant	[mm^{-2}]
ε	external porosity of flowing powder	[-]
ε_{geo}	geometrical efficiency	[-]
ε'_{geo}	maximum geometrical efficiency of a labeled particle during passage	[-]
$\bar{\varepsilon}_{geo}$	averaged geometrical efficiency during counting	[-]
ε_{de}	detector efficiency	[-]
ε	detection efficiency	[-]
μ	dynamical gas viscosity	[poise]
ρ_b	bulk density of flowing powder	[kgm^{-3}]

$\rho_{\ell p}$	density of labeled particle	[kgm^{-3}]
ρ	density of absorber	[kgm^{-3}]
σ	cross section for neutron bombardment	[cm^2]
ϕ	neutron flux	[$cm^{-2}s^{-1}$]
θ	abundance of the nuclide	[-]
Ω	solid angle	[sterad]

CHAPTER 5

RESULTS OF THE BULK AND MICRO MEASUREMENTS. DISCUSSION AND CONCLUSIONS; SUGGESTIONS FOR FURTHER INVESTIGATIONS.

Synopsis

The results of the bulk measurements are given. The practical problems with the micro measurements are briefly mentioned. The results of the micro measurements in the glass and the perspex standpipe are summarized and discussed. The micro measurements and the bulk measurements are compared. Suggestions are made for further investigations.

5.1 The bulk measurements

A lot of measurements with cracking catalyst were carried out in the glass standpipe (see Figure 3.1). By varying the gas bypass flow and the upper butterfly valve position stationary powder flow could be obtained at different porosities and at sufficiently low velocity to enable measurement of the wall slip velocity visually. The lower butterfly valve was completely open in all these measurements to prevent that an unknown amount of the powder in the standpipe was supported by the lower butterfly valve.

The measurements in the coated perspex tube are incomplete, missing the wall slip velocity value. The coated tube was not sufficiently transparent to discern the black painted powder particles from the white bulk powder particles. The measurements in the glass tube are summarized in Table 5.1 where the following quantities are tabulated: the bulk porosity of the flowing powder (ε), the pressure drop across 1371 mm of the standpipe (ΔP_{pipe}), the increase in pressure drop across the lower fluidized bed per unit time ($\Delta P_{bed}/\Delta t$), the wall slip velocity (v_w), the wall shear stress (τ_w) calculated from ε and ΔP_{pipe}, the averaged powder velocity ($\bar{v}_d$) calculated from ε and $\Delta P_{bed}/\Delta t$ and the quantity G to be defined in the following section. Table 5.2 summarizes the results in the perspex tube (ε, ΔP_{pipe}, $\Delta P_{bed}/\Delta t$, τ_w, $\bar{v}_d$).

Comparison of the τ_w values for the glass tube and the perspex tube show a strong increase in τ_w in the rough perspex tube of about a factor of 4. This clearly demonstrates the influence of the wall roughness on the wall shear stress.

ε	$-v_w$ (cm/s)	ΔP_{pipe} (N/m^2)	$-\tau_w$ (N/m^2)	$\Delta P_{bed}/\Delta t$ (N/m^2s)	$-\bar{v}_d$ (cm/s)	-G (1/s)
0.482	6.81	4943	1.278	2.735	7.24	0.14
0.481	4.81	4962	1.173	1.90	5.02	0.07
0.479	7.565	4962	1.377	3.075	8.09	0.175
0.476	6.14	5000	1.298	2.45	6.41	0.09
0.476	4.23	5013	1.154	1.66	4.34	0.037
0.474	8.405	5001	1.501	3.43	8.94	0.178
0.470	7.555	5043	1.468	3.09	7.99	0.145
0.470	4.05	5065	1.222	1.59	4.11	0.020
0.469	4.90	5069	1.228	1.95	5.03	0.043
0.466	6.09	5089	1.393	2.44	6.26	0.057
0.464	5.885	5106	1.413	2.35	6.01	0.042
0.463	7.76	5105	1.540	3.15	8.04	0.093
0.462	7.32	5116	1.524	2.97	7.56	0.08
0.460	4.775	5148	1.389	1.91	4.85	0.025
0.460	9.65	5117	1.727	3.98	10.10	0.15
0.458	5.335	5162	1.449	2.145	5.43	0.032
0.456	3.98	5185	1.407	1.595	4.02	0.013
0.454	7.39	5184	1.631	3.02	7.58	0.063
0.452	6.17	5208	1.589	2.51	6.28	0.036
0.451	5.255	5219	1.573	2.14	5.34	0.028
0.448	6.015	5239	1.668	2.47	6.13	0.038
0.446	3.028	5273	1.513	1.23	3.04	0.004
0.444	9.50	5261	1.860	3.98	9.81	0.103
0.425	10.0	5423	2.118	4.28	10.20	0.067

ε	$-v_w$ (cm/s)	ΔP_{pipe} (N/m^2)	$-\tau_w$ (N/m^2)	$\Delta P_{bed}/\Delta t$ (N/m^2s)	$-\bar{v}_d$ (cm/s)	-G (1/s)
0.512	4.55	4687	.869	1.89	5.30	0.25
0.510	7.70	4648	1.513	3.61	10.10	0.80
0.510	2.485	4733	.581	0.97	2.71	0.075
0.510	5.92	4691	1.042	2.51	7.03	0.37
0.509	6.50	4682	1.251	2.92	8.15	0.55
0.506	5.29	4734	.998	2.23	6.19	0.30
0.505	7.42	4702	1.453	3.33	9.22	0.60
0.505	4.40	4752	.910	1.80	4.98	0.20
0.503	6.66	4737	1.288	2.90	8.01	0.45
0.501	4.39	4787	.959	1.78	4.90	0.17
0.500	8.25	4740	1.578	3.68	10.09	0.61
0.499	7.70	4760	1.459	3.38	9.25	0.52
0.497	5.51	4812	1.110	2.24	6.105	0.20
0.496	6.40	4811	1.227	2.65	7.21	0.27
0.495	2.73	4858	.821	1.05	2.85	0.04
0.492	9.10	4826	1.490	3.82	10.31	0.40
0.490	7.28	4863	1.294	3.00	8.06	0.26
0.490	4.84	4886	1.038	1.905	5.12	0.09
0.489	5.96	4887	1.140	2.39	6.41	0.15
0.486	6.82	4904	1.271	2.75	7.33	0.17
0.486	2.86	4935	.933	1.095	2.92	0.02
0.485	9.01	4894	1.491	3.72	9.90	0.30
0.484	8.34	4904	1.434	3.44	9.14	0.27
0.483	2.91	4961	.977	1.12	2.97	0.02

Table 5.1 Measuring results obtained in the glass standpipe.

ε	ΔP_{pipe} (N/m^2)	$\Delta P_{bed}/\Delta t$ ($N/m^2 s$)	τ_w (N/m^2)	$-\bar{v}_d$ (cm/s)
0.474	4425	4.35	- 7.7	11.65
0.460	4494	5.83	- 8.5	15.2
0.441	4577	7.60	- 9.6	19.15
0.425	4609	9.19	-10.9	22.5
0.419	4627	10.60	-11.4	25.7
0.412	4655	12.27	-11.8	29.4

Table 5.2
Results of transport experiments in the perspex standpipe of cracking catalyst/air.

Evaluation of the measuring results using a modified Rabinőwitz equation

Because the wall slip velocity is not equal to zero the Rabinőwitz equation cannot be used directly. It is, however, possible to incorporate the wall slip velocity in the equations as is outlined in Appendix 5.1. Using these results the quantity G (s^{-1}) which enables the determination of the rate of shear ($\dot{\gamma}_w$) can be expressed as:

$$G = \frac{\bar{v}_d - v_w}{R}$$

where $\bar{v}_d$ is the averaged bulk velocity
v_w is the wall slip velocity
and R is the radius of the standpipe.

From other experiments it is known that a certain minimal shear stress is required to induce a flowing movement in a fluidized powder (e.g. tilting bed experiments [8,9] and rotation viscosimeter experiments [1,2]). So the rheological model to be applied should account for this phenomenon of the existence of a yield shear stress (τ_0). The most simple model then is the Bingham model.
Assuming the porosity of the flowing powder is constant across the horizontal cross section of the standpipe and applying the Bingham model the quantity G can be expressed in the wall shear stress (τ_w), the yield shear stress (τ_0) and the apparent viscosity (μ). This is outlined in Appendix 5.2. The final result is:

$$G = \left[\frac{\tau_w}{4\mu} + \frac{\tau_o^4}{12\mu\ \tau_w^3} - \frac{\tau_o}{3\mu}\right]_\varepsilon \qquad (1)$$

This expression enables the determination of τ_o and μ if sufficient measuring results of (G,τ_w) combinations at constant porosity are available.

The accuracy of the derived quantities

The accuracy of the quantities τ_w, $\bar{v}_d$, ρ_b and G follows from the accuracy of the directly measured quantities ε, ΔP_{pipe}, $\Delta P_{bed}/\Delta t$ and v_w.

The absolute inaccuracy of these last quantities is determined experimentally: $\sigma(\varepsilon) = 0.002$

$\sigma(\Delta P_{pipe}) = 3.3\ N/m^2$

$\sigma(\Delta P_{bed}/\Delta t) = 0.01\ N/m^2s$

$\sigma(v_w) = 1.3$ mm/s (for $-v_w = 50$ mm/s)

The results for the derived quantities are calculated to be:

$\sigma(\tau_w) = 0.11\ N/m^2$

$\sigma(\bar{v}_d) = 0.3$ mm/s (for $\varepsilon = 0.500$; $\Delta P_{bed}/\Delta t = 2.00\ N/m^2s$)

$\sigma(\rho_b) = 4.4\ kg/m^3$ ($\rho_p = 727\ kg/m^3$)

$\sigma(G) = 0.044\ s^{-1}$ (for $\Delta P_{bed}/\Delta t = 2.00\ N/m^2s$; $\varepsilon = 0.500$, $-v_w = 50$ mm/s)

Calculation of τ_o and μ using the Bingham model

Because very few combinations of G and τ_w at the same porosity are available and because at least two combinations are required to obtain τ_o and μ using equation (1) the measuring results are devided in small ε-intervals. The inaccuracy in G, τ_w and ε renders this procedure acceptable. The ε-intervals were chosen such that they contain five ε-values.

Rewriting equation (1) to

$$G\,\tau_w^3 = \frac{\tau_w^4}{4\mu} - \frac{\tau_o\tau_w^3}{3\mu} + \frac{\tau_o^4}{12\mu} = a\,\tau_w^4 + b\,\tau_w^3 + c \qquad (2)$$

an equation is obtained which enables the determination of a, b and c by deriving the best regression curve by means of the least squares fit method. The result of the computation is given in Table 5.3.

ε interval	$\bar{\varepsilon}$	μ (Ns/m^2)	$-\tau_o$ (N/m^2)
0.510-.505	.5070	.390	.394
.509-.503	.5056	.381	.401
.506-.501	.5040	.375	.417
.505-.500	.5028	.332	.494
.505-.499	.5010	.370	.495
.503-.497	.5000	.335	.477
.501-.496	.4986	.300	.560
.482-.476	.4788	.456	.802
.481-.474	.4772	.649	.763
.479-.470	.4750	.705	.757
.476-.470	.4732	.564	.837
.476-.469	.4718	.513	.863
.474-.466	.4698	.416	.919
.462-.456	.4592	.625	1.012
.460-.454	.4576	.669	1.025
.460-.452	.4560	.591	1.064
.458-.451	.4542	1.522	.989
.456-.448	.4522	1.858	.981

linear regression of μ: $\mu = 6.8469 + (-13.0208) \times \varepsilon$ Ns/m^2
corr.coef. -0.7317

of τ_o: $-\tau_o = 6.1358 + (-11.2128) \times \varepsilon$ N/m^2
corr.coef. -0.9821

Table 5.3
Fragments of the results of the computation of μ and τ_o from the experimental results by using equation (2).

The averaged value ($\bar{\varepsilon}$) is the arithmetic averaged value of the ε values in the ε interval.

$-\tau_o$ takes values inbetween 0.37 and 1.11 N/m^2 while μ lies inbetween 0.29 and 3.26 Ns/m^2.

The thus obtained τ_o and μ values are correlated with the averaged ε value by simple linear regression with the result:

$$-\tau_o = 6.1358 - 11.2128 \times \bar{\varepsilon}\ N/m^2 \quad \text{correlation coefficient: } -0.9821 \qquad (3)$$
$$\mu = 6.8469 - 13.0208 \times \bar{\varepsilon}\ Ns/m^2 \quad : -0.7317$$
$$\text{for } 0.4428 \leq \varepsilon \leq 0.5102$$

From the expression for $\tau_o(\varepsilon)$ and $\mu(\varepsilon)$ for each ε value $G(\tau_w)$ can be calculated ($G_{cal}(\tau_w)$).

The quality of the fit is indicated by the value of $\overline{|G_{EXP} - G_{CAL}|}$ where G_{EXP} is the experimentally obtained G value. For the 48 experimental measuring results G_{CAL} was derived with the expression (3) for $\tau_o(\varepsilon)$ and $\mu(\varepsilon)$. The averaged value for $|G_{EXP} - G_{CAL}|$ was 0.0530 with a standard deviation of 0.07.

The regression is at best if the averaged value of $|G_{EXP} - G_{CAL}|$ is minimal and the calculated standard deviation in $|G_{EXP} - G_{CAL}|$ is less than or equal to the standard deviation in $|G_{EXP} - G_{CAL}|$ to be expected based on the inaccuracies in the quantities G_{EXP}, τ_w and ε. The last quantity can be calculated to be: 0.06.

Using these criterions a new approximation of τ_o and μ as function of ε can be obtained by iteration. The constants A, B, C and D in the expressions

$$-\tau_o = A - B\varepsilon$$
$$\mu = C - D\varepsilon$$

are approximated until the criterions:

i) averaged ($|G_{EXP} - G_{CAL}|$) is minimal.

ii) standard deviation in $|G_{EXP} - G_{CAL}|$ is less than 0.06

are fulfilled.

Starting from some set of starting values for A, B, C and D first the approximation of A and B is sought at constant C and D, result: A' and B'. The next step is a better approximation for C and D at constant A' and B' values, etc.

As starting values the results of equation (3) are used. As illustration a part of the output is given in Table 5.4.

A	B	C	D	$\overline{\lvert G_{CAL}-G_{EXP}\rvert}$	σ in $\overline{\lvert G_{CAL}-G_{EXP}\rvert}$	conclusions
6.1358	11.2128	6.8469	13.0208	0.0530	0.0711	
6.1000	11.2128	6.8469	13.0208	0.0699	0.0861	
6.0000	11.2128	6.8469	13.0208	0.1328	0.1231	
6.1400	11.2128	6.8469	13.0208	0.0512	0.0694	A' = 6.14
6.14	11.2100	6.8469	13.0208	0.0506	0.0688	
6.14	11.20	6.8469	13.0208	0.0486	0.0668	
6.14	11.10	6.8469	13.0208	0.0346	0.0476	
6.14	11.00	6.8469	13.0208	0.0358	0.0342	
6.14	11.05	6.8469	13.0208	0.0333	0.0396	B' = 11.05
6.14	11.05	6.85	13.0208	0.0331	0.0373	
6.14	11.05	6.86	13.0208	0.0325	0.0314	
6.14	11.05	6.90	13.0208	0.0341	0.0320	
6.14	11.05	6.87	13.0208	0.0320	0.0284	
6.14	11.05	6.88	13.0208	0.0322	0.0279	C' = 6.87
6.14	11.05	6.87	13.0200	0.0320	0.0283	

final result: A" = 6.11
B" = 11.05
C" = 6.88
D" = 13.00

Table 5.4

Some steps of the iterative optimization of the correlations:

$-\tau_o = A - B \times \varepsilon$

$\mu = C - D \times \varepsilon$

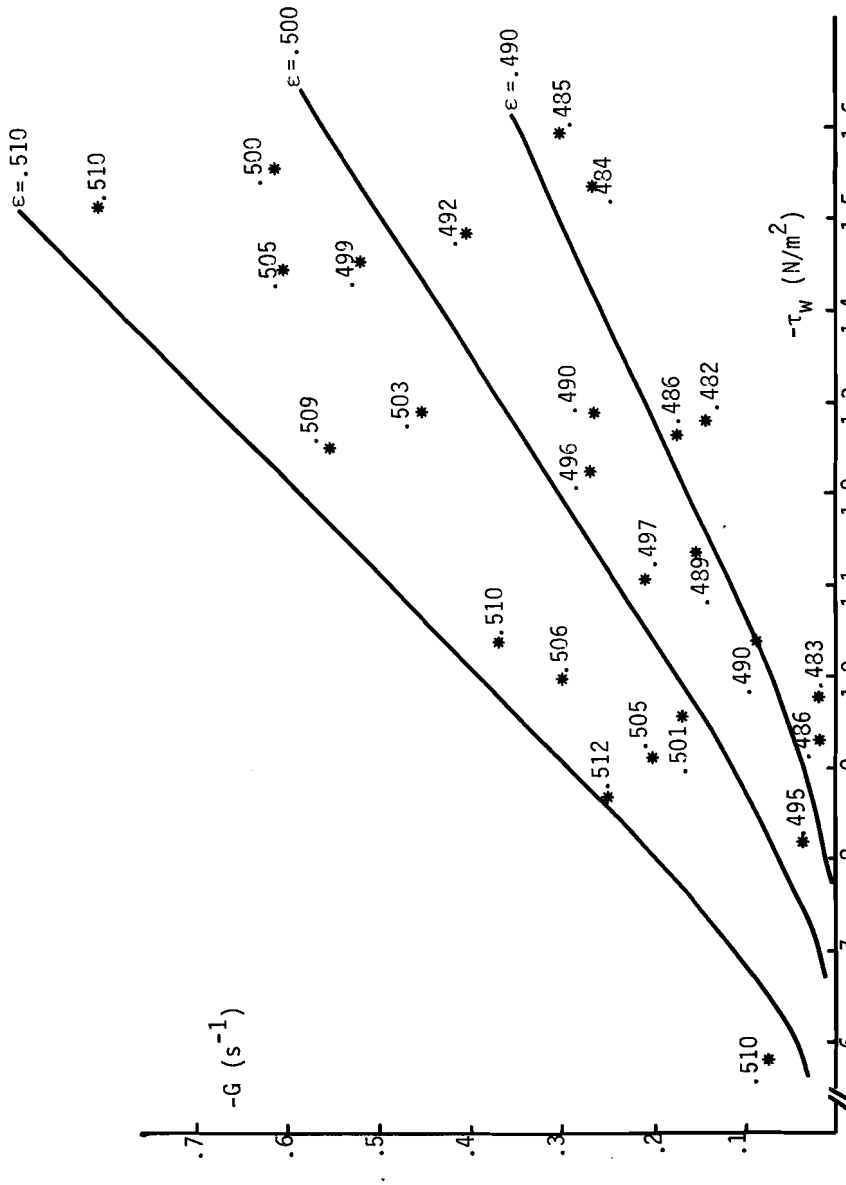

Figure 5.1
Comparison of experimentally derived $(-G, -\tau_w)_\varepsilon$ (✱) combinations and calculated $(-G, -\tau_w)_\varepsilon$ relation (—) for $-\tau_o = 6.11 - 11.05\ \varepsilon$ N/m^2 and $\mu = 6.88 - 13.00\ \varepsilon$ Ns/m^2.

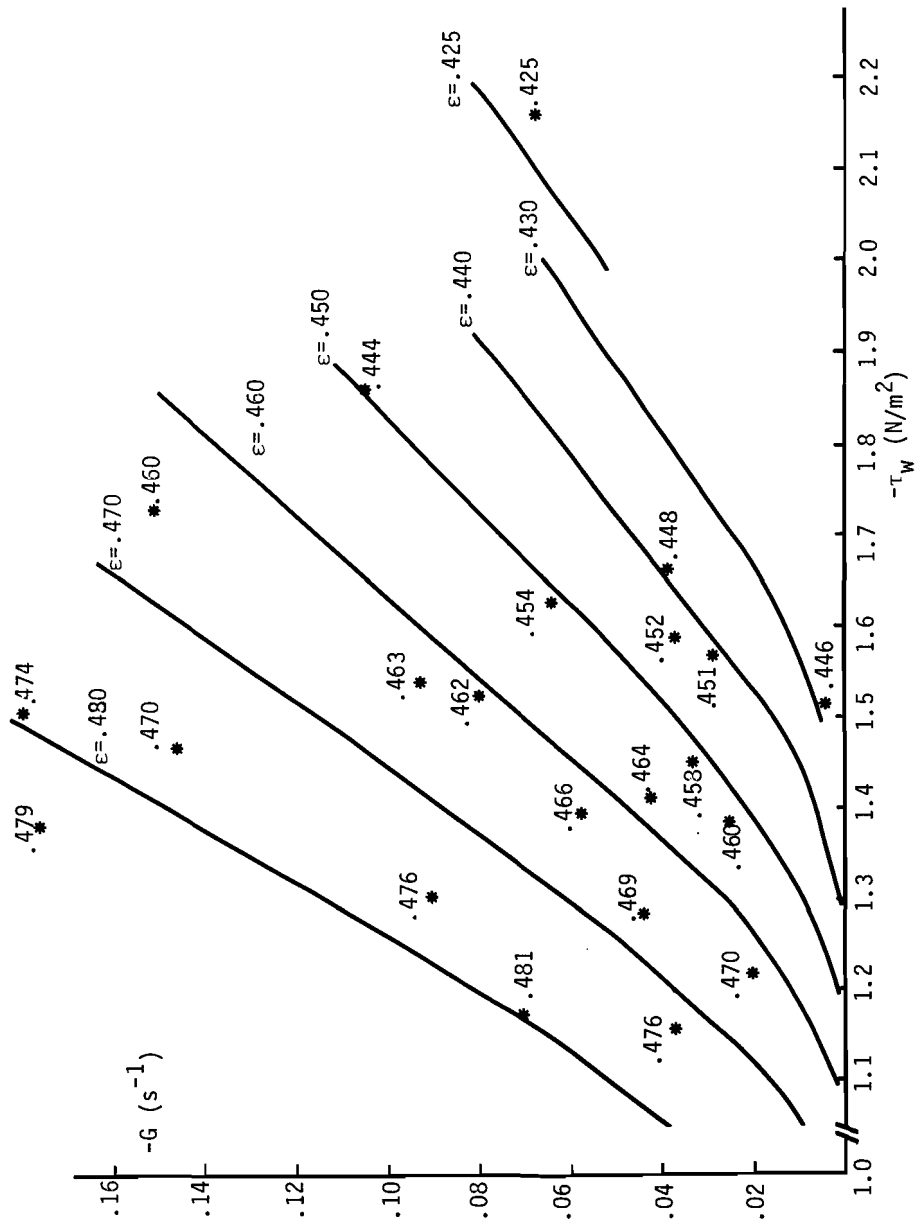

Figure 5.2

Comparison of experimentally derived $(-G, -\tau_w)_\varepsilon$ (✱) combinations and calculated $(-G, -\tau_w)_\varepsilon$ relation (—) for $-\tau_o = 6.11 - 11.05\ \varepsilon\ N/m^2$ and $\mu = 6.88 - 13.00\ \varepsilon\ Ns/m^2$.

The final result is:

$$-\tau_o = 6.11 - 11.05\varepsilon \ N/m^2$$
$$\mu = 6.88 - 13.00\varepsilon \ Ns/m^2 \qquad \text{for } 0.4428 \leq \varepsilon \leq 0.5102 \qquad (4)$$

Averaged $|G_{EXP} - G_{CAL}| = 0.029$ with standard deviation: 0.025.
In Figures 5.1 and 5.2 a comparison is made between the experimentally obtained combinations $(G_{EXP}, \tau_w)_\varepsilon$ and the calculated relation between G and τ_w for various ε values using expressions (4).
A graph of $|v_w|$ versus $|\tau_w|$ for various ε values can be seen in Figure 5.3. Also in this case the relation (between $|v_w|$ and $|\tau_w|$) is ε dependent. Just as in the foregoing the relations are obtained using five points ε-intervals and simple linear regression between $|v_w|$ and $|\tau_w|$. A part of the results of the computation is given in Table 5.5 were relations are summarized of the kind: $-v_w = \alpha + \beta * (-\tau_w)$ for $\varepsilon = \bar{\varepsilon}$. The correlation is, however, rather poor (correlation coefficient about 0.985) and for small ε values ($\varepsilon < 0.456$) the correlation fails (correlation coefficient about 0.91 or less!).

$\bar{\varepsilon}$	correlation	correlation coefficient
0.5102	$-v_w = -0.3838 + -\tau_w * 5.5406$	0.9824
.5090	$-v_w = -0.4719 + -\tau_w * 5.5830$	.9836
.5080	$-v_w = -0.9936 + -\tau_w * 6.2421$	.9845
.5056	$-v_w = -0.2441 + -\tau_w * 5.3310$	.9904
.5040	$-v_w = -0.2418 + -\tau_w * 5.3210$	.9912
.4698	$-v_w = -14.7040 + -\tau_w * 15.2813$	.9972
.4678	$-v_w = -12.9210 + -\tau_w * 13.8297$	.9928
.4664	$-v_w = -8.4435 + -\tau_w * 10.2895$	.9813
.4648	$-v_w = -9.7420 + -\tau_w * 11.2892$	.9832
.4630	$-v_w = -10.6832 + -\tau_w * 11.8829$	.9740

Table 5.5
Some fragments of the computation of the relation between $-v_w$ and $-\tau_w$ at various porosities

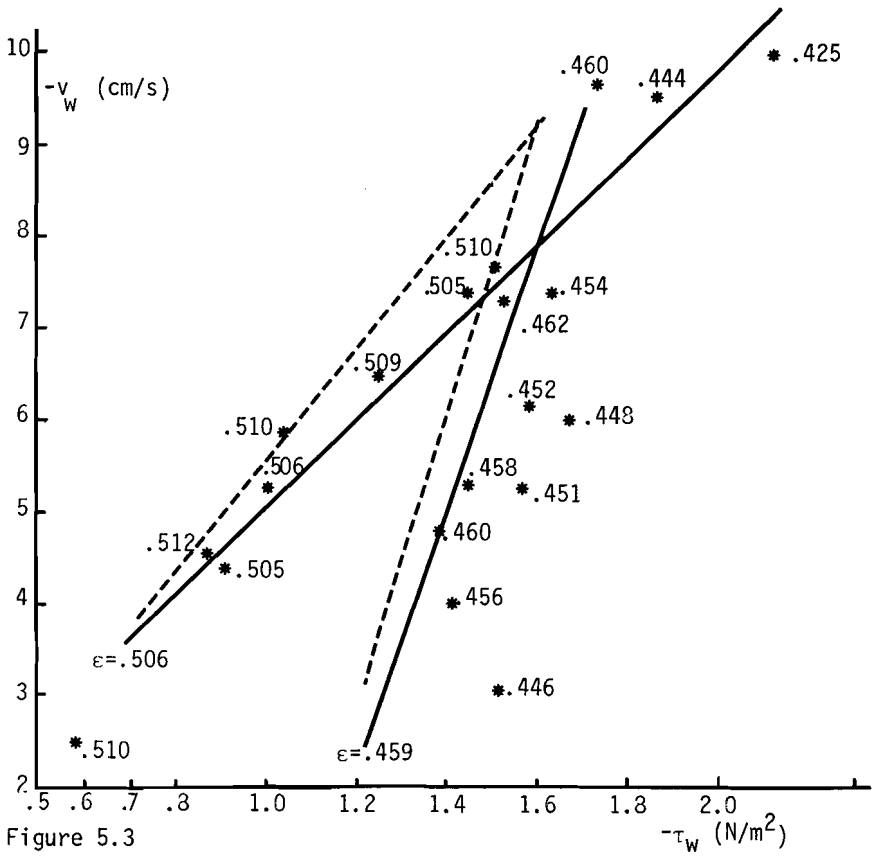

Figure 5.3

Graph of $-v_w$ and $-\tau_w$ at various porosities experimentally derived combinations (✱) and calculated relations (—) (five points ε-intervals).

The relation: $-v_w = 319.2 \times \varepsilon - 161.8 + (-198.0 \times \varepsilon + 106.1)(-\tau_w)$ gives the dotted lines (- - -).

The coefficients α and β are ε dependent and a simple linear regression is applied, giving:

$\alpha(\varepsilon) = 319.2 \times \varepsilon - 161.8 \qquad 0.456 \leq \varepsilon \leq 0.5102$

$\beta(\varepsilon) = -197\text{-}96 \times \varepsilon + 106.14 \qquad 0.456 \leq \varepsilon \leq 0.5102$

So the general expression for $v_w(\tau_w, \varepsilon)$ reads:

$$-v_w = (319.2 \times \varepsilon + 161.8) + (-198.0 \times \varepsilon + 106.1)(-\tau_w)$$

All the regression lines form a bundle of lines with centre ($-v_w = 9.25$ cm/s, $-\tau_w = 1.61$ N/m^2) so the general expression can be rewritten as:

$-v_w - 9.25 = (\tau_w + 1.61)(198.0\varepsilon - 106.14) \quad 0.456 \leq \varepsilon \leq 0.5102$

These correlations are very poor and the relations only give a very rough indication of the α and β values for a certain ε value. The relation $v_w(\tau_w,\varepsilon)$ is probably more complicated than indicated by the linear relations given. The following qualitative trends are, however, clearly visible: $-v_w$ increases with increasing $(-\tau_w)$ values. This increase at constant porosity decreases with increasing $(-\tau_w)$ values. The increase is dependent on the porosity and decreases with increasing porosity.
The interpretation of this expression is, however, not straightforward because a value for ε is used which is an averaged value over the total pipe cross section, while the porosity at the wall will be the governing parameter. This porosity at the wall is expected to be smaller than the bulk porosity, but quantitative values lack.

5.2 Results of the micro measurements

In the beginning the micro measurements gave a lot of problems. Most of them could be solved more or less easily. A few examples will be given here. During sieving the powder in the standpipe got packed and the powderflow stopped. This could be prevented by applying an extra oscillating gasflow upwards through the powder in the standpipe. This was realized by a gas bypass line going from the lower vessel above the powder bed to the powder in the standpipe just above the sieve. The oscillating gas flow is generated by a small compressor (frequency 60 Hz). To cover the entire cross-sectional area of the standpipe it was necessary to inject the gas at two diametrically positioned points.
The most serious problem was the fact that the labeled particles would not travel up and down through the standpipe when transporting the powder, but remained in the lower vessel.

Several measures were taken:

1. Increasing the fluidizing gasflow in the vessel
2. Fluidizing during half an hour vigorously ($u_{oA} \geq 10$ mm/s) before powder transport.
3. Lowering the upward powder transport velocity.

These were not sufficient. At last the powder itself was investigated in a two dimensional bed. It turned out that the powder contained a

rather large fraction of large size particles ($d_p \geq 125$ μm), which fraction segregated into a thin layer (1-2 cm) just above the bottom plate. For an -as yet- unknown reason the tracer particles got buried in this layer. When this large size fraction was removed by sieving the problem was solved.

As illustration the passage of one labeled particle as seen by detection chain 1 at a distance of d_1 = 20.15 mm from the front of the collimator is given in Figure 5.4 as the count rate versus the channel number.

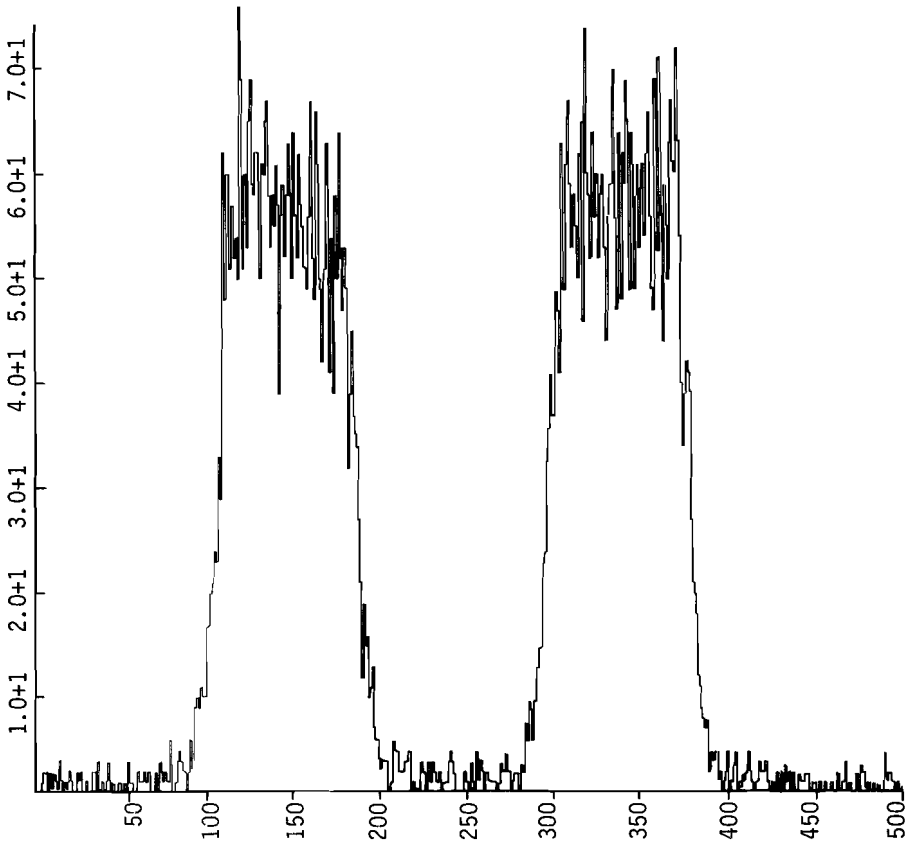

Figure 5.4
The actual output of the detection system. Indicated is the number of registered counts per millisec versus the channel number. The distance of the particle to the front of the collimator was 20.15 mm: the activity was about 1 mCi.

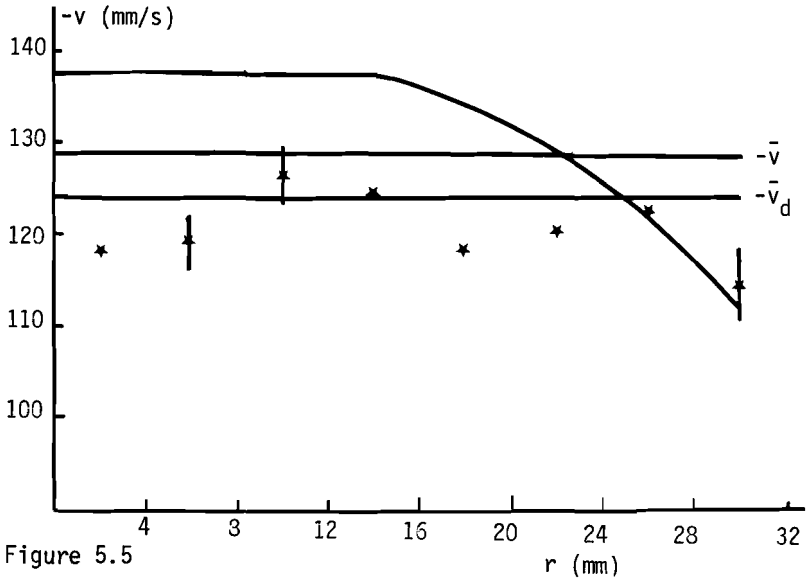

Figure 5.5

Results of the micro measurements in the glass tube. The velocity averaged per Δr-interval of 4 mm, versus r is indicated. Vertical lines indicate the standard deviation. $-v_d$ is the result of the bulk measurement. The full line is the velocity profile calculated from the bulk measurement results (Bingham model) averaged velocity $-\bar{v}$.

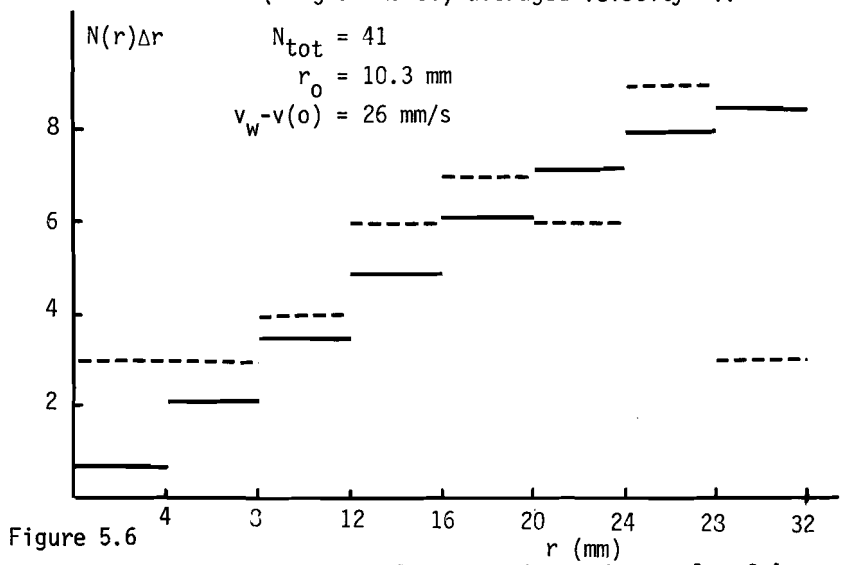

Figure 5.6

Distribution of labeled particles over the Δr-intervals of 4 mm as measured (dotted lines) and as calculated assuming a homogeneous distribution of the particles across the cross section of the pipe (full lines). The velocity is calculated by using the Bingham model.

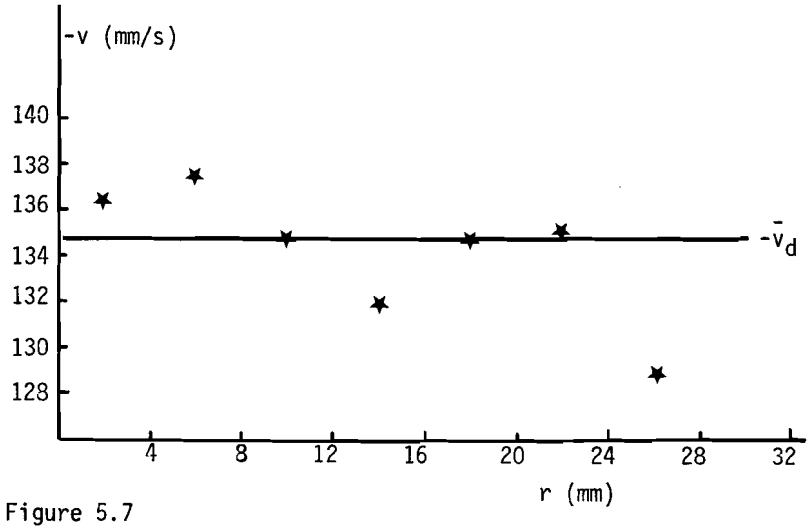

Figure 5.7

Results of the micro measurements in the perspex tube. The velocity averaged per Δr-interval of 4 mm versus r is indicated: $-\bar{v}_d$ is the result of the bulk measurement.

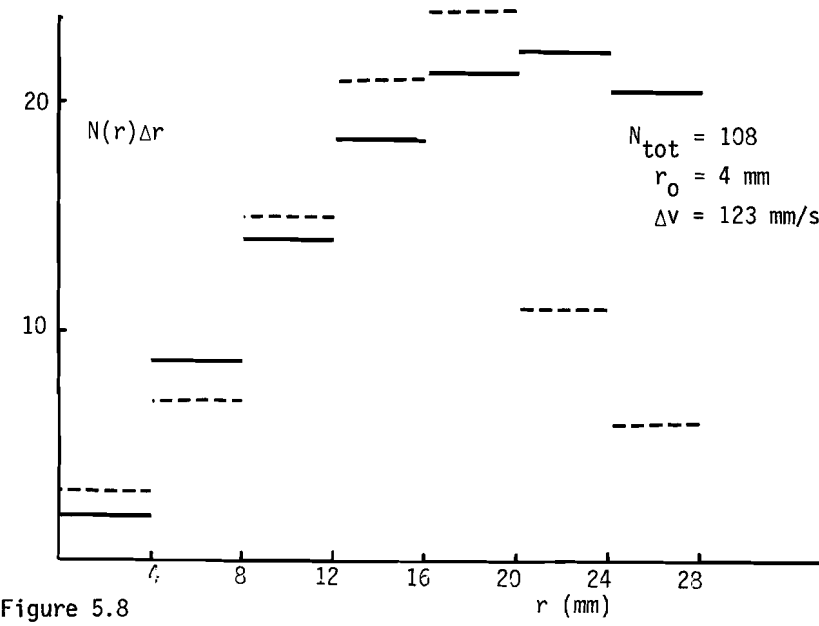

Figure 5.8

Distribution of labeled particles over the Δr-intervals of 4 mm as measured (dotted lines) and as calculated assuming a homogeneous distribution of the particles across the cross section of the pipe (full lines). The velocity is calculated by using the Bingham model.

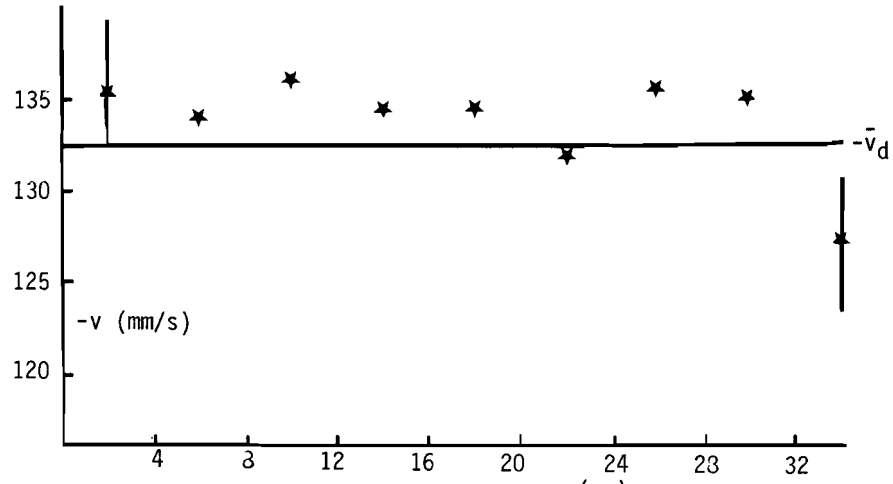

Figure 5.9

Results of the micro measurements in the perspex tube. The velocity averaged per Δr-interval of 4 mm versus r is indicated: $-v_d$ is the result of the bulk measurement.

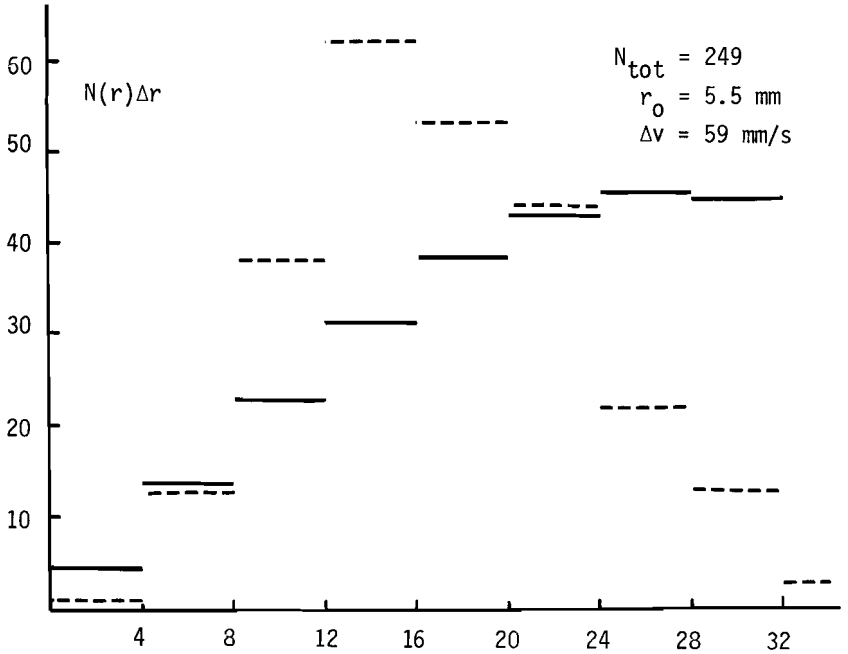

Figure 5.10

Distribution of labeled particles over the Δr-intervals of 4 mm as measured (dotted lines) and as calculated assuming a homogeneous distribution of the particles across the cross section of the pipe (full lines). The velocity is calculated by using the Bingham model.

The results of the micro measurements in the glass standpipe are given in Figures 5.5 and 5.6, while Figures 5.7, 5.8, 5.9 and 5.10 give the results for the coated perspex standpipe. The Figures 5.5, 5.7 and 5.9 give the velocity of the labeled particles as function of their radial position while in Figures 5.6, 5.8 and 5.10 the number of detected labeled particles is plotted versus the radial position. The measurements are averaged over Δr intervals of width 4 mm. This rather rough Δr division is chosen in view of the size of the labeled particles itself ($d_{lp} \approx 2$ mm) and of the inaccuracy in the position determination.
This value for the inaccuracy was obtained in calibration measurements, in which a labeled particle is moved up and down at known vertical speed at a known radial position (inaccuracy less than 0.3 mm). The calibration measurements gave for the r determination of 72 passages a full width at half height of 3.25 mm independent of the r value itself. For the velocity measurement the full width at half height was 2.36 mm/s at $\bar{v}$ = 260 mm/s (i.e. 0.9%) for 144 passages.
The velocity profiles (Figures 5.5, 5.7 and 5.9) show a nearly constant velocity for particles in the central part of the tube. The particles in the Δr interval near the pipe wall show a significantly lower velocity as was to be expected on basis of the bulk measurements. The region over which the shear rate extends is small.
The micro measurements are difficult to interpret and the required accuracy is very difficult to achieve in practice. This is partly caused by the large fluctuation in measured velocities for particles in one Δr interval. As illustration the velocity distribution of the particles in the perspex tube (Figure 5.9) at $12 \leq r < 16$ mm is given in Figure 5.11. The averaged velocity in this Δr-interval is 134.7 mm/s, the full width at half height is 13.4 mm/s (i.e. 10% of the averaged value!). This can probably be ascribed to local porosity fluctuations on a scale small compared to the size of the capacitive porosity meter (7x7 cm) and large compared to the tracer particle size. This implies that these ε-fluctuations cannot be measured with the capacitive porosity meter but that they can cause local accelerations and decelerations of the tracer particles. To obtain a reliable value of the averaged velocity in a small Δr interval a lot of measurements are required. Because the number of labeled par-

ticles in the system is limited this implies a lot of experiments at the same conditions, which also asks for a high reproducibility of the experiment and a lot of patience of the experimentalist.
The accuracy of the position determination has to be increased. It should be kept in mind, however, that the accuracy of the position determination is limited by the size of the tracer particles. The relatively large size of the tracer particles causes also a deviation of the indicated velocity profile with the actual undisturbed velocity profile. As indicated already in section 4.3 and Figure 4.13 the curvature of the velocity profile accounts for a lag in velocity of the labeled, large size particles in the order of magnitude of 0.08%. The large size of the particles causes also a migration of the particles. From literature [3,4,5,6] it is known that large size particles moving in a liquid flow rotate due to velocity gradients, which leads to a migration. For neutrally buoyant particles in a newtonian viscous fluid in a vertical circular pipe this so-called Segrē-Silberberg effect causes the particles to concentrate in a small annular zone with diameter equal to two-third of the pipe diameter. The migration of the labeled particles is demonstrated by the measured position distributions sketched in Figures 5.6, 5.8 and 5.10. The full line indicates the expected position distribution if no migration occurs, assuming the tracer particles are distributed homogeneously across the cross section of the pipe:

$$N(r)\,\Delta r = \alpha . 2\pi r \Delta r . |v(r)|$$

$N(r)\,\Delta r$ is the number of tracer particles passing at a radial distance between $r+\frac{1}{2}\Delta r$ and $r+\frac{1}{2}\Delta r$.
α accounts for the particle concentration and the total measuring time.
The migration causes that the number of particles in the regions near the pipewall is relatively small and renders the determination of the velocity in these regions additionally difficult. As outlined already the wall slip velocity is an important parameter.

These drawbacks of the micro measurements are fundamental and cannot be removed by improvements in the constructions. The drawbacks mentioned can partly be overcome only if it would be possible to use smaller tracer particles. In view of the arguments leading to our

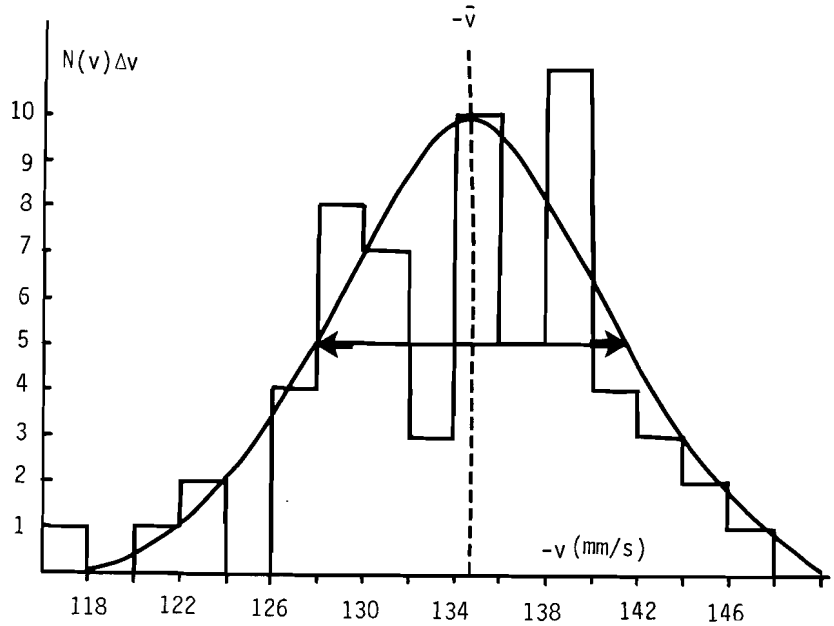

Figure 5.11

Distribution of the measured velocities of the labeled particles having radial distances between 12 and 16 mm (measurements of Figure 5.9 and 5.10). Velocity interval is 2 mm/s, averaged velocity in this Δr-interval was 134.7 mm/s.

choice for the labeled tracer particles we doubt the possibility to succeed in using smaller tracer particles.
The occurrence of the porosity fluctuations causing a large tracer particle velocity distribution cannot be solved, but is inherent to the system.

5.3 Comparison of the bulk and micro measurements

When we compare the results of the two measuring methods we see that the results are not contradictory:
both methods give a decreasing particle velocity near the standpipe wall. Also the order of magnitude of the averaged labeled tracer particle velocity and of the averaged bulk powder velocity ($\bar{v}_d$) agree. However, the quantitative values for the velocity in each

Δr interval in the shear region differ: the bulk measurements predict a much steeper velocity gradient than has been measured with the labeled tracer particles. This is even more pronounced in the perspex tube. In the evaluation of the micro measurements in the perspex tube use was made of the relations for $\tau_0(\varepsilon)$ and $\mu(\varepsilon)$, which were obtained in the glass tube. But we think this is justified because τ_0 and μ are characteristics of the flowing medium, independent of the system in which is measured.

A possible explanation for the above mentioned discrepancy between the calculated and the directly measured velocity profile might be a r dependence of the porosity (see Appendix 5.3). Therefore it would be very interesting to measure the local porosity. As outlined already this is very difficult because no disturbing measuring devices are to be put in the system.

A suggestion might be to use labeled tracer particles emitting two gamma rays: one high energetic and one low energetic. The high energetic rays should be such that the transmission through the powder is almost complete (transmission factor $\gtrsim 1$). These rays can be used to determine the position of the labeled particle accurately. The low energetic rays enable calculation of the absorption of the rays by the powder. Because the pathway in the powder is known from the position determination and the mass attenuation coefficient can be calculated (see Appendix 4.3) the averaged bulk density can be obtained. This bulk density is averaged over the pathway. By measuring at a number of positions it should be possible to deduce the local porosity. An additional advantage of this method is the increased accuracy of the determination of the position, because the iteration for the absorption is no longer necessary. The difficulty is to produce labeled tracer particles of the optimum size and particle density containing a sufficient amount of radio nuclide(s) to determine accurately the particle position and the absorption of the low energetic gamma rays.

5.4 Suggestions

Regarding the problems with the micro measurements it seems advisable to draw the attention to the bulk measurements, although it is a deductive way in contrast to the inductive character of the micro

measurements.

Some improvements in the measurements are necessary. The determination of the wall slip velocity was very simple and straightforward but was only possible in transparent standpipes at low wall slip velocity. By using two photocells at two levels in the wall and correlating the outputs the method can be extended to higher wall slip velocities. The use of piezoelectric cristals at two levels and correlation of the signals enables impact measurements in opaque standpipe at high wall slip velocities. It would be a good thing if the accuracy of the wall shear stress measurement could be increased. Our way is rather simple but involves the substraction of two large quantities to determine the relatively small wall shear stress. But we doubt if the direct measurement of the wall shear stress by means of moveable sections is more accurate. The connections of the moveable section with the rigid sections seem problematic: the connection should be flexible, should not get blocked or become less flexible due to piling up of powder, and of course should be air thight. The connection will probably induce disturbance of the flow. The force on the moveable sections will be small and therefore difficult to determine accurately.

To investigate the rheological behaviour of flowing powders it is necessary to use several powder/gas systems. The need to investigate several kinds of powder does not require any comment. The justification for the use of several kinds of gases is given in Appendix 5.4.

5.5 Summary of the conclusions

It is possible to obtain in a vertical standpipe a stationary regular uniform, unidirectional flow of fluidized powder (no bubbles).

In our experiments the averaged bulk powder velocity can be adjusted by choosing the correct combination of butterfly valve position, gas bypass flow rate and fluidizing gas flow rates.

Two measuring methods have been evaluated, tested and compared.

The results for cracking catalyst/air were roughly consistent:

1. The shear stress at the pipe wall depends on the wall roughness.
2. A yield value of the shear stress at the wall exists, the exact value depending on the bulk porosity (order of magnitude 0.5 N/m^2).

3. There is a non-zero wall slip velocity (order of magnitude v_w = 80% of $\bar{v}_d$ in the smooth glass pipe).
4. An apparent viscosity is found. The numerical value depending on the bulk porosity (order of magnitude 0.5 Ns/m^2).
5. The velocity profile is plug-shaped, with a rather large plug radius and a small shear region near the pipe wall.

To derive a rheological model, describing the flow of fluidized powders much more experiments are necessary. The influence of the powder/gas system (gas viscosity, powder particle cohesion, powder particle size, etc.) and of the measuring system (wall roughness, diameter of the pipe, etc.) should be investigated.

References

1. Schenk G., Rietema, K., Kort verslag. Internal report Eindhoven University of Technology.
2. Schenk G., Viscosimetrie in een fluid bed, 1979, internal report Eindhoven University of Technology.
3. Jeffrey R.C., Pearson R.A., J.Fluid Mechanics 22 (1965) 721
4. Ho B.P., Leal L.G., J.Fluid Mechanics 65 (1974) 365
5. Drew D.A., J.Fluid Mechanics 88 (1978) 393
6. Rubinow S.I., Keller J.B., J.Fluid Mechanics 11 (1961) 447
7. Simha R., Kolloid Zeitschrift 76 (1936) 16
8. Rietema K., Mutsers S.M.P., Proceedings of the international symposium Fluidization and its applications. Toulouse (1973) 28
9. Mutsers, S.M.P., Rietema K., Powder Technology 18 (1977) 239

List of symbols

A	nozzle area	$[mm^2]$
A'	open nozzle area	$[mm^2]$
b	constant	$[s^{-\frac{1}{2}}mm^{-1}]$
C_D	discharge coefficient	[-]
d	nozzle diameter	[mm]
d_o	minimal nozzle diameter for flow	[mm]
$\bar{d}_p$	mean particle diameter	[μm]
d_i	distance of the labeled particle towards the front of collimator i	[mm]
E	elasticity modulus	[Poise.s]
f	frequency of slip-and-stick flow	$[s^{-1}]$
G	quantity defined by $G = (\bar{v}_d - v_w)/R$	$[s^{-1}]$
G_{EXP}	experimentally derived value for G	$[s^{-1}]$
G_{CAL}	calculated value for G	$[s^{-1}]$
g	acceleration due to gravity	$[ms^{-2}]$
k	proportionality constant relating d_o, d and $\bar{d}_p$	[-]
m	total mass of powder to be transported	[kg]
$N(r)\Delta r$	number of tracer particles passing at radial distances between $r-\frac{1}{2}\Delta r$ and $r+\frac{1}{2}\Delta r$ in time interval Δt	[-]
ΔP	pressure drop	$[Nm^{-2}]$
ΔP_{pipe}	pressure drop across 1.37 m of the standpipe	$[Nm^{-2}]$
ΔP_{bed}	pressure drop across the lower fluidized bed	$[Nm^{-2}]$
$\frac{dP}{dz}$	pressure gradient	$[Nm^{-3}]$
Q	mass flow rate	$[kgs^{-1}]$
Q_d	volume powder flow rate	$[m^3s^{-1}]$
R	internal radius of the standpipe	[m]
r	radial position	[mm]
r_o	radius of the Bingham plug	[mm]
r_m	location of the extremum in the shear stress	[mm]
S	quantity defined by $S = Q_d/\pi R^3$	$[s^{-1}]$
T	discharge time	[s]
Δt	time interval	[s]
$v(r)$	local velocity	$[ms^{-1}]$
v_w	wall slip velocity	$[ms^{-1}]$

$\bar{v}_d$	averaged bulk velocity	[ms^{-1}]
$\bar{v}$	averaged value of the velocity in a Δr interval or velocity averaged over the cross section of the standpipe	[ms^{-1}]

Greek symbols

$\dot{\gamma}$	shear rate	[s^{-1}]
$\varepsilon(r)$	local porosity	[-]
ε_o	porosity at the centre of the standpipe	[-]
ε_w	porosity at the wall of the standpipe	[-]
$\bar{\varepsilon}$	arithmetic mean value of the ε-values in the ε-interval or the averaged ε-value over the cross section of the pipe	[-]
$\Delta\varepsilon$	porosity variation over the radius of the standpipe	[-]
μ	dynamical viscosity	[Poise]
μ_a	apparent dynamical viscosity	[Poise]
ρ_b	bulk density	[kgm^{-3}]
ρ_{bo}	bulk density at minimum fluidization	[kgm^{-3}]
ρ_p	particle density	[kgm^{-3}]
$\sigma(Q)$	standard deviation of quantity Q	
$\tau(r)$	local shear stress	[Nm^{-2}]
τ_o	yield value of shear stress	[Nm^{-2}]
τ_w	shear stress at the wall	[Nm^{-2}]

Appendix 5.1

Determination of the rate of shear of the powder at the wall of the standpipe

The volumetric powder flow rate in the pipe is given by

$$Q_d = 2\pi \int_0^R (1-\varepsilon)\, r\, v(r)\, dr$$

Assuming $(\frac{\partial \varepsilon}{\partial r}) = 0$ and using the boundary condition $v(r=R) = v_w$ the result is:

$$Q_d = \pi(1-\varepsilon)\, [R^2 v_w - \int_0^R r^2 \frac{dv}{dr}\, dr]$$

The relation for the shear stress in a vertical circular tube reads:

$$\tau = -\frac{r}{2} [\frac{dP}{dz} - \rho_b\, g]$$

which implies:

$$dr = \frac{-2\, d\tau}{(\frac{dP}{dz} - \rho_b\, g)}$$

so $(\frac{dv}{dr})$ is a function of the shear stress τ: $f(\tau)$

Q_d can be expressed by:

$$Q_d = \pi(1-\varepsilon)\, [R^2 v_w - \frac{R^3}{\tau_w^3} \int_0^{\tau_w} \tau^2 f(\tau)\, d\tau] \qquad (1)$$

Defining $S = Q_d/\pi R^3$ differentiation gives (2)

$$\frac{dS}{d\tau_w} = (1-\varepsilon)\, [\frac{1}{R} \frac{dv_w}{d\tau_w} + \frac{3}{\tau_w^4} \int_0^{\tau_w} \tau^2 f(\tau)\, d\tau - \frac{1}{\tau_w} (\frac{dv}{dr})_w]$$

$$- \frac{\partial \varepsilon}{\partial \tau_w} [\frac{v_w}{R} - \frac{1}{\tau_w^3} \int_0^{\tau_w} \tau^2 f(\tau)\, d\tau] \qquad (3)$$

The integrals in equation (3) can be expressed in the quantity S (eq.(1) and eq.(2))

The definition of the rate of shear $\dot{\gamma}$ reads

$$\dot{\gamma}_w = + (\frac{dv}{dr})_w \qquad \text{(see chapter 1)} \qquad (4)$$

From equations (3) and (4) $\dot{\gamma}_w$ can be expressed as:

$$-\dot{\gamma}_w = \frac{dS}{d\tau_w} \cdot \frac{\tau_w}{r\varepsilon} - \frac{\tau_w}{R} \cdot \frac{dv_w}{d\tau_w} + \frac{3S}{1-\varepsilon} - \frac{3v_w}{R} + \frac{S\tau_w}{(1-\varepsilon)^2} \frac{d\varepsilon}{d\tau_w} \tag{5}$$

Defining G by

$$G = \frac{S}{1-\varepsilon} - \frac{v_w}{R} \tag{6}$$

$\dot{\gamma}_w$ can be expressed in G and τ_w:

$$-\dot{\gamma}_w = 3G + \tau_w \frac{dG}{d\tau_w} \tag{7}$$

Remark Using the equation for $G(S,\varepsilon,v_w,R)$; $S(Q_d,R)$ and $Q_d(\bar{v}_d,\varepsilon,R)$ G can simply be written by:

$$G = \frac{\bar{v}_d - v_w}{R}$$

Appendix 5.2

Application of the Bingham model to the powder flow in the standpipe

The volumetric powder flow rate in the pipe is:

$$Q_d = \pi R^2 \bar{v}_d (1-\varepsilon) = 2\pi (1-\varepsilon) \int_0^R v(r)\, r\, dr = \pi(1-\varepsilon) \left[v_w R^2 - \int_0^R r^2 \left(\frac{dv}{\partial r}\right) dr \right]$$

where again is assumed $(\partial\varepsilon/\partial r) = 0$. (1)

The Bingham model states:

$$\tau = \tau_o - \mu \dot{\gamma} = \tau_o - \mu\left(\frac{dv}{dr}\right) \qquad (r > r_o) \tag{2}$$

for a cylindrical vertical pipe holds:

$$\tau = -\frac{r}{2}\left(\frac{dP}{dz} - \rho_b\, g\right) \tag{3}$$

Combination of (2) and (3) gives:

$$\left(\frac{dv}{dr}\right) = \left[\tau_o + \frac{r}{2}\left(\frac{dP}{dz} - \rho_b\, g\right)\right]/\mu \qquad (r > r_o) \tag{4}$$

Using equation (4) and (1) this gives:

$$R^2 \bar{v}_d = v_w R^2 - \int_0^R \frac{r^2}{\mu} \left(\tau_o + \frac{r}{2}\left(\frac{dP}{dz} - \rho_b\, g\right)\right) dr \tag{5}$$

Because $\left(\frac{dv}{dr}\right) = 0$ for $r < r_o$ in the Bingham model the lower limit in the integral can be exchanged by r_o. From equation (3) it is easy to obtain:

$$r_o = \frac{\tau_o}{\tau_w} \cdot R \tag{6}$$

Then the final result of equation (5) reads:

$$\bar{v}_d = v_w - \frac{\tau_o R}{3\mu}\left(1 - \left(\frac{\tau_o}{\tau_w}\right)^3\right) + \frac{\tau_w R}{4\mu}\left(1 - \left(\frac{\tau_o}{\tau_w}\right)^4\right)$$

which implies:

$$G = \frac{\bar{v}_d - v_w}{R} = \frac{\tau_w}{4\mu}\left(1 - \left(\frac{\tau_o}{\tau_w}\right)^4\right) - \frac{\tau_o}{3\mu}\left(1 - \left(\frac{\tau_o}{\tau_w}\right)^3\right)$$

Appendix 5.3

Influence of a r dependence of ε on the velocity profile

Assume $\varepsilon = \varepsilon_o + \Delta\varepsilon\ r/R$, where R is the radius of the pipe.
This implies $\varepsilon(0) = \varepsilon_o$

$$\varepsilon_w = \varepsilon(R) = \varepsilon_o + \Delta\varepsilon$$

and $$\bar{\varepsilon} = \varepsilon_o + \frac{2}{3}\Delta\varepsilon$$

Calculation of the wall shear stress

The general expression for a circular, vertical pipe obtained by a force balance is:

$$\frac{1}{r}\frac{d}{dr}(\tau(r).r) = -\frac{dP}{dz} - \rho_b \cdot g$$

$$= -\frac{dP}{dz} - \rho_p\, g\, (1-\varepsilon(r))$$

The flow is in the downward vertical direction (z) and ρ_b and ρ_p indicate the bulk density and the particle density respectively.
This leads to:

$$\tau(r) = -\frac{r}{2}\frac{dP}{dz} - \rho_p\, g\, \{(1-\varepsilon_o) \cdot \frac{r}{2} - \frac{\Delta\varepsilon}{R}\ \frac{r^2}{3}\}$$

The wall shear stress is

$$\tau_w = \tau(R) = -\frac{R}{2}\{\frac{dP}{dz} + \rho_p\, g\, (1-\bar{\varepsilon})\}$$

Expressing the shear stress in the wall shear stress gives:

$$\tau(r) = \tau_w \cdot \frac{r}{R} + \frac{\rho_p\, g\, \Delta\varepsilon}{3R}(r^2 - rR)$$

$\tau(r)$ has an extremum for $r = r_m = \frac{R}{2} - \frac{3}{2}\frac{\tau_w}{\rho_p\, g\, \Delta\varepsilon}$

Because the wall shear stress has a negative value when the powder flows downwards this implies that
for $\Delta\varepsilon$ positive ($\varepsilon_w > \varepsilon_o$): $r_m > \frac{R}{2}$ and τ has a minimum
and $\Delta\varepsilon$ negative ($\varepsilon_w < \varepsilon_o$): $r_m < \frac{R}{2}$ and τ has a maximum.

For one case the measuring results will be evaluated assuming a r dependent porosity.
The set of measuring results (from the glass tube) used is

$\bar{\varepsilon} = 0.500$; $v_w = -8.25$ cm/s; $\tau_w = -1.578$ N/m^2; $\bar{v}_d = -10.09$ cm/s.
Using the derived expressions for the yield shear stress and the apparent viscosity:

$\tau_o = -6.11 + 11.05\ \bar{\varepsilon}$

$\mu = 6.88 - 13.00\ \bar{\varepsilon}$

The radius of the plug can be calculated by equating

$\tau(r_o) = \tau_o$, giving: $r_o = 2.006$ cm.

Remember, however, that these equations are not quite correct because in deriving them a constant porosity is assumed.
Choosing $\Delta\varepsilon = -0.03$ the following expression for the velocity can be derived:

$$-v(r) = 0.01667 - 0.00866 \ln(0.12 + 13.00 \times r) + 1.9903 \times r - 91.35 \times r^2 - v_w \quad \text{m/s} \qquad \text{for } R > r > r_o$$

where r is expressed in meters; $-\bar{v} = 0.103$ m/s.
Graphs of $\varepsilon(r)$, $\tau(r)$ and $v(r)$ are given in Figure A5.3.1. For comparison the computation results assuming a constant porosity, equal to $\bar{\varepsilon}$, are indicated too.

$r_o^* = 1.1$ cm

$-v^*(r) = 69.21\ r^2 + 1.54\ r - 0.01619 - v_w$ m/s for $R > r > r_o$

and $\bar{v}^* = -0.0986$ m/s

From Figure A5.3.1 it can be seen that the plug radius is increased almost a factor 2 by the assumed r dependence of ε, while the velocity difference ($|v(o) - v_w|$) is almost the same (2.46 cm/s and 2.82 cm/s). This increase in the plug radius is more consistent with the results of the micro measurements.

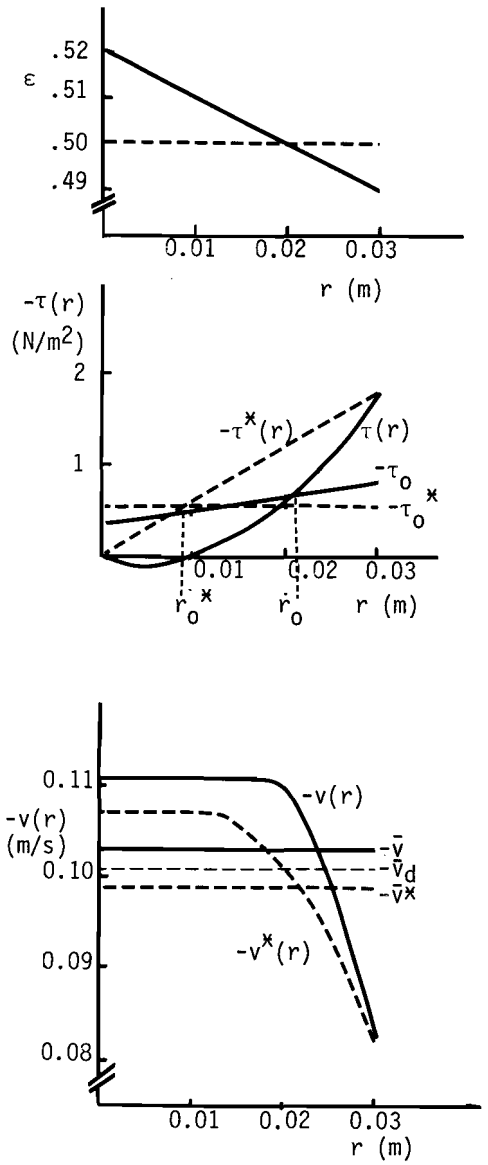

Figure A5.3.1

$\varepsilon(r)$, $\tau(r)$, $\tau_0(r)$ and $v(r)$ for two cases.

Dotted lines assume a constant porosity, parameters indicated with asterisk. Full lines assume a porosity decreasing with increasing radial distance.

Appendix 5.4

The influence of the gas on the flow behaviour of fine powders

Gas-solid interaction

As pointed out by Rietema et al. [1,4] the behaviour of a powder gas mixture is influenced by the properties of the powder as well as by the properties of the gas. In most literature on the mechanics of dispersed solids suspended in gas these mechanics are described as a result of solid characteristics and solid properties only, the effect of the gas phase and the interaction between gas and solids are not considered at all. It certainly is justified to neglect the density of the gas phase relative to the solid density and hence also the kinetic energy and the momentum concentration of the gas. Viscous transfer of momentum can be neglected compared to friction between the solids for large particles (i.e. $\bar{d}_p > 100\mu m$), for smaller particle sizes this is, however, not allowed. Another effect of gas-solid interaction is the adsorption of gas to the solids, which process is enhanced by an increase of the gas pressure and by reduction of the particle size. Gas adsorption appears to influence the structure of dense suspensions of solids.

In literature on gas-solid fluidization until recently the emphasis was put on the fluid dynamics, while of all the powder characteristics mostly only the particle size and density were taken into account. However, more and more it becomes clear that also other powder characteristics like cohesion, particle friction, etc. play an important role in fluidization behaviour.

The effect of the interaction of gas and solids is not unique for fluidization. In all handling operations of dry powders a gas is present in the interstitial pores, in the pores of the particles themselves and in the voids above the powder. In most of these operations the packing density is constantly changing so there will be a difference in velocity between gas and particles. In other words there is an interaction. This interaction will be the stronger the finer the particles are.

Effects of the gas characteristics have been observed for instance in fluidization. The stability of an expanded fluidized bed and the degree of expansion at which bubbles originate are controlled by the

dynamic equilibrium between dynamic restoring forces (originating from the elasticity of the bed structure) and the perturbing forces (caused by the upward gas flow). The upward velocity of the perturbations increases with decreasing gas viscosity and increasing gas velocity (increasing porosity). These gas flow perturbations cause perturbations of the solid particles from their rest position. Hence due to the particle inertia also the perturbing forces acting on the solids increase with decreasing gas viscosity and, therefore, will reach equilibrium with the restoring elastic forces already at a lower gas velocity when the gas viscosity is decreased. This was clearly demonstrated by the experiments and theoretical analysis of Mutsers and Rietema [2].

The observation of the effect of high pressure on the fluidization stability might be ascribed to gas adsorption to the solids. Increased gas adsorption seems to increase the cohesion of the bed structure as well as the elasticity. In this way the bed stability is increased. The bulk density of the packed bed which arises after fluidization has been stopped suddenly or after dumping from a hopper depends on the strength of the conservative force field in which the process occurs but also on the viscosity of the surrounding gas. This was clearly demonstrated by experiments in a large "human" centrifuge by Mutsers [3].

Also in the case of bulking or settling the adsorption of the gas to the solid surface plays a role especially at high pressures or in the case of very fine powders. Finally, the effect of gas-solid interaction on the grinding of fine powders should be mentioned. Experiments in a ball mill filled with different gases, under the same grinding conditions, showed that at short grinding times grinding of fresh cracking catalyst is more effect the higher the gas viscosity. The better grinding results can be explained by the better flowability of the powder. In this case the falling balls are less slowed down when they plunge in the powder pool on the bottom and hence retain a larger part of their kinetic energy for final collision with other balls or with the wall of the mill. At longer grinding times, involving smaller average particle sizes adsorption of the gas to the solids seems to decrease the grinding rate.

Similar experiments performed with quartz show a reverse effect: in neon-atmosphere the grinding is the least effective while in hydrogen

atmosphere the best grinding result is obtained. Possibly adsorption of the gas to the surface of the solid particles, which decreases the resistance to breakage of the particles is the reason for this grinding behaviour.

Adsorption measurements revealed that the adsorption of H_2 to quartz was reasonably strong, while adsorption of N_2 was much less and that of Ne was negligible. The adsorption of all the gases mentioned to cracking catalyst (measured per gram of powder) is about a factor of 10 higher than to quartz. Taking into account the specific surface areas of catalyst and quartz (about 5×10^5 m^2/kg and 1.2×10^2 m^2/kg respectively) the adsorption to catalyst is negligible compared to the adsorption to quartz. So the effect of the surrounding gas in the case of catalyst will be much more smaller than in the case of quartz.

Rheology

Fluidized powders and more or less also packed powders are able to flow. A clear rheological model of fluidized powders does not exist so far but it is clear that this rheology is characterized by at least three parameters:

i. a yield value which has to be surpassed before flow can set in. This yield value probably increases with decreasing particle size and decreasing porosity.

ii. a slip velocity along smooth and non-adhesive walls. As a consequence of both yield and slip a so-called stick-and-slip flow might occur which indeed is often observed along glass walls.

iii. an apparent viscosity, μ_a, which describes the rate of momentum exchange between neighbouring layers of particles which move at different velocities. This apparent velocity depends strongly on porosity and is probably related to the elasticity modulus E. If we assume $\mu_a = E/f$ -in which f is the frequency of the slip-and-stick flow- this would suggest that μ_a decreases if f increases. Stemerding [5] found that if from the outside a vibration, with frequencies ranging from 30 up to 100 Hz, is forced onto the powder the flow properties improve.

Concluding, these data indicate that the flowability of a powder improves markedly when the porosity increases. Because fluidized and settling powders generally have a higher porosity, when the viscosity

of the interstitial gas is higher, the apparent powder viscosity decreases if the gas viscosity increases.

Influence of the gas viscosity on the discharge time of fresh cracking catalyst in a sandglass

Experiments have been carried out in a standardized sandglass (see Figure A5.4.1) with ketjen cracking catalyst (HA-HPV) as a powder, while atmospheres of different gases (H_2, N_2, Ne) were used. The nozzle between the two hoppers of the sandglass could be exchanged, so the nozzle diameter could be varied between 1 and 12 mm. Because gas must flow upwards countercurrently with the powder also a gas bypass, which could be closed, was fitted. The conus angle of the nozzle equals the conus angle of the hoppers. The transition of the nozzle and the perspex hoppers is as smooth as possible. Care should be taken that no powder enters the bypass, because the powder would damage the o-rings sealing the throughput of the control of the rubber sheets, which separate the hoppers from the bypass. This would give rise to leakages, disturbing the measurements. To ensure reproducible measuring results the porosity at the beginning of the experiment is very important. To avoid settling of the powder, resulting in a bulk density higher than the density of a freely poured powder vibrations and bumping must be prevented. When working with different gases care has to be taken that all the gas present in the hoppers -also the interstitial gas, the gas adsorbed to the powder and the gas in the pores of the powder- must be replaced by the new gas. The gas exchange can be improved by feeding the new gas to the lower hopper, while the powder is in the upper hopper. When sucking the gas away from the upper hopper the gas has to flow through the powder thus stripping the adsorbed gas from the powder. To minimize the effect of the start and end phenomena the powder level is chosen always well above level A Figure A5.4.1.

In Figure A5.4.2 and Table A5.4.1 the measuring results are given. Indicated is the discharge time, T, i.e. the time needed to discharge 170 g fresh catalyst. Measurements are made with open as well as with closed bypass. The influence of the nozzle diameter can be described by:

$$\frac{1}{\sqrt{T}} = b(d-d_o)$$

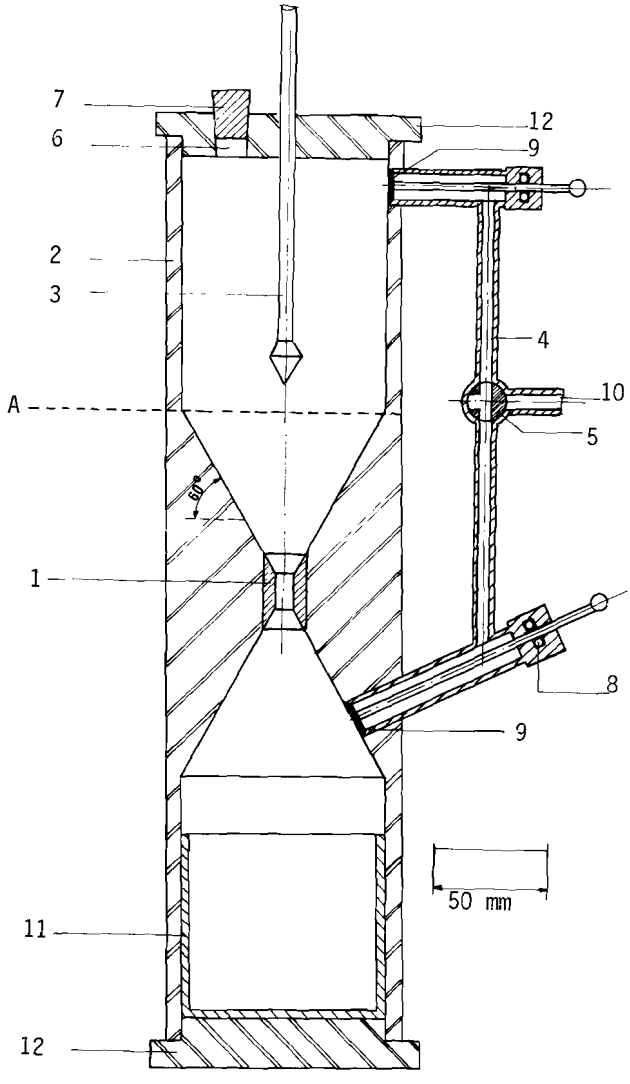

Figure A5.4.1 Sketch of the small sandglass

1.exchangeable brass nozzle
2.perspex sandglass
3.moveable stop of nozzle
4.gas bypass
5.three way valve
6. filling hole
7. rubber plug
8. o-rings
9.moveable sealing of bypass
10.gas inlet
11.perspex powder receiver glued to the cover
12. covers

nozzle diameter [mm]	discharge time [s] open bypass	discharge time [s] closed bypass	gas atmosphere
5	194.6	527	
6	112.6	272.8	
7	75.2	176.8	air
10	29.3	61.0	
12	16.7	35.8	
5	139.0	646.6	
6	81.82	332.3	
7	55.22	209.3	hydrogen
10	21.76	77.2	
12	13.37	44.9	
5	240.3	463.0	
6	139.8	197.9	
7	93.0	137.5	neon
10	34.0	55.5	
12	20.3	30.4	

Table A5.4.1 Discharge measuring results of 0.170 kg fresh cracking catalyst in a small sandglass

Table A5.4.2 gives the measuring results. d_0 is the minimal nozzle diameter for spontaneous flow, at smaller diameters flow is inhibited by bridge formation. The constant b depends on the kind of powder, the gas atmosphere and the bypass setting. d_0 varies for different gases and is influenced too by the bypass setting.
The effects of the gas viscosity are remarkable. With the bypass open the powder flows faster when the gas viscosity is lower which seems reasonable. When the bypass is closed the situation is just reversed and the powder flows faster -although always slower than with the bypass open- when the gas viscosity is higher. In this situation the gas must flow upwards through the nozzle and the powder in the upper hopper near the apex will be fluidized. As indicated in the foregoing

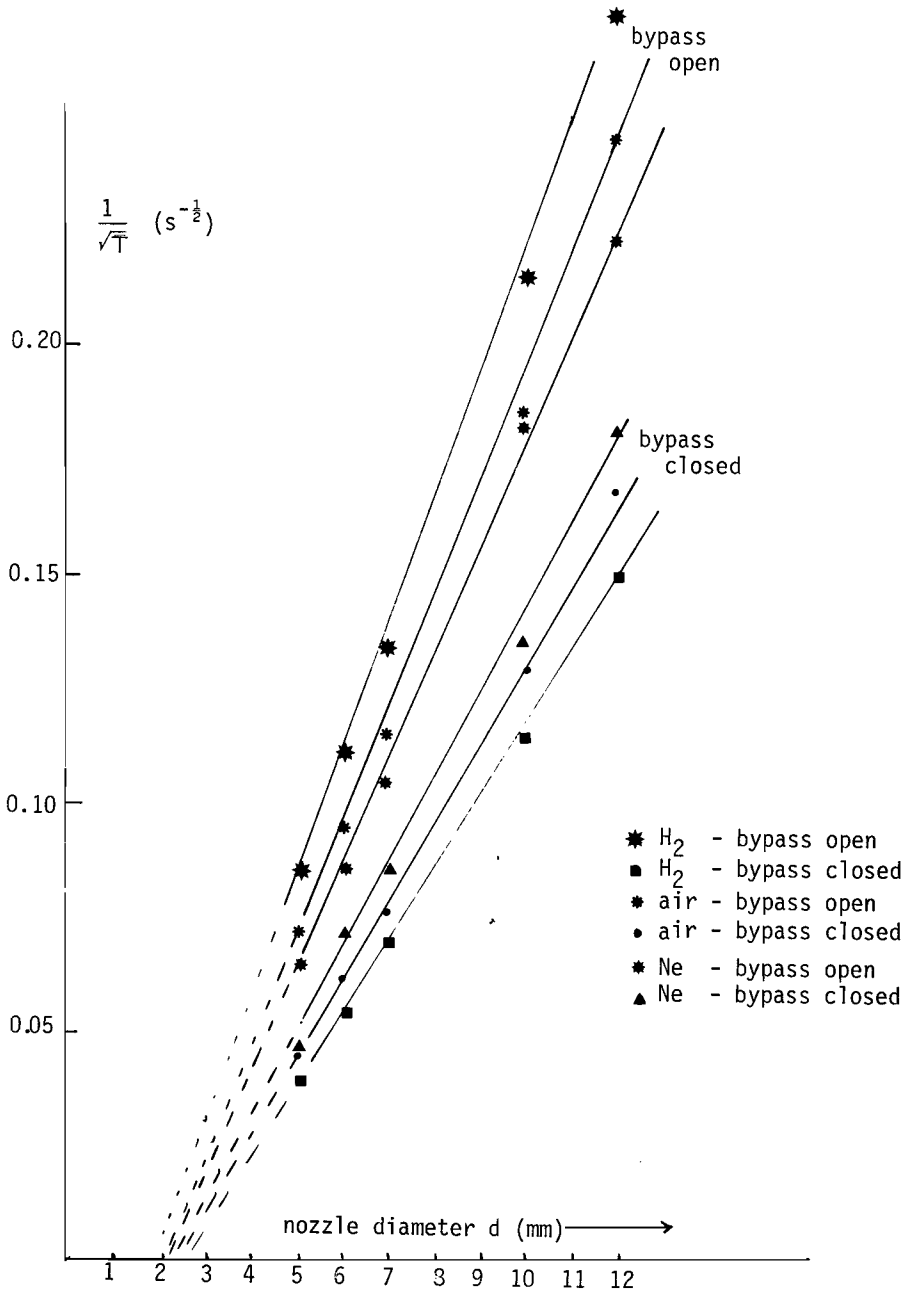

Figure A5.4.2

Results of the measurements. The time, T, needed to discharge 0.170 kg fresh catalyst as function of the nozzle diameter, d. Plotted is $T^{-\frac{1}{2}}$ versus d.

fluidization at higher gas viscosity results in higher porosity of the fluidized layers and this again improves the flowability. The formula by which the measuring results are fitted may be compared to the formulation given by Brown [6].

The mass flow rate Q was found to be proportional to g, the acceleration due to gravity. This is reasonable because g determines the driving force for flow directly. The quantity:

$$L = \frac{4Q}{\pi\rho_p\sqrt{g}}^{2/5}$$

has dimension length. ρ_p represents the particle density, plotting L

	air	H_2	Ne
bypass open	$b^2 = 0.595\times10^{-3}$ $[s^{-1}m^{-2}]$ $d_o = 2.17$ [mm]	$b^2 = 0.718\times10^{-3}$ $d_o = 1.90$	$b^2 = 0.506\times10^{-3}$ $d_o = 2.26$
bypass closed	$b^2 = 0.286\times10^{-3}$ $d_o = 2.45$	$b^2 = 0.240\times10^{-3}$ $d_o = 2.50$	$b^2 = 0.339\times10^{-3}$ $d_o = 2.37$

Table A5.4.2

The constants determining the flow equation:

$$\frac{1}{\sqrt{T}} = b(d-d_o)$$

where T: mean discharge time [s]

d: nozzle diameter [mm]

d_o: minimal nozzle diameter for flow [mm]

Squaring the equation and multiplying by m -the total mass to be transported- gives:

$$Q = \frac{m}{T} = mb^2\,(d-d_o)^2 = \frac{4}{\pi}\frac{mb^2}{\rho_b} \cdot \rho_b \cdot \frac{\pi}{4}(d-d_o)^2 \qquad (1)$$

where Q is the mass flow rate [kg/s]

$\frac{\pi}{4}(d-d_o)^2$ is the area free for flow [mm^2]

and

$\frac{4}{\pi}\frac{mb^2}{\rho_b}$ is the superficial powder velocity [mm/s]

if ρ_b is the bulk density [kg/mm^3]

versus the diameter of the orifice gives straight lines. For different particles -beads, sand and coal were used- almost parallel lines were found. None of these lines passes through the origin. Thus holds:

$$L = \alpha(d-d_o) \qquad (2)$$

Where d is the diameter of the orifice, d_o is the diameter for which Q is zero.
This formula indicates that there is an annulus of width $d_o/2$, adjacent to the edge of the aperture, through which no flow takes place. d_o does not depend on aperture size or aperture shape, but does depend on the particle size.
By putting $b^2 = \frac{\pi}{4}\frac{1}{m}\sqrt{g}\,\rho_p\,\alpha^{5/2}\sqrt{d-d_o}$ the equations (1) and (2) become identical.

De Jong [7] studied the air controlled particle flow from a flat bottomed bunker for non-cohesive fine materials through circular orifices. The effect of air injection on the discharge has been studied. The hopper has a glass filter provided with a pressure chamber as bottom. The gas pressure above the powder in the hopper is kept constant (1 bar). Measurements were carried out with sand ($\bar{d}_p$ = 140 μm), ballotini ($\bar{d}_p$ = 212 μm, 96 μm) and rabasan ($\bar{d}_p$ = 150 μm).

The effect of bed height and air input have similar effects on the solids flow rate as long as they have the same effect on the pressure drop across the orifice, which ultimately determines the flow of air through the orifice. When the solids flow rate squared is plotted versus the orifice pressure drop for various bed heights and varying air input just one line is found, other parameters being constant. Assuming the particles in the orifice behave like a fluidized bed, the flow of the air-solids mixture is treated as a liquid with a density equal to the bed density at minimum fluidization. The actual bed density, also given by de Jong, differs from the bed density at minimum fluidization roughly 10%.
Taking the velocity uniform over a part A' of the total cross section A, and zero over the remaining part of A, the results are correlated by:

$$Q^2 = C_D^{\,2}\, 2\rho_{b,o}\, A'^2\, \Delta P$$

C_D is called the discharge coefficients, $\rho_{b,o}$ the bulk density at minimum fluidization. A' is an effective orifice area defined by:

$$A' = \frac{\pi}{4} d^2 (1 - k \frac{\bar{d}_p}{d})^2$$

k is obtained from experiments of Beverloo [8]. k = 2.9 for sand and 1.4 for spherical particles.
The discharge coefficient was found to be 0.53, which value differs considerably from the value for liquids (= 0.63). De Jong tries to explain this discrepancy by assuming that in the powder flow frictional losses occur in the vena contracta in constrast with liquid flow. The dependence of Q on the nozzle diameter is the same as given in formula (1) and (2), however, the k value differs considerably, perhaps due to different particle size and increased cohesion.

Evaluation of our results in the small sandglass using the relation of de Jong and taking for ΔP the driving pressure head of the powder bed gives a C_D value of 0.29.
This discrepancy might be ascribed to the fact that the catalyst powder is more cohesive than the powder used by de Jong and the fact that no aeration has been used, which implies a packed powder bed instead of a fluidized one.

References

1 Rietema, K., Mutsers, S.M.P.
Proceedings of the international symposium on Fluidization and its Applications, Toulouse (1973) 28

2 Mutsers, S.M.P., Rietema, K.
Powder Technology 18 (1977) 239

3 Mutsers, S.M.P., Rietema, K.
Powder Technology 18 (1977) 249

4 Rietema, K. et al.
Conference Particle Technology, Amsterdam, June 3-5, 1980

5 Stemerding, S., Wes, G.W.J.
Chemisch Weekblad 75/19 (1979) 8

6 Brown, R.L., Richards, J.C.
Trans.Instn.Chem.Engrs. 38 (1960) 245

7 de Jong, J.A.H.
Powder Technology 3 (1969/1970) 279

8 Beverloo W.A. et al.
Chem.Eng.Sci. 15 (1961) 260

Summary

The investigation described in this thesis is a first step in obtaining a better comprehension of the rheological behaviour of fluidized powders.

After exploring measurements with a modified liquid rotation viscosimeter a literature study has been made concerning the flow of fluidized powders and about the "viscosity" measurements in fluidized beds. The measurements showed that three parameters play a role in characterizing the rheological behaviour: the yield shear stress, a slip velocity of the fluidized system at the wall of the measuring device and an apparent viscosity of the fluidized bed. It is not apparent from the literature that there is accounted for these three factors. From the experiments conclusions could be made for a better measuring system and a better measuring method.

An axial symmetrical powder flow in vertical direction in a cylindrical standpipe was chosen. The presence of measuring devices in the flow was avoided to prevent disturbance of the flow.

A new experimental rig, consisting of two fluidized beds above each other and connected by a vertical circular pipe was designed, constructed and tested. The system as a whole is an air-closed circuit. In preliminary experiments the way to realize the desired regular, uniform flow of the fluidized powder was determined. The powder velocity can be adjusted by choosing the correct combinations of the position of the butterfly valves at both extremities of the pipe and of the gas flows (the gas flow through the bypass line between both vessels and the fluidizing gas flows through both powder beds).

Two measuring techniques have been tested and compared. A deductive method in which the following parameters of the bulk flow were measured: averaged powder velocity, shear stress at the wall and the wall slip velocity. The averaged powder velocity follows from measurement of the pressure drop across the lower bed versus time and the determination of the bulk density of the flowing powder. For the density measurement the capacity of a flat plate condensator, placed around the standpipe, was determined. The shear stress at the wall is obtained by measuring the pressure gradient across the standpipe and the already mentioned density. The wall slip velocity is determined visually using inked powder particles.

A very simple rheological model was applied to the measuring results. The model chosen, the Bingham model, accounts for the occurrence of a yield shear stress. The parameters of the model, yield shear stress and apparent viscosity were determined using a least squares fit method and were correlated linearly with the bulk porosity of the flowing powder. From the thus obtained results the velocity profile can be calculated for every occurring porosity.
The second method is inductive and aims at the determination of the occurring velocity profile of the powder at various shear stresses at the wall of the standpipe by means of a direct measurement. For the direct determination of the velocity profile a tracer technique was developed, based on radioactive labeling of tracer particles which follow the undisturbed powder flow. The tracer particles are hand made, more or less round balls. Small polystyrene foam balls (diameter 1.0-2.0 mm) formed the kernel. They were coated with a two component resin in which the radio nuclide is very finely dispersed. The layer thickness should be such that the compositae have the correct density: equal to the bulk density of the flowing powder. The compositae were selected on their size (diameter 1.8 - 2.0 mm). The radio nuclide used ($^{197}_{79}$ Au) is activated in a neutron reactor to $^{198}_{79}$ Au. At the measurements about one hundred tracer particles are mixed with the powder, in such a way that they, distributed randomly in the standpipe, are dragged along by the powder flow. The tracer particles were thoroughly tested on their relevant properties.

The activated tracer particles are detected by means of three NaI(Tl) crystal detectors. In front of each detector is a lead collimator provided with two horizontal slits above each other. The position of the detector systems and the slit dimensions are such that each tracer particle in the pipe, passing the slits can be detected by these three detectors. From the registered signals of the three detection systems the position and the vertical velocity of the individual activated tracer particles can be derived.

The usefulness of the measuring methods has been illustrated by measurements of the system fresh cracking catalyst/air. The results of the inductive method agree reasonably with those of the deductive method.

In order to be able to formulate a rheological model much more measurements of other systems (powder particles/gas) and in other pipes (e.g. influence of the pipe diameter, wall roughness) are necessary. The investigation described gives the devices and methods to obtain the necessary measuring results.

Samenvatting

Het in dit proefschrift beschreven onderzoek is een aanzet om te komen tot een beter begrip van het stromingsgedrag van gefluïdiseerde poeders.
Na verkennende metingen met een gemodificeerde vloeistof-rotatie-viscosimeter is een literatuurstudie verricht over de stroming van gefluïdiseerde poeders en over de "viscositeits"metingen in gefluïdiseerde bedden. De metingen toonden aan dat drie parameters een rol spelen bij het rheologisch gedrag t.w.: de zwichtschuifspanning, een slipsnelheid van het gefluïdiseerde systeem aan de wand van het meetobject en een schijnbare viscositeit van het gefluïdiseerde bed. Uit de literatuur blijkt niet dat met alle drie factoren rekening is gehouden. Uit de experimenten konden conclusies getrokken worden voor een beter meetsysteem en een betere meetmethode.
Gekozen werd voor een axiaal symmetrische poederstroming in verticale richting in een cylindrische standpijp. Aanwezigheid van meetinstrumenten in de stroming werd vermeden om verstoring van de stroming te voorkomen.
Er is een nieuwe opstelling, bestaande uit twee boven elkaar geplaatste gefluïdiseerde bedden verbonden door een verticale ronde pijp ontworpen, gebouwd en getest. De opstelling als geheel heeft geen verbinding met de buitenlucht. In inleidende experimenten is bepaald hoe de gewenste regelmatige, uniforme stroming van het gefluïdiseerde poeder gerealiseerd kan worden. De poedersnelheid kan ingesteld worden door juiste keuze van de stand van de vlinderkleppen, die zich aan de beide uiteinden van de pijp bevinden, en van de gasstromen(de gasstroom in de omloopleiding tussen beide vaten en de fluïdisatiegassnelheden door beide poederbedden).
Twee meetmethoden zijn getoetst en vergeleken.
Een deductive methode, waarbij de volgende parameters van de bulkstroming werden gemeten: gemiddelde poedersnelheid, schuifspanning aan de wand en de slipsnelheid aan de wand. De gemiddelde poedersnelheid volgt uit een drukvalmeting over het onderste bed als functie van de tijd en de bepaling van de bulkdichtheid van het stromende poeder. Voor de dichtheidsmeting wordt de capaciteit bepaald van een electrische vlakke plaat condensator die om de standpijp geplaatst is. De schuifspanning aan de wand wordt verkregen uit meting van de druk-

gradient over de standpijp en de reeds vermelde dichtheidsmeting. De slipsnelheid aan de wand wordt visueel bepaald m.b.v. met inkt gekleurde poederdeeltjes. Op de verkregen meetgegevens is vervolgens een zeer eenvoudig rheologisch model toegepast. Het gekozen model, het Bingham model, houdt rekening met het optreden van een zwichtschuifspanning. De parameters van het model, zwichtschuifspanning en schijnbare viscositeit, worden bepaald m.b.v. een soort "kleinste kwadraten methode" en worden vervolgens lineair gecorreleerd met de bulkporositeit van het stromende poeder. Uit de verkregen resultaten kan het snelheidsprofiel voor iedere optredende porositeit berekend worden.
De tweede methode is inductief en beoogt de bepaling van het optredende snelheidsprofiel van het poeder bij verschillende schuifspanningen aan de wand van de standpijp middels een directe meting. Voor de directe bepaling van het snelheidsprofiel is een tracertechniek ontwikkeld, gebaseerd op radioactive merking van tracerdeeltjes die de ongestoorde poederstroming volgen. De tracerdeeltjes zijn handvaardig geproduceerde min of meer ronde bolletjes. Uitgegaan wordt van kleine piepschuim polystyreen bolletjes (diameter 1.0-2.0 mm) die gecoat worden met een twee-componenten-lijm waarin het radionuclide heel fijn gedispergeerd is. De laagdikte moet zodanig zijn dat het composietdeeltje de juiste deeltjesdichtheid heeft: gelijk aan de bulkdichtheid van het stromende poeder. De composietdeeltjes worden geselecteerd op grootte (diameter 1.8-2.0 mm). Het gebruikte radionuclide ($^{197}_{79}Au$) wordt in de neutronenreactor geactiveerd tot $^{198}_{79}Au$. Bij de metingen worden ongeveerd honderd tracerdeeltjes opgemengd met het poeder, zodat ze random door de pijp meegevoerd worden door de poederstroming. De tracerdeeltjes zijn uitvoerig getest op hun relevante eigenschappen.
De geactiveerde tracerdeeltjes worden m.b.v. 3 NaI(Tl) kristaldetectoren gedetecteerd. Vóór iedere detector bevindt zich een loodcollimator met twee horizontale, boven elkaar geplaatste spleten. De positionering van de detectorsystemen en de spleetdimensies zijn zodanig dat ieder tracerdeeltje in de pijp dat de spleten passeert door alle drie detectoren gedetecteerd wordt. Uit de geregistreerde signalen van de drie detectiesystemen kunnen de plaats en de verticale snelheid van de individuele geactiveerde tracerdeeltjes bepaald worden.

De bruikbaarheid van de meetmethoden is geïllustreerd aan de hand van metingen aan het systeem verse kraakkatalysator/lucht. De met deze

inductieve methode verkregen resultaten stemmen redelijk overeen met de resultaten van de deductieve methode. Om een rheologisch model op te kunnen stellen zijn echter nog vele metingen aan andere systemen (poederdeeltjes/gas) en in andere pijpen (bijv. invloed van de pijpdiameter, wandruwheid) nodig. Het beschreven onderzoek geeft echter de instrumenten en methoden om de benodigde meetgegevens te verkrijgen.

Dankwoord

Het in dit proefschrift beschreven onderzoek is verricht in de vakgroep Fysische Technologie. De manier waarop de leden mij, als eerste universitair fysica in de groep hebben geaccepteerd heb ik erg gewaardeerd. De gesprekken tijdens de koffiepauzes vormden steeds een aangename afwisseling met het werk en getuigden van de warme belangstelling voor elkaars leven en werk.

Mijn dank gaat uit naar de Nederlandse Organisatie voor Zuiver Wetenschappelijk Onderzoek, die het onderzoek financieel mogelijk gemaakt heeft.

Het ontwerp en de bouw van de opstelling is een gemeenschappelijke prestatie van Karel Janssen, de tekenaar/constructeur, en technici, in het bijzonder Frank Grootveld die het leeuwendeel van het werk verricht heeft -in erg moeilijke tijden bijgestaan door Toon v.d. Stappen en Toon van Schendel. De Centrale Technische Dienst heeft enkele meesterstukjes geleverd: de vlinderkleppen, het zeefsysteem en de collimatoren.

Bij het zoeken naar de geschikte radioactieve meetmethode heb ik veel steun gehad van prof.dr.ir.J.J.M. de Goeij. Tevens mijn dank voor het beschikbaar stellen van drie kristaldetectoren met photomultiplierbuis. Zijn enthousiaste belangstelling gedurende het hele onderzoek is een grote stimulans geweest.

Voor de bestraling van de tracerdeeltjes kon ik rekenen op het Interuniversitair Reactor Instituut, waar mevr.C.Zegers steeds weer zorgde dat de benodigde bolletjes op tijd bestraald werden.

De Stralings Beschermingsdienst heeft van het begin af aan een erg opbouwende rol gespeeld. De discussies met ir.Chr.J.Huyskens hebben zeker bijgedragen tot de uiteindelijke keuze van de meetmethode. Inleidende test-experimenten konden steeds verricht worden in het radiologisch laboratorium in gebouw Athene. Daarbij kon ik altijd rekenen op hulp en belangstelling van Wim Kok, Harrie Theelen en Piet Thijssen. Met electrotechnische problemen kon ik altijd terecht

bij Jacques Vermeulen.
Het vervoer van de tracerkorrels werd verzorgd door de expeditie van de T.H.Eindhoven. De S.B.D. zorgde steeds voor de benodigde vervoersdocumenten.

De uiteindelijke metingen zijn verricht in het cyclotrongebouw. De vakgroep Deeltjesfysica o.l.v. prof.dr.ir.H.L.Hagedoorn heeft bereidwillig een hoek van de bundelzaal beschikbaar gesteld om een bunker te kunnen bouwen rond de zandloper. Tevens kon ik gebruik maken van het CAMAC-interface systeem en de PDP 11/03 computor. Twee medewerkers van de groep Deeltjesfysica wil ik nog met name noemen. Austin Bruil, die in de beginfase inleidende experimenten van praktikanten heeft begeleid: Henk Arnoldussen en Johan Douwes met de spoortrein, Carol de Vries en Ivo Raaymakers met de twee spleet-collimatoren en Peter Verhallen met Ad Schuurbiers die de computorverwerking van de tweede metingen voor hun rekening genomen hebben.
Maarten Prins, die vele avonden en dagen op "het maschien" heeft zitten rammelen om het uiteindelijke meet- en verwerkingsprogramma goed draaiende te krijgen. Tevens heeft hij een zeer constructieve bijdrage geleverd bij de bouw van de bunker.

De bulkmetingen zijn verricht door Frê Didden, die als afstudeerder aan dit project gewerkt heeft. Joop Boonstra heeft op drie kritieke "momenten" zijn medewerking verleend: bij de opstart van de zandloperopstelling, bij de oplossing van het probleem van de weerbarstige tracerdeeltjes en de laatste metingen. Zijn manier van ondersteunen -er zijn als het nodig is en bereid zijn alles aan te pakken- is voor mij van onnoemelijk waarde geweest.

Verder wil ik nog noemen Ad Verkooijen, die het onderzoek steeds met belangstelling gevolgd heeft en suggesties heeft geleverd. De bereiding van het goudpoeder voor de tracerdeeltjes is zijn werk geweest.

Bij de totstandkoming van het uiteindelijke geschrift heb ik veel hulp gehad van Karel Janssen bij het tekenwerk.
Het typewerk is met veel zorg verricht door Anniek van Bemmelen. De snelheid en accuratesse van haar werk hebben bewerkstelligd dat het manuscript tijdig druk-klaar was.

Dhr.P.E.Tempelaars van de afdeling Reproductie heeft de fotografische verkleiningen van de tekeningen ongekend snel verzorgd.

Verder wil ik iedereen uit mijn naaste omgeving bedanken voor hun steun en begrip. Ik ben mij ervan bewust dat mijn aandacht en zorg voor Geert, onze komende baby en de hond wel eens tekort schoten. Bedankt dat jullie niet al te hard mopperden.

STELLINGEN

1

Het gedrag van een poeder wordt niet alleen bepaald door de eigenschappen van het vaste stof bestanddeel, maar ook door het gas dat in en rondom het poeder aanwezig is. Het is derhalve onjuist om een poeder te definiëren als bestaande uitsluitend uit vaste stof deeltjes.

dit proefschrift.

2

De afleiding die Dahneke geeft voor de attractie tussen een bolletje en een plat vlak, waarbij elastische vervorming van het bolletje optreedt houdt geen rekening met de verandering van deze vervorming indien het bolletje van het platte vlak verwijderd wordt door een uitwendige kracht.

Dahneke, B. Jl. Colloid Inf. Sci. 40/1 (1972) 1.

3

De vergelijkingen die Prudhoe en Riquarts geven voor de viscositeit van een dispersie kunnen aanzienlijke quantitatieve verschillen geven als de dichtheid van de dispersie veel afwijkt van die van de continue fase.

Prudhoe, J. British Chem. Eng. 9/6 (1964) 371.

Riquarts, H.P. Chem. Ing. Tech. 49/10 (1977) 822.

4

Uit $SiHCl_3/HCl/H_2$ mengsels kunnen met het chemical vapour deposition proces of grafiet substraten, bedekt met een 10 μm dikke tin laag, grofkorrelige polykristalijne siliciumlagen (korrelgrootte > 100 μm) verkregen worden bij een oppervlakte temperatuur van $1400^{o}k$. Met deze methode kan de kostprijs van photovoltaïsche cellen drastisch gereduceerd worden.

Graef, M.W.M., thesis, K.U.N. (1980).

5

Combinatie van meerdere meettechnieken zoals moleculaire beam maser technieken en verstrooiingstechnieken kan veel nieuwe mogelijkheden openen in het simulatie-onderzoek naar de verklaring van het in interstellaire emissies optredend verschijnsel dat de hoger gelegen atomaire energie toestanden relatief te zwaar bezet zijn (populatie inversie).

Reynders, J.M.H., thesis K.U.N. (1978).

6

In een goed ontworpen continu werkend bezinkingsbassin zullen de vertikale dichtheidsgradiënten, die als gevolg van het sedimentatieproces overal optreden verhinderen dat zich in de horizontale stroming turbulenties ontwikkelen.
Theorieën over het effect van eventueel optredende turbulenties op het rendement van de bezinking zijn dan ook irrelevant.

Dobbins, W.E., Transactions, ASCE 109 (1944) 629.

Cordoba-Molina, J.F. et. al., Jl. of the environmental engineering division, 104 (1978) 1263.

Wheatland A, Chemistry and Industry (1982) 81.

7

Zolang aan een gehuwde sollicitante bij haar sollicitatie indiscrete vragen gesteld worden over haar gezinsplanning is van een echt gelijke behandeling van beide sexen geen sprake.

8

De tijd die in verscheidene onderzoeksgroepen aan instellingen van W.O. verstrijkt tussen de initiëring en de realisering van een experimenteel onderzoeksproject, staat niet in de juiste verhouding tot de lengte van het dienstverband van de medewerk(st)er in z.g. langdurig tijdelijk dienstverband.

9

Te weinig wordt beseft dat een promotie op een experimenteel onderzoek het werk is van een grote groep mensen, waarvan de promovendus slechts de voortrekker(ster) is.

10

Bij de discussie over de gasprijzen voor glastuinbouwers in de verschillende E.G. landen dient ook de hoeveelheid gas benodigd per kilogram produkt betrokken te worden i.v.m. verschillen in gemiddeld aantal uren zon en gemiddelde temperatuur.

11

Hoe nuttig een goed inzicht in de samenhang tussen natuurkunde en maatschappij ook is, toch dient betwijfeld te worden of V.W.O.-leerlingen dit inzicht bijgebracht kan worden als zowel kennis van de natuurkunde als van de maatschappij nog nauwelijks ontwikkeld zijn.

Eijkelhof et.al., Natuurkunde in de samenleving (1978).

18 juni 1982.

G.v.d. Langenberg-Schenk.